A computational atomistic study of lithium transport in graphitic anode materials

A computational atomistic study of lithium transport in graphitic anode materials

by

Christopher M. Shumeyko

Presented to the Graduate and Research Committee

of Lehigh University

in Candidacy for the Degree of

Doctor of Philosophy

in

Mechanical Engineering

Lehigh University

August 2015

Approved and recommended for acceptance as a dissertation in partial fulfillment of the requirements for the degree of Doctor of Philosophy.

_____
Date

_____
Dissertation Advisor

Committee Members:

_____
Dr. Edmund B. Webb III, Committee Chair

_____
Dr. Terry Delph

_____
Dr. D. Gary Harlow

_____
Dr. Martin Harmer

_____
Dr. Jeffrey Rickman

Acknowledgements

There are numerous individuals whom I would like to thank for their support during my graduate school journey. First and foremost I would like to thank my advisor, Dr. Ed Webb for his constant support and guidance over the last 4 years. Your leadership not only with research, but with teaching and education in general was extremely beneficial. I would also like to thank the members of my thesis committee: Dr. Terry Delph, Dr. D. Gary Harlow, Dr. Martin Harmer, and Dr. Jeffrey Rickman.

Second, I want to thank my friends and colleagues from both Lehigh University and Lafayette College. All of our discussions, both academic and not, greatly contributed in helping build character and maturity as I moved toward my post-graduate career. Thank you to Dr. Cody Brownell and Dr. Daniel Sabatino for countless advice throughout the graduate school process. Thank you to my many students over the years, from ME 121 to MECH 03, for helping me discover my true passion for teaching.

Finally and most importantly, I want to thank my family. Thank you to my parents, Drs. Mark and Nancy Shumeyko, for always inspiring me and pushing me beyond my personal limits. For teaching me that learning never stops and that you grow more from your failures than your successes. I wouldn't be where I am today if not for your endless love and support. Thank you to my sister, Alyson, for always being there and understanding this journey and what it means to me. Thank you all and I look forward to what the future holds for us.

"Luck is where preparation meets opportunity." -Randy Pausch

Contents

List of Tables

List of Figures

Abstract

In this dissertation, atomistic simulations of Lithium transport into and through graphite grain boundaries are studied. Graphite is a commonly used negative electrode (anode) material in Lithium-ion batteries yet Li diffusion shows high levels of variability in a material that has been in use for the last 25 years. Researchers have used both experiments and computations to prove such variable diffusion and have proposed numerous hypotheses toward explaining the differences. It is known that intralayer transport is most rapid; the purpose of this study is to address secondary mechanisms for diffusion and therefore, cell charging. Although clues have led to the importance of defects such as grain boundaries in battery anodes, there has not yet been an exhaustive study, either experimentally or computationally, that addresses their role. Grain boundaries have widely been studied in metallic systems, but the covalent nature of graphite creates a two-fold motivation for this study. Not only is transport addressed, but also the underlying GB structure that abets and impedes such motion.

The aforementioned studies are performed using Molecular Dynamics with both as-written and modified interatomic potentials. Potential optimizations and modifications were performed on existing models to fit the needs of this work. Carbon-Carbon interactions are well described, but Lithium-Carbon and Lithium-Lithium potentials were optimized using ab initio and experimental data of the lithium-graphite and lithium-graphene systems. From this, the modified potentials better represent the equilibrium structures of Li_xC_6 albeit with limitations.

Li diffusion from a free surface and into a graphite grain boundary fosters discussions on how surface structure influences transport rates. While no electrolyte or solid-electrolyte

interface (SEI) are modeled here, it is thought that all grain boundaries would be subject to approximately the same level of SEI formation and therefore diffusive flux at the GBs will be similar. Therefore, any differences in intercalation rates that manifest provide additional reasoning to diffusional variability in graphite. While the results may not be absolute, the relativity is what is important here.

Lastly, grain boundary diffusion is studied for the systems analyzed during intercalation simulations. While one boundary may have faster surface intercalation than another, there are underlying questions as to whether surface behavior correlates with or against internal behavior. Data is presented addressing collective mechanisms for diffusion as well as the role of inherent GB structure on mass transport. Finally, recommendations are made to connect this dissertation with continuum models in addition to advance into new material systems for energy storage applications.

Chapter 1

Introduction

1.1 Research Opportunity

As technology has continued to advance over the last century, batteries have become part of our everyday life, even taken for granted by many in today's society. With many aspects of technology, what is discovered today is better than yesterday, and tomorrow will be better than today. The world of batteries are no different. As new materials become cheaper and widely available, battery technology improves daily. For example, Figure 1.1 shows the relative power and energy densities of various rechargeable batteries on the market. Higher power and energy directly relate to increased current and longer discharge times for such batteries [29]. Another way to look at Figure 1.1 is to consider changes over time. With the exception of Li-metal batteries which are considered unstable, moving from left to right can be seen as a movement through history, with emerging technologies resulting in better batteries. The newest technologies, such as Li-polymer and Li-air batteries among others could be placed at the far right of the chart, but these are technologies still very much in their infancy.

With continued efforts to increase our battery capacity, the need for a thorough understanding of macro and nano scale behavior is essential. Li-ion batteries (LIBs) have been around since the early 1990s yet many questions about their behavior are left unanswered. Problems still remain, exemplified by the recent issues with the Boeing 787. When LIBs

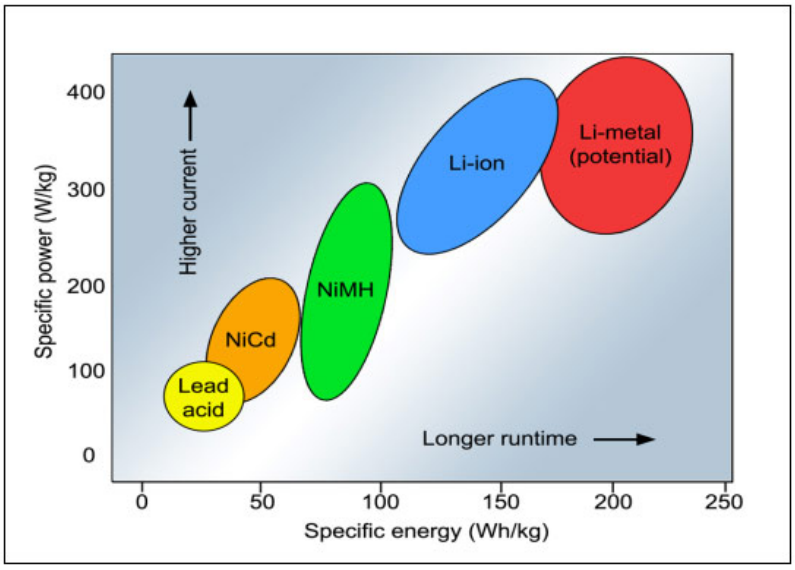

Figure 1.1: Specific power as a function of specific energy for various rechargeable battery types [29].

fail, they can do so catastrophically, leading to dangerous situations such as fires and explosions. The 787 case was very newsworthy because of associated fears with an in-air fire or explosion leading to a possible aviation disaster. Figure 1.2 perfectly captures the reason for continued research efforts with LIBs even as the technology is no longer considered to be at the forefront of battery advancements. Anomalous behavior, especially in confined spaces can prove both costly and fatal. Thus, understanding why this behavior occurs has the opportunity to save lives.

Aside from the safety concerns with understanding advanced battery technologies, there is a greater goal of increasing the planet's dependence on renewable energy. With the global energy usage expected to double by 2050, there is definite urgency in studying renewable energy systems [18]. As the percentage of energy produced from renewable sources continues to grow, the need for better storage follows suit. The downside to renewable energy is that many forms are variable, in that the wind isn't always blowing or the sun always shining. To take advantage of these modes of energy production, increased storage capability is needed to allow power to be drawn for electricity at times when it's not necessarily being produced. Current studies show that based on energy production and usage rates, solar and wind devices can produce enough energy to last 72 hours under proper stor-

Figure 1.2: Battery fire aboard a Boeing 787 Dreamliner at Boston Logan International Airport in 2013 [1].

age conditions [18]. However, such storage technologies do not yet exist, at least not for widespread deployment. Because of their high storage capacity, LIBs are being considered as a frontrunner for renewable energy storage, but the remaining questions about costs, safety, and cycle life all limit their widespread distribution [58]. Recent news of electrical vehicle manufacturer Tesla unveiling a home energy storage device for renewable energy has renewed the importance of safety, in a different light from the 787 incidents [2].

Based on the both the safety and energy considerations mentioned, there is great need to study and fully understand the behavior of energy storage devices. These technologies are crucial to lessening the burden on traditional energy production, but a lack of understanding can serve as a bottleneck for emerging technologies.

1.2 Problem Statement

The aforementioned increasing reliance on renewable energy and associated storage devices are the driving forces behind understanding the role and function of advancing LIB technology. Although LIBs have been on the market for over 25 years, there are still many unanswered questions regarding their behavior. As technology continues to improve, our

portable electronic devices continue to get smaller, faster, and require more power. Energy storage technologies are trying to keep pace, but frequently, complaints are heard of batteries dying too quickly or taking too long to charge. Being able to provide a complete image of the battery cycle, both macro and microscopically, can lead to smart design methodologies to address these known public issues and complaints.

From a scientific point of view, anomalous material behavior can have its causes rooted in materials science and one such example is the effect of crystal structure on macroscopic material properties [94, 76, 77, 83]. Grain boundaries disrupt the ideal perfect crystal and although they have properties that both help and hurt macroscopic properties, understanding their behavior is essential to fully classifying materials. As battery technology continues to change and devices grow smaller, the use of nanoscale battery components is not out of the question. Therefore, in addition to macroscopic effects, the role of grain boundaries in nanoscale mechanisms is equally important [97].

Variability of lithium diffusion rates in graphitic carbon has direction application to LIB charging and discharging rates. Many have noted that the anisotropy of graphite along with Li concentration effects are the cause for the rate differences. Grain boundaries have been shown to have a profound impact on diffusion in metallic systems [78, 87, 33]. Therefore, there is reason to believe that grain boundaries will provide some level of variability regarding Li transport. At what capacity do graphite grain boundaries affect charging rates in LIBs? Do some grain boundaries promote diffusion quicker than others? Are they GBs that prevent transport altogether? How does varying transport rates affect the transient structural behavior of the system?

There are many unanswered questions regarding the role of grain boundaries in covalently bonded materials. Investigating these questions and shedding light on this behavior can provide valuable insight into establishing macroscopic models of LIB behavior and foster discussion on advanced anode design.

1.3 Thesis Objectives

There are several goals of this dissertation centered around the study of mass transport in battery anode materials:

- To investigate lithium-ion intercalation into symmetric-twin tilt grain boundaries in graphite from a free surface.
- To study the surface structure of graphite grain boundaries to understand the mechanisms affecting intercalation behavior.
- To simulate grain boundary diffusion in polycrystalline systems to study connections with intercalation behavior
- To further quantify GB structure and its connections to diffusion.
- To form a collective understanding of Lithium diffusion in graphite such that recommendations can be made to establish a continuum-scale grain boundary diffusion model.

First, there have been no computational studies to date strictly considering grain boundary intercalation in graphite as it applies to energy storage. Grain boundaries are considered a secondary transport mechanism in anodes to edge/gallery intercalation, but nevertheless they are important factors to consider. The intercalation process is the second to last during charging, as it signifies the movement of ions from the electrolyte, more specifically, the solid-electrolyte interface, into the anode. Rate differences during this process would lead to atomic accretion at the interface and asymmetric transport into the anode.

Second, if differences emerge in intercalation rates, quantifying the geometry of the grain boundary that either abets or hinders transport is key to providing insight on anode design. If certain GB character prohibits atom transport into the bi-crystal, such structure can be studied to see what characteristics of the GB drive this behavior.

Third, to bolster intercalation studies, GB diffusion simulations will provide data to foster connections between the two diffusive mechanisms. In metallic systems, some GBs

are thought to provide much faster diffusive pathways, whereas in graphite they are support systems to the very rapid gallery diffusion. The behavior of Li in GBs may showcase areas where motion is squandered altogether and thus provide clues as to how and why overall storage battery capacity drops over time.

Fourth, like in grain boundary studies of metallic systems, the structure of the GB has a profound effect on the mechanical and nanocrystalline properties of the sample [94]. While characterizing the surface plane of a GB will provide clues to nanoscale behavior, it is by no means exhaustive. Analyzing the full GB, in this case, layer-by-layer develops connectivity of diffusive pathways. Doing so provides information toward the final goal of this dissertation in which suggestions are put forth towards establishing a diffusive model for graphite GBs.

1.4 Thesis Structure

The remainder of this thesis is laid out in the following manner. Chapter 2 will discuss relevant background information, including batteries, LIBs, and computational methods. Computational methods will focus on the background of molecular dynamics (MD) along with other nanoscale simulation techniques and the associated models necessary to fully describe systems within this research. Chapter 3 focuses on the optimization of interatomic potentials necessary for Li transport studies in MD, Chapter 4 addresses Li intercalation into a graphite grain boundary from a free surface, and Chapter 5 discusses subsequent grain boundary diffusion in graphite. Chapter 6 extends the structural findings from Chapter 5 to a larger range of grain boundaries consistent with those investigated during intercalation studies. Finally, Chapter 7 discusses concluding remarks from this research as well as proposes future studies to advance the current work beyond the scope of this thesis.

Chapter 2

Background and Methodology

2.1 Batteries

Since the advent of electricity, people have been trying to harness its power, both on the grid and off. The roots of batteries have been debated, as some scientists and historians trace their history back to the Parthian period (∼250 B.C.-244 A.D.) while others argue they came about more recently [109, 46]. Many of these devices that were originally believed to be early batteries may have actually been cells for electroplating various things such as jewelery. In reality, the modern day battery came about in the last 150 years, with the purpose of storing an electric charge for an extended period of time and supplying power when needed. Batteries are energy conversion devices, as the energy is stored in a chemical form and provides electrical power as output [6]. Today, batteries are a part of everyday life, powering our cell phones, watches, and in some cases, our cars. While there are various battery types, they have the same goal and work in similar ways.

All batteries share many common features in terms of their operation. They are compromised of a positive (cathode) and negative (anode) electrode also known as active mass, connected by an conductive electrolyte [7]. When the battery circuit is completed (ie to power a device), electrons flow from the negative terminal to the site of positive potential (cathode), and to maintain charge balance, ions flow through the electrolyte to the anode. The anode and cathode have different chemical composition thus creating a voltage po-

tential when connected together. Once ion concentration is sufficiently depleted, ion flow stops and the battery can no longer provide power. Rechargeable (secondary) batteries take this one step further, because if a large voltage is applied to the cell, this process is reversed, thereby charging the battery again.

The first practical battery cell built with the premise of producing a stored charge was the Galvanic cell, sometimes better known as the Volta Cell, after Alessandro Volta in 1800 [10]. Continuing on Volta's discovery, the Daniell Cell, shown in Figure 2.1, was first constructed in 1836. Here, two dissimilar metals (Cu and Zn) were connected by a wire and suspended in an aqueous electrolyte, which allowed ions and electrons to flow freely in a circuit. The two half cells were separated such that electrons were forced through the connecting wire. As the Zn anode gave up electrons (oxidation) to form Zn^{2+} in the aqueous solution, the electrolyte, SO_4^{2-} ions migrated to the Zn anode to maintain charge neutrality. Conversely, Cu^{2+} ions moved to the cathode (reduction), thus causing material accretion. Over time, the Zn anode would dissolve, while the Cu cathode would grow. Seeing as the anode degrades as electrons continue to move, the reuse of this cell is impossible, but it did prove the energy storage concept [6].

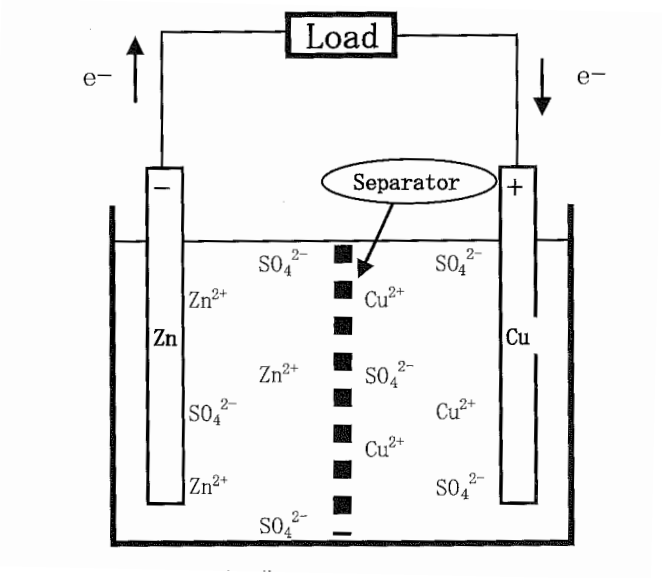

Figure 2.1: Schematic of the Daniell cell, a primitive form of battery reaction [6].

From this primitive galvanic cell, the first primary batteries were invented, specifically

Lead-acid batteries in the mid-1800s [7]. As a bit of nomenclature, batteries are made up of numerous *cells*, which can be connected in either series or parallel to increase the storage capacity of the battery [11]. Primary batteries are those that cannot be recharged, whereas secondary batteries are those that can, like LIBs, which are the focus of this dissertation [12].

2.1.1 Fundamental Battery Laws

When discussing batteries, there are two conditions or states that need to be considered. First, the thermodynamic or equilibrium state and associated parameters characterize the battery's behavior when there is no current flowing. In this form, the battery is at its highest possible potential, U^0. The second state occurs when current is flowing through the battery and is referred to as the kinetic state and parameters [12]. The kinetic state disrupts the established parameters of the thermodynamic equilibrium and is influenced by the actual design of the battery cell. One of the greatest kinetic parameters to discuss is diffusion and mass transport.

The equilibrium states do not depend on the reaction path, such as separation distance of electrodes, but rather the products and reactants of the actual reaction [12]. Three important parameters to consider for classifying equilibrium performance are: the enthalpy of reaction, ΔH, the free enthalpy of reaction, ΔG and the entropy of reaction, ΔS. The enthalpy of the reaction dictates the maximum possible heat generation during the reaction, if no electrical energy is being produced. Gibb's free energy change is the opposite, rather describing the amount of chemical energy that can be converted into electrical energy. Finally, the entropy of reaction details reversible losses or gains [12]. The three terms are related by:

$$\Delta G = \Delta H - T \cdot \Delta S \tag{2.1}$$

where T is temperature in degrees Kelvin. The second important relation to consider during equilibrium is the determination of the equilibrium cell voltage, given as:

$$U^0 = -\frac{\Delta G}{n \cdot F} \tag{2.2}$$

Here, F is the Faraday constant, or 96485 $A - s/mol$ and n is the total number of exchanged electronic charges (in moles). Together, their product symbolizes the total amount of electrical charge associated with the reaction [12]. Finally, multiplying this product by the equilibrium voltage obtains the total electrical energy generated by this reaction, equivalent to ΔG.

When current flows and kinetic processes are considered, diffusion is a leading parameter, as the movement of ions must remain steady with the flow of electrons. Therefore, it can be said that diffusion is, in a way, one rate-limiting process in battery chemistry. The other parameter to consider is the deviation from the equilibrium voltage, again caused by the flow of current in the form of polarization (difficulty of charge transfer) at the electrodes and losses due to resistance in battery components [72]. The operating voltage or actual voltage, differs from the equilibrium voltage during discharge by:

$$U^d = U^0 - U^L \tag{2.3}$$

or more specifically,

$$U^d = U^0 - \eta^- - \eta^+ - IR \tag{2.4}$$

where η is the polarization of the negative and positive electrodes, respectively, and IR is the resistance losses, also known as ohmic losses. As seen in Figure 2.2, IR losses have a greater impact than polarization losses, as they are directly related to the current flow through the battery. An equivalent way to view Figure 2.2 is to consider the current as the actual capacity of the battery, C, in Amp-hours. For example, if a battery can supply one A-h of power, and it does so at a rate of $C/5$, the battery will be usable for 5 hours [72].

There are countless other parameters and factors that contribute to designing batteries, but the goal here was to provide basic working knowledge of a battery in the context of this dissertation. More specifics regarding lithium-ion batteries will be discussed in the

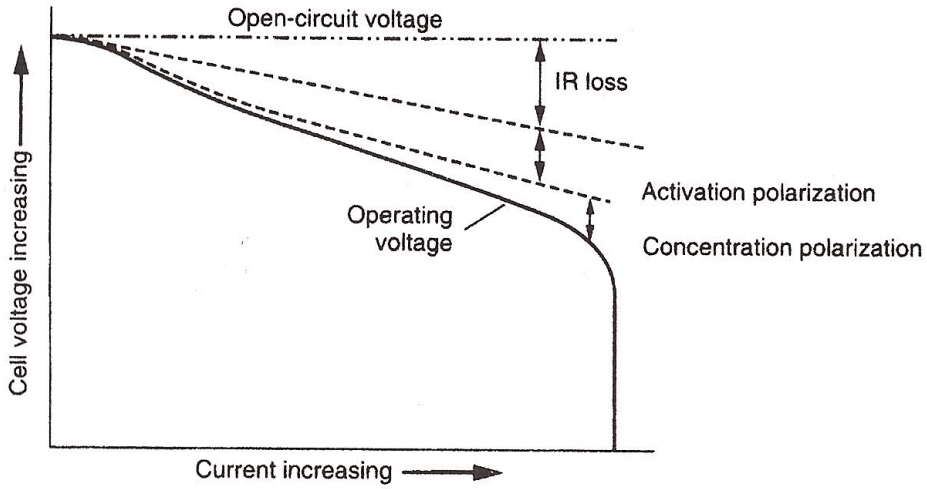

Figure 2.2: The effect of polarization and IR loss on actual operating voltage in a battery [72].

subsequent section.

Figure 2.3 shows the progression of battery development, starting with Lead-acid in the mid 1800's all the way through possible future batteries in 2050. While the operating mechanisms are generally the same as those presented above, there are differences that separate them and their operational capacity. Lead-acid and Li-ion batteries are similar in the sense that they are secondary batteries who use the same active material in both electrodes- Pb and Li, respectively. LIBs have the highest operating voltage of the existing battery types shown, which correlates with the total amount of energy that can be produced.

As battery technologies continue to evolve, there is continued drive to lower their production cost, increase their storage capacity, and make them more sustainable [7]. Although there has been progress in these areas, existing LIBs still present their own challenges, which will be discussed next.

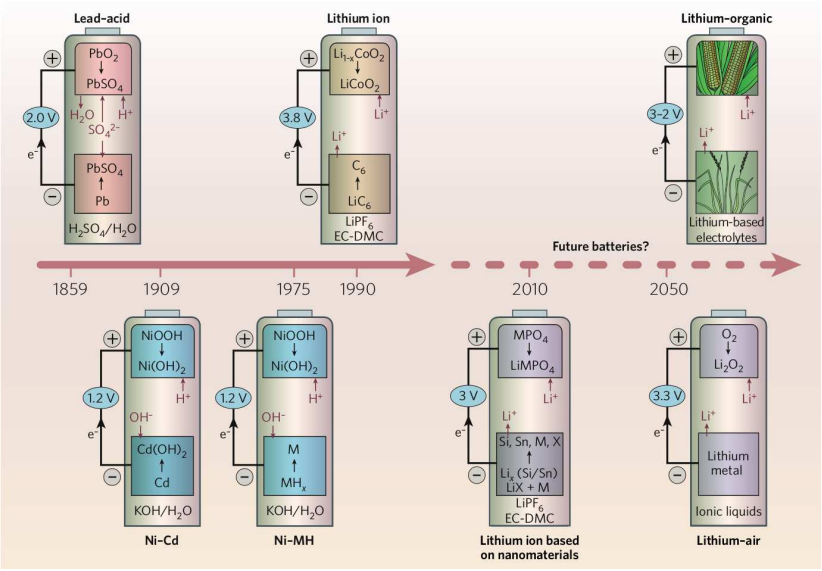

Figure 2.3: The history of modern battery types as well as predictions about future technologies [7].

2.1.2 Lithium-ion Batteries

Lithium-ion batteries are derived from Li-metal batteries, which had a very high theoretical capacity, but possessed numerous safety concerns because of the formation of Li dendrites (tree-like crystals) which caused short circuits during cycling [8]. Originally developed by the Sony Corporation in 1991, LIBs were created with lithium intercalation materials as an anode to combat the problems with Li-metal batteries. The major difference is there is no lithium metal in LIBs, but metallic Li can form on the anode during charging. In addition to a new battery chemistry, Sony also incorporated some of the battery world's first safety features, including a current interrupt device and electronic circuitry to control charging and discharging [8]. The first iterations of LIBs were certainly improvements on their predecessors, but as more materials research was performed, LIBs began improving as well. Figure 2.4 details the increase in capacity of LIBs as a function of new materials over time, primarily through the transition of anode materials from hard carbons to graphite, as well as electrolyte additives and a more stable cathode [8]. Today, LIBs have a theoretical capacity or total electrical charge that can be drawn from the battery, of approximately 372 mAh/g, up from 200 mAh/g at first iteration.

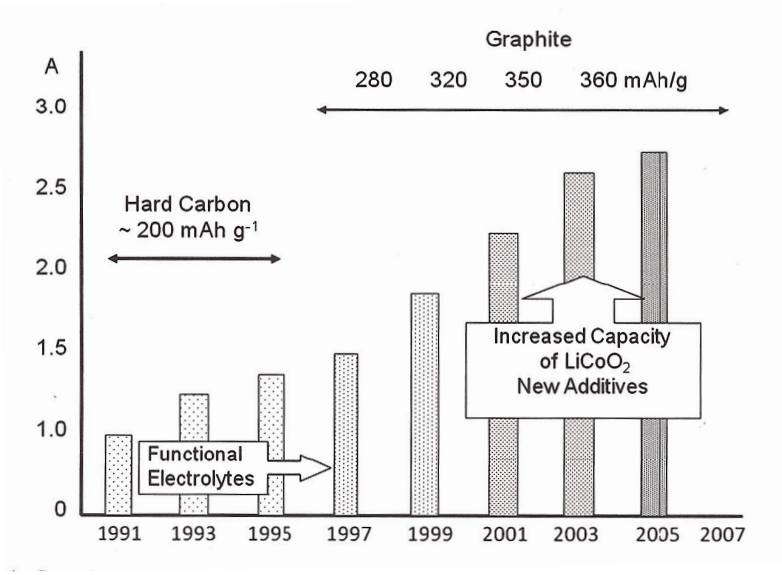

Figure 2.4: Advancements in storage capacity as a function of new materials and methods [8].

Before discussing additional details about LIBs, it's worth showcasing the components mentioned in the preceding section. Figure 2.5 shows an LIB during charging; electrons are flowing from the cathode, through the load, to the anode, while Li-ions are flowing in the same direction but through the electrolyte. The silver and gold bars represent the positive and negative current collectors, respectively. Like in any battery, the role of the current collector is to join the ion and electron portions of the circuit at both the anode and cathode. In this example, the anode is represented by graphitic carbon and the cathode is a Lithium-Metal-Oxide, which varies by application although Lithium-Cobalt-Oxide is often used [7]. The electrolyte material can vary as well and will be discussed in detail later, however, its role is to smoothly transfer ions from the cathode to the anode and vice versa. For comparison to reality, Figure 2.6 shows the same components as the schematic, but in their production form. The anode and cathode are actually rolled sheets with a separator between them. Included in the cell is a safety vent in the case of large pressures inside the battery. LIBs can be manufactured in many different forms from the one shown here, although they all contain the same components.

When LIBs are first assembled, there is a pristine interface between the electrolyte and the electrodes. If the electrolyte was composed of just elements necessary to transport

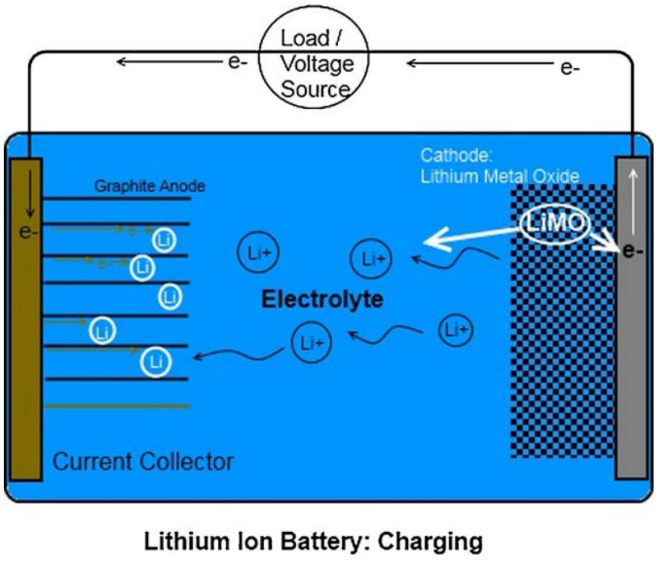

Figure 2.5: Schematic of modern Lithium-ion battery components during charging [25].

ions, it would react with the graphite surface causing degradation of the anode and decomposition of the electrolyte, which leads to long-term capacity loss. Instead, companies began including additives into the electrolytes to prevent this reaction from happening and instead a purposeful solid-electrolyte interface (SEI) is formed to eliminate 'active sites' on the graphite surface [72]. Figure 2.7 shows the impact of including additives into the electrolyte. The top panel shows non-homogeneous distribution of the SEI when no additives are used, conversely, with additives, there is a widespread distribution of small SEI particles on the graphite surface. While the SEI is essential to battery performance, it greatly impacts the diffusion of Li-ions into the graphitic anode, which is showcased in Figure 2.8. The rough SEI undoubtedly interrupts transport pathways from the electrolyte into graphite edge-planes, where Li sites at the fully charged state. After the first charge/discharge cycle, the SEI assumes the structure seen, with its density varying as a function of distance from the actual anode. This occurs because of interaction distances between the electrolyte additives and the electrode. As the SEI grows, the additives must diffusive farther through it, thereby rate limiting its accretion. A similar phenomena is observed in intermetallic coumpound (IMC) growth between tin and copper in the well-known tin whisker geometry [14, 15].

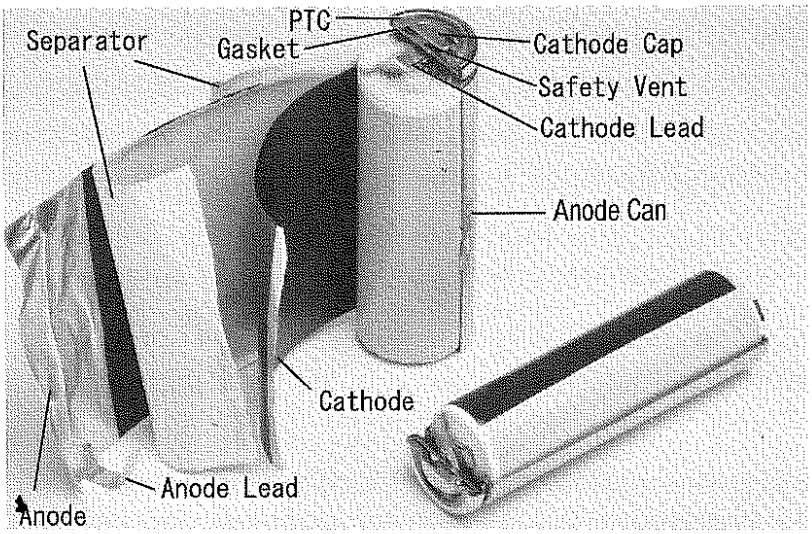

Figure 2.6: Blown apart structure of a lithium-ion cell [6].

As desirable as LIBs are for portable electronics and large-scale energy storage, they still have numerous safety concerns that limit their application. The events involving the Boeing 787 brought the problems closer to the public's eye and forced greater discussion on how to circumvent them if LIBs are to be used more widely. While one problem is the public's misconception about lithium use in general, there are issues to be resolved. The issue that makes LIBs so volatile and potentially dangerous is the combination of highly energetic materials with flammable electrolytes, which are based on organic compounds [9]. This mix, in the presence of blatant misuse, such as overcharging, excessive heating, or improper disposal can lead to the largely publicized fires or explosions. Misuse, however, is not the only method in which these batteries cause issues. Overheating is frequently thought of as the main issue with LIBs. Here, exothermic reactions in the cell can be triggered by the application of heat to the system, where chemical reactions (rather than the desired galvanic reactions) begin to occur [9]. If, as these reactions are occurring, the battery can dissipate heat, then there is no issue. However, when the cell continues to heat up, the chemical reactions occur more rapidly thereby fostering thermal runaway. This, by nature, is associated with excess pressure, leading to mechanical failures of various components.

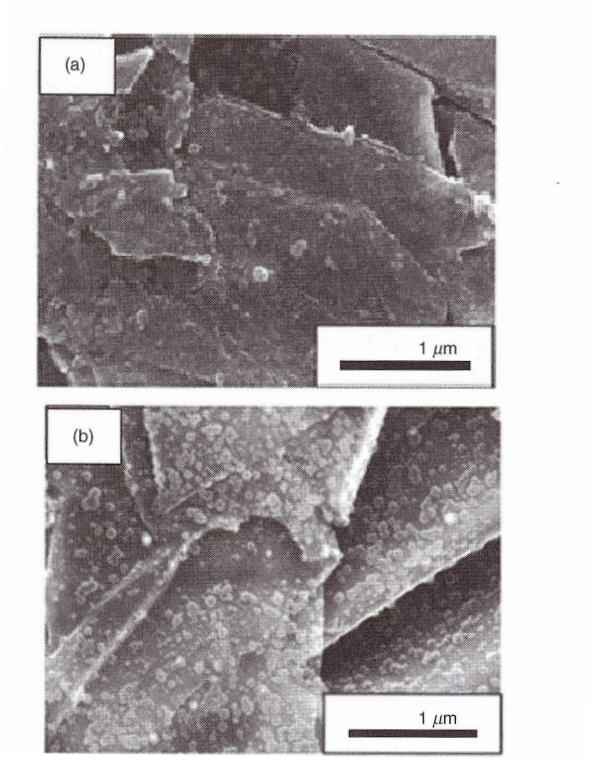

Figure 2.7: Graphite anode after cycling without (a) and with (b) electrolyte additives [72].

While the generation of heat in LIBs is unavoidable, adequate heat dissipation is a must to prevent the dangerous and unwanted chemical reactions from occurring. Thus, batteries are designed with safety measures in place to aid in heat transfer away from the battery, either by convection or radiation [9]. However, as electronics get smaller, the spaces allowable for heat dissipation shrink as well. Therefore, preventive measures for thermal runaway remain a constant engineering challenge. One solution used in the 787 case was independent of the battery itself, where the containment device for the LIBs was bolstered, such that the failure was not catastrophic to the aircraft. This solution is not practical everywhere though and still does not address failure of the device itself.

Another important safety feature or consideration in LIBs is the sizing of the electrodes. As will be explained later, the maximum capacity of the anode and cathode are defined by chemistry, but overcharging/discharging remains a possibility because of the forced voltage differential. Based on this chemistry, cyclability of the cathode is rather good, but the anode is subject to degradation at a quicker rate. Therefore, as a safety feature, the

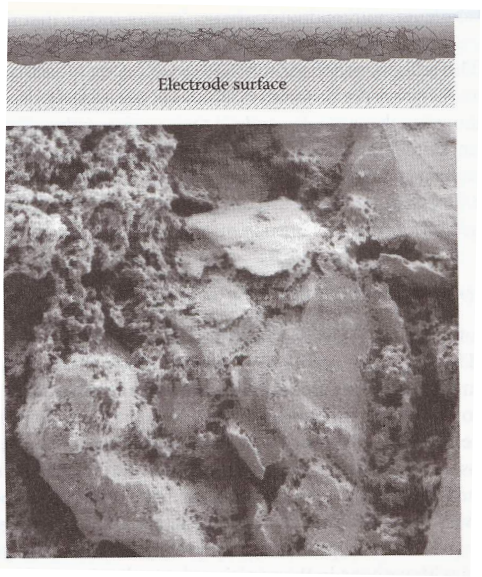

Figure 2.8: Actual SEI formation on graphite. The top diagram details SEI formation density, which decreases with distance from the anode surface [11].

anode capacity is usually greater than the cathode, thereby preventing over-discharging and slowing degradation [11]. It is important to keep in mind that relative to other battery types as well as electronics in general, LIBs are a very young technology and thus warrant further investigation, like that being studied in this dissertation [89].

2.2 Graphite

Graphite is a material comprised of layers of carbon, oriented in covalently bonded hexagonal rings with sp^2 bonding. Layers are ordered in an ABAB stacking sequence and are connected via relatively weak van der Waals forces. A single plane of carbon atoms in graphite or alone, is referred to as graphene [8]. These bonding characteristics lead to highly anisotropic behavior in numerous categories. Figure 2.9 shows an example of a graphite lattice, with the graphite primitive unit cell highlighted on the right side of the image. The unit cell of graphite is not like typical fcc or bcc class lattices, but rather hexagonal in nature. Like shown in Figure 2.9, the unit cell is actually a rhombohedral shape, as opposed to hexagonal as one would expect [52].

The hexagonal nature of graphite arises from the repetition of C-C bonds with sp^2

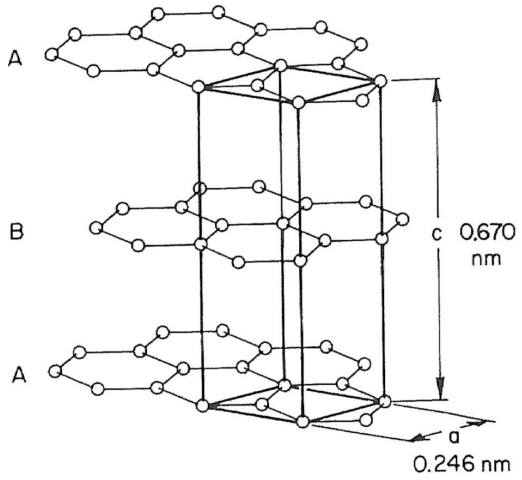

Figure 2.9: Example of graphite lattice showing three adjacent layers with the distinct ABA stacking sequence and experimental lattice constants at $T = 0$ K [39].

hybrid orbitals. The in-plane bonds are so strong because of the *sigma* bonds while the layering and associated weak vdW forces come from interactions of π-electron clouds. Graphene (single-plane of C atoms) is considered one of strongest materials in the material world, which results from these *sigma* bonds, the same of which are found in diamond [19]. The equilibrium in-plane lattice constant is $a = 2.46$ Å, while out-of-plane it is, $c = 6.7$ Å. In the primitive unit cell, the lattice vectors are:

$$a_1 = a\left(\frac{\sqrt{3}}{2}, \frac{1}{2}, 0\right) \tag{2.5}$$

$$a_2 = a\left(\frac{\sqrt{3}}{2}, -\frac{1}{2}, 0\right) \tag{2.6}$$

$$a_3 = c\,(0, 0, 1) \tag{2.7}$$

where a_3 is perpendicular to the basal plane. The basis atoms in the graphite unit cell are listed in Table 2.1.

Graphite is widely used as the negative electrode (anode) in LIBs because of its stability, high theoretical capacity, and reversibility relative to other materials, especially Li-metal [38]. Other advantages include its high corrosion resistance, low elasticity, low cost, and

Table 2.1: List of basis atom positions in the graphite unit cell.

Index	a_1	a_2	a_3
C_1	0	0	$\frac{1}{4}$
C_2	0	0	$\frac{3}{4}$
C_3	$\frac{1}{3}$	$\frac{2}{3}$	$\frac{1}{4}$
C_4	$\frac{2}{3}$	$\frac{1}{3}$	$\frac{1}{4}$

high purity [8]. Like will be discussed in the next section, a high percentage of graphite edge planes in an anode are desired because of the rapid intercalation that takes place here. To influence that behavior, mechanical milling of natural graphite flakes can induce certain arrangements, like the ones seen in Figure 2.10. It's worth noting though, that these arrangements still have internal interfaces where graphite fragments join, which depending on orientation, could form grain boundaries while others could be more amorphous regions [8].

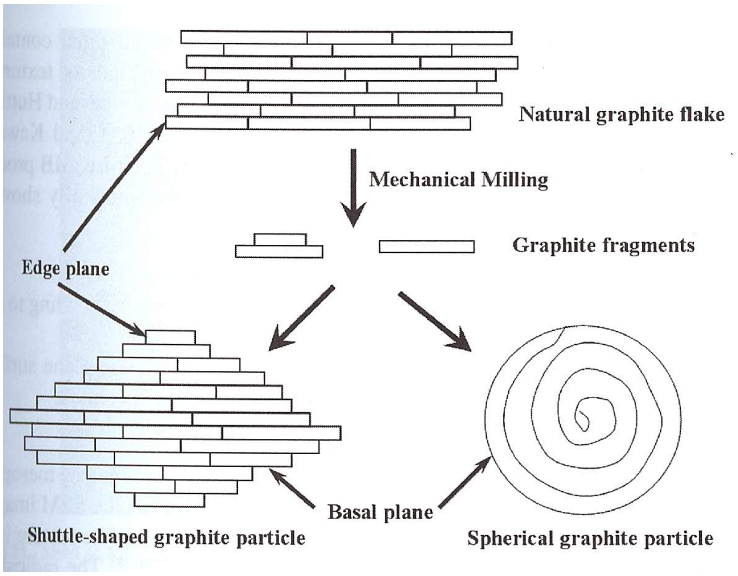

Figure 2.10: Production of graphitic anodes from natural graphite flakes. Vertical lines dictate edge-planes as well as grain boundaries [8].

The high reversibility of graphite anodes stems from the ability of Li-ions to quickly and easily enter and exit graphite crystals. An example of a graphite edge plane, those that are so conducive to rapid transport, is seen at left in Figure 2.11. Li site between layers

of graphite and can easily leave the crystal via these galleries. When chemically stable LiC_6 is formed, lithium atoms site in between layers of graphene, aligned in the center of hexagonal rings, like the right panel of Figure 2.11. The equilibrium lattice spacing for Li sites is 4.3 Å in plane. The weak van der Waals interlayer forces in graphite are screened by the Li-Li repulsion to cause expansion of the lattice in the c direction. The result is an interlayer spacing of 3.7 Å, which is approximately 10% greater than bulk graphite [8]. Greater detail regarding this expansion and its affects will be discussed in Chapter 3.

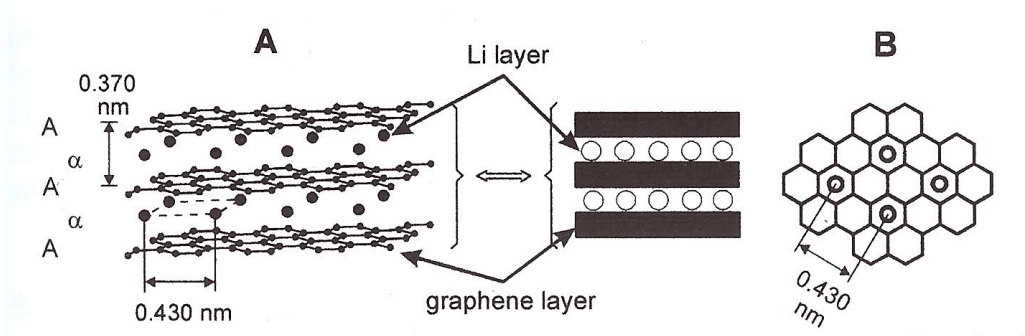

Figure 2.11: Lithium intercalation structure in graphite [72].

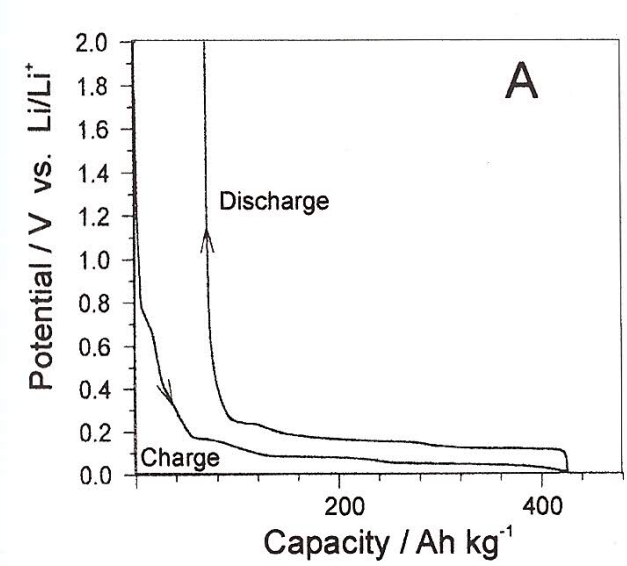

Figure 2.12: First cycle charge/discharge characteristics for Li in graphite [72].

Before discussing the details of Li diffusion in graphite, which deviates from direct discussions on LIBs, one last application should be mentioned. Graphite's voltage profile and cyclability are two reasons it's widely used in LIBs, but the first charge/discharge

cycle is unique from others. As shown in Figure 2.12, the first cycle experiences a capacity loss, as shown in the difference between charge and discharge portion of the cycle. This change is capacity is due to the formation of the SEI, where a reaction takes place at the electrode surface prior to intercalation of Li ions, shown from 0.8 to 0.2 V in the charging curve. Once the cell voltage reaches 0 V, Li metal can deposit on the electrode surface, which should be avoided [72]. After the first cycle, the charge capacity of graphite largely remains the same, hence its high cyclability. There are limits, of course, as no battery has an infinite cycle life.

While graphite is highly advantageous and reliable for use in LIBS, as will be discussed, there is a huge range of Li diffusivities reported that warrant investigation. Diffusion in bulk graphite will be discussed below, with more complex diffusion mechanisms such as defect diffusion being addressed later in this dissertation.

2.2.1 Li Diffusion in Graphite

With graphite being the most commonly used anode in modern day LIBs, it comes as no surprise that diffusion in graphite has been widely studied for the last several decades [88, 110, 37, 38, 93, 99, 57, 34, 82, 101, 49, 66, 74, 79, 56]. The importance of diffusion comes from the direct relation to cell charging and discharging; the faster the diffusion of ions in a battery corresponds to decreases in charging times. Graphite is a leader for anodes because it's one of the best materials in terms of coulombic capacity per volume, which when discussing electric vehicles, relates directly to range between charges [99]. Even with on-going research, large variability in Li behavior in graphite still exists and thus there is further opportunity to quantify such diffusion. Persson *et al.* noted that a battery is only as strong as its weakest and the highly varied diffusion can certainly plague overall performance [70]. While all the previous research performed does not specifically comment on its application to LIBs, it can nevertheless be applied toward understanding the mechanisms at which such batteries operate.

Diffusion, in the most general sense, describe the motion of atoms. Since diffusion is frequently discussed in this dissertation, it's worth addressing the relation between the

diffusion coefficient, D and the motion of an individual atom. For atoms in a crystal lattice, their motion can be described by a random walk process [43]. Detailing this process and the probability of finding a random walker in a given position after time, t, leads to the derivation of the diffusion coefficient. In the one dimensional case, assume a random walker can move a distance a, either right (+) or left (-), with equal probability. After N steps, the position of the walker can be described by:

$$R_N = a_1 + a_2 + a_3 + \ldots + a_N \tag{2.8}$$

Since there is equal probability of a move to the left or right, the average final displacement, $\overline{R_N}$, is zero. However, when looking at an individual walker, this is not necessarily the case. Thus, there is a distribution of final positions that can be described by observing the square of Equation 2.8;

$$R_N^2 = Na^2 + \sum_{i \neq j} a_i a_j \tag{2.9}$$

When considering $a_i a_j$, there are two outcomes that give positive answers (both move same direction), two which give negative answers (opposite directions), both with equal probability. Therefore, the second term of Equation 2.9 will, on average, be zero. That assumptions means that the average root mean square displacement is:

$$\sqrt{\overline{R_N^2}} = \sqrt{N}a \tag{2.10}$$

This result can be related back to the diffusion coefficient, D, if the number of steps, N, is written as Γt where Γ is the jump frequency and t is time. Then, when considering Fick's first law, the diffusion coefficient in one dimension is:

$$D = \frac{a^2\Gamma}{2} = \frac{a^2 N}{2t} = \frac{\overline{R_N^2}}{2t} \tag{2.11}$$

This can expand to two dimensions when the additional directions of motion are considered (4 in 2-D):

$$D_{2D} = \frac{\overline{R_N^2}}{4t} \tag{2.12}$$

Various experimental techniques have been used to calculate Li diffusion rates in carbonaceous materials as a function of different variables, including state of charge (varying x in Li_xC_6), temperature, and material geometry [110, 88]. Figures 2.13 and 2.14 exhibit two such studies in which differing results were uncovered. Yu *et al.* calculated diffusion coefficients as a function of state of charge and uncovered very little dependence on such. States of charge from $0 - 40\%$ were investigated, with diffusion approximately constant at $D = 10^{-9}\ cm^2/s$ [110]. Takami *et al.* on the other hand noticed a large dependence of diffusivity on composition, with a difference of 2 orders of magnitude $\left(10^{-08} - 10^{-10}\ cm^2/s\right)$ for natural graphite [88]. While these results only scratch the surface of past experiments for Li diffusion in graphite, they certainly elucidate the notion that such quantities are highly variable and dependent on many factors.

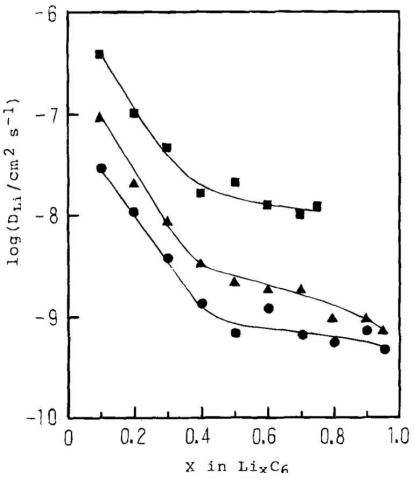

Figure 2.13: Rapid lithium diffusion rates in graphite as a function of concentration [88].

One of the most common methods for simulating and investigating lithium intercalation and diffusion in graphite is via first-principles techniques in which few, if any assumptions are made about the system of interest. Ab initio techniques model the electronic structure of a system without the addition of empirical parameters like those used in classical simulations such as molecular dynamics. An inherent problem of first-principles calculations

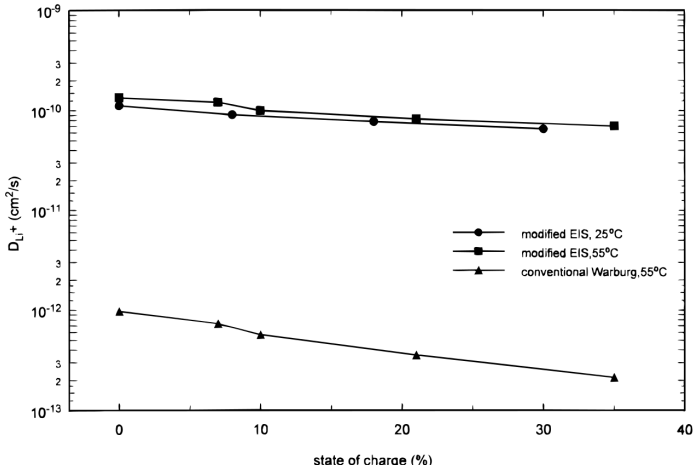

Figure 2.14: Low-end lithium diffusion rates in graphite as a function of stage of charge [110].

though is the misrepresentation of van der Waals forces, which are an integral piece of the graphite model. These van der Waals (vdW) forces are very weak, non-bonded, intermolecular forces that are responsible for holding layers of graphene together to form graphite. The covalent interactions in a graphene plane are contained within that plane and thus can be thought of as a 'closed-shell' system, leaving vdW interactions as the sole means of connectivity. A practical realization of these weak interactions is seen when rubbing a piece of pencil lead (graphite) in between your hands. After a short while, a noticeable amount of material has accumulated on your hands and it's these weak intermolecular forces that cause graphite to be highly susceptible to shear deformation, leading to material transfer. This is also why graphite is so widely used as a solid lubricant.

Many first-principles studies solve the above problem by incorporating a dispersion term, by one means or another, into their model. This however by nature, adds an empirical component to the problem, thereby abandoning traditional first-principles methods. There have been extensive studies and trials on perfecting a dispersion term to correctly model vdW forces, all of which have a certain degree of shortcoming or overestimation [47, 38]. Regardless of this variability, such studies still provide valuable insight in Li behavior in graphite and are worth discussing further.

The origins of this dissertation and research although broadly centered around Li dif-

fusion in graphite, originated from the work of Persson, *et al.* who performed both experiments and computational studies in the last five years on this system. Persson noted the high diffusional anisotropy in graphite and performed unique experiments to probe such differences. By creating a Devanathan-Stachurski (D-S) type two-compartment cell, which was originally used to test hydrogen permeation and diffusion through palladium, Persson was able to experimentally probe Li diffusion in highly-oriented pyrolytic graphite (HOPG) [27]. HOPG by design has graphite crystals aligned in the basal direction with minimal angular offset thus allowing for highly controlled investigations into diffusional anisotropy. First, Persson used a pristine membrane of HOPG, like the one seen in the inset of Figure 2.15, as a working electrode connecting the two compartments of the cell. A current was placed across the membrane such to encourage Li diffusion through the HOPG membrane. Since the basal planes of the graphite crystals were exposed to compartment A, the sole means of transport through the membrane were vacancy defect or grain boundary diffusion, since lattice diffusion is highly energetically unfavorable [57]. A limited number of step edges were also available as transport pathways. An increase in current density in compartment B would signify successful diffusion through the membrane and this trend can be seen in the main panel of Figure 2.15. While current density does increase in compartment B, Persson noted that only a fraction of the inserted Li ions successful diffused through the membrane, noting that the majority of the ions likely became trapped. This will be discussed in detail later, but it is thought that the connectivity of fast grain boundaries could abet diffusion such that no two HOPG membranes like the one see here exist.

As a means of comparison in diffusion rates, a second experiment was setup using the same D-S type two compartment cell. This time however, artificial defects were created by drilling $1mm$ holes, located $0.5mm$ apart into the membrane, as seen in the inset of Figure 2.16. The goal here was to allow Li ions to quickly intercalate into the HOPG membrane and rapidly diffuse between graphene planes to the second void, and out into compartment B. For this case, the current response (Figure 2.16) was much more rapid, on the order of seconds instead of hours, and there was a nearly 100% coulombic efficiency [71]. Applying Fick's second law (Equation 2.13) to these experiments allowed for direct

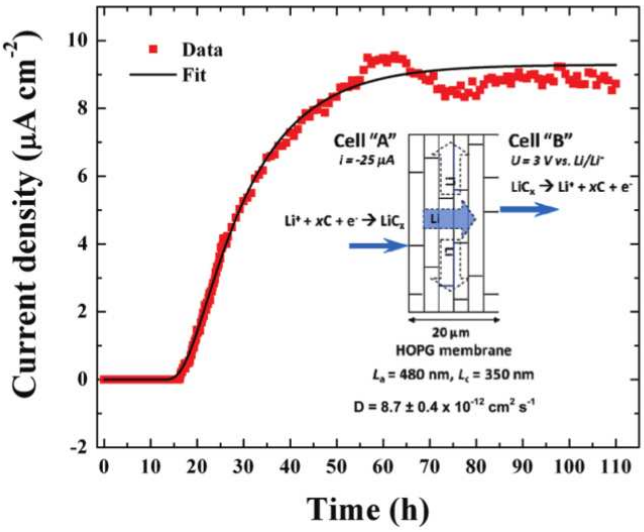

Figure 2.15: Experimental data displaying current density as a function of time across an HOPG membrane [71].

measurements of diffusion parallel and perpendicular to the graphene planes, calculated as $D_{\parallel} = 4.4 \times 10^{-06}\ cm^2/s$ and $D_{\perp} = 8.7 \times 10^{-12}\ cm^2/s$, respectively. Fick's second law describes how diffusion, D, drives changes in concentration (ϕ), over time, t [43].

$$\frac{\partial \phi}{\partial t} = D\frac{\partial^2 \phi}{\partial x^2} \tag{2.13}$$

This work was one of the first to distinctly recognize the diffusional anisotropy and point to grain boundaries as the main transport mechanism across the basal plane in graphite. These results however, ignore any sort of concentration effects on diffusion. The highly repulsive ionic Li-Li interactions in-plane at high concentrations block, to a degree, transport thereby driving down diffusion rates [71].

Like mentioned above, many researchers use first-principles to study chemical diffusion of Li in graphite. MD methods are useful in simulating diffusive events where trajectories can be mapped over time. Certain situations, such as the vacancy diffusion of Li in high concentrations, are hard to obtain via traditional MD because it's much too computationally expensive. Therefore, researchers obtain hop frequency rates, or the rate at which Li atoms jump between lattice sites from first-principles, defined empirically as

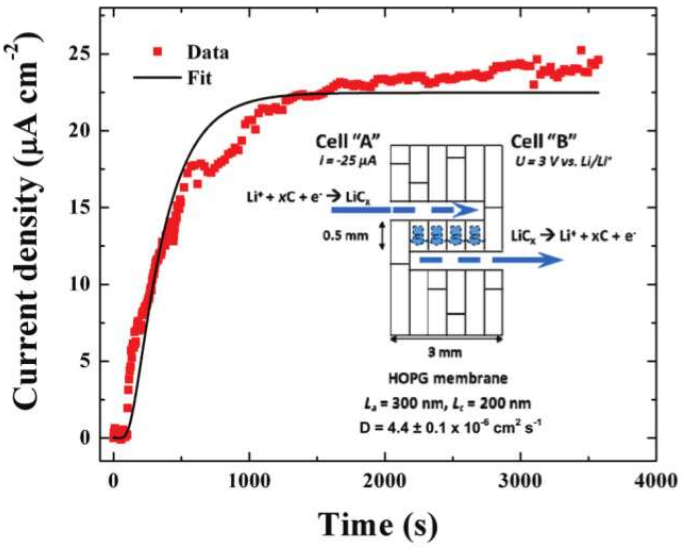

Figure 2.16: Experimental data displaying current density as a function of time across an HOPG membrane with artificial defects drilled into the graphite [71].

$$\Gamma = \nu^* exp\left(-\Delta E_k / k_b T\right) \tag{2.14}$$

where k is the Boltzmann constant, ΔE_k is an activation energy, T is temperature, and ν^* is a vibrational frequency [70, 93]. The exponential prefactor, ν^* is comparable to an attempt frequency, whereas the exponent itself is the actual probability of a successful hop based on energetics [93]. Knowing the hop frequency, Γ, allows researchers to use Kinetic Monte Carlo (KMC) simulations to obtain diffusion coefficients for systems where MD perhaps falls short. It's important to note however that KMC cannot determine this frequency on its own, it must be in the input parameter set from the beginning. Determining ν^* and therefore Γ is not straightforward and takes great attention to detail during first-principles calculations.

2.3 Grain Boundaries

All materials in nature are made of up atoms, arranged on a lattice that is dictated by the size of the atoms and the bonding nature of the system [31]. In a single crystal (solid), all the atoms and bonds are arranged in an identical way, such that it creates a uniform

arrangement throughout. However, if a material is originally liquid and undergoes a phase transformation to a solid, it's highly unlikely all the atoms will arrange themselves into a single crystal. Rather, solid crystals begin to nucleate throughout the liquid as it solidifies, with varying arrangements, sizes, and orientations [31]. As solidification continues and finally ceases, these crystals come together at interfaces known as grain boundaries, like the ones seen in Figure 2.17.

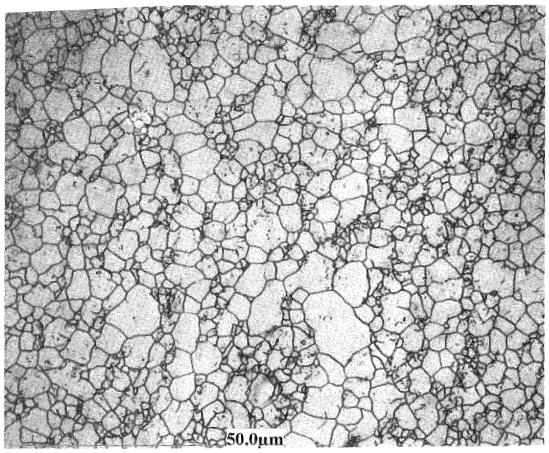

Figure 2.17: Polycrystalline material viewed under a microscope containing numerous grain boundaries [31].

Grain boundaries are unique because atomic and bonding arrangements near the interface differ from the perfect crystalline lattice. Instead, atoms fall closer or farther than equilibrium and take on unique bonding configurations. Generally, the deviation from crystalline orientation is rather tight to the boundary and within a few nanometers or less, atoms retain the perfect lattice arrangement. The reason grain boundaries are important to study is that their unique orientation greatly affects mechanical, thermodynamic, and transport properties of a material [31]. Even in pure elements and compounds, a certain amount of impurities can exist in the sample. These impurities can migrate to the grain boundaries by diffusion mechanisms, thereby also negatively affecting macroscopic properties [31]. This concept though, of dopants migrating to GBS, opened the door for material enhancement and strengthening. Such enhancement, through the subtle control and chemistry, can create numerous different structures at the boundary, so named com-

plexions, by Harmer *et al.* [28, 17]. While many researchers are focused on the effect of grain boundaries in mechanical failure modes (Ashby Maps), this study will focus solely on the role of grain boundary structure in mass transport. One must remember that grain boundaries are dynamic in that they can migrate as well as act as source and sinks for atomic diffusion [31]. Here, the concern is with the motion of a dopant, in this case, Li, rather than self-diffusion of carbon atoms through graphite GBs.

Grain boundaries are characterized by a number of different factors including, width, energy, structure, misorientation angle, and relative grain orientation [31]. There are many different orientations to consider, as seen in Figure 2.17. No two interfaces are alike and it's not uncommon to see more than two crystals coming together at one location. For the purposes of this study, simple interfaces will be considered, where two grains meet at a common interface. At this interface, two crystals can arrange themselves in various ways, like the ones in Figure 2.18. To describe the GB, there are macroscopic (6) and microscopic (4) degrees of freedom (DOF) to consider. Macroscopically, three DOFs describe crystallographic rotation, two define the GB plane, and one describes the possible inversion required to bring one crystal in alignment with another. Microscopically, three DOFs describe grain translation (to be discussed later) and one defines GB position [31].

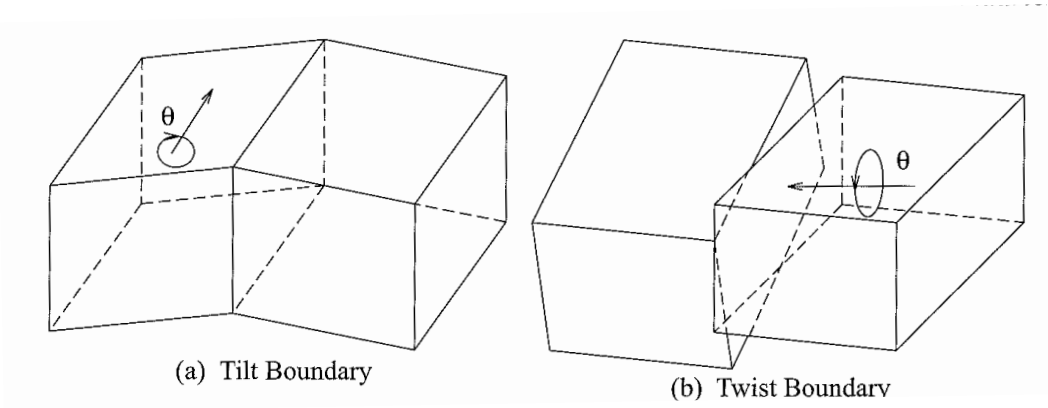

Figure 2.18: Example of two types grain boundary interfaces [31].

In a tilt GB, two crystals share an entire common plane, even though the two crystals have a random orientation from one another. In a twist boundary, the crystals share different rotations about the common plane, leading to a crystallographic mismatch at the

boundary. In graphite, this leads to mismatch across galleries, whereas tilt boundaries remain planar.

There exists a special category of boundaries within tilt boundaries known as a twin boundary. Twin boundaries are unique because they are highly symmetric and atoms at the boundary are common to both crystals that compose the GB. In fact, all nearest-neighbor atoms are in the correct arrangement, but the second neighbors are in the incorrect location across the boundary [43]. This can occur when crystals with only slight misorientation come together during growth processes. Figure 2.19 shows an example of a symmetric twin boundary, with overlapping atoms shaded in black.

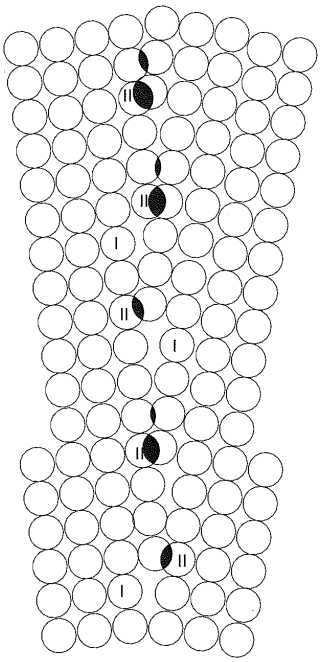

Figure 2.19: Unrelaxed twin grain boundary. The black shaded regions refer to areas of atomic overlap between the two crystals [31].

Even though many grains come together at random orientations that show little or no coherence, there are certain situations were the GB can be described by a repeating pattern of atomic arrangements (ie structural units) [95]. In this orientation, the coincident site lattice (CSL) notation can be used. Here, the total number of shared atomic sites between the two grains are divided by the number of sites at the GB. The boundary is thus described by its Σ value, where Σ^{-1} sites are common to both grains [31]. Figure 2.20 shows two

examples of CSL boundaries, notably the Σ11 and Σ9 GBs in aluminum and copper.

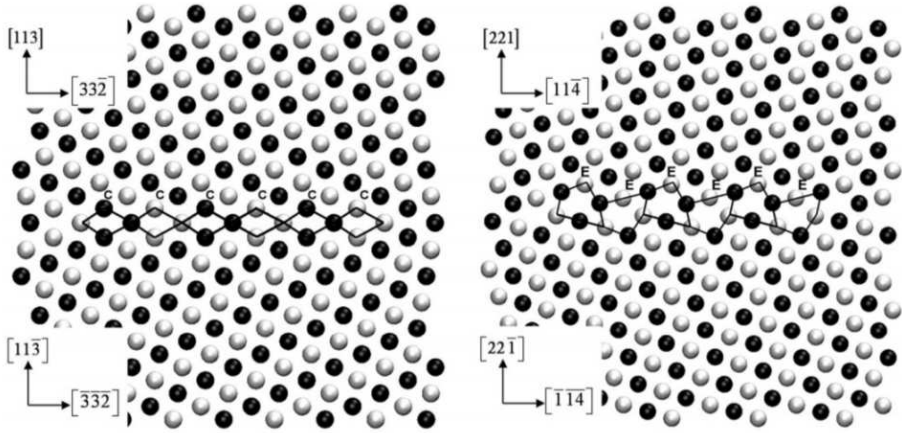

Figure 2.20: Example of CSL notation for two different GBs. The repeating structural unit in each case is outlined in black [95].

When studying the effect of grain boundaries on macroscopic behavior, it's important to consider multiple types of boundaries. Although each individual GB has an effect on behavior, it is the collective effect of all GBs together that dictate large scale behavior. In this study, multiple grain boundaries are studied for their transport properties, such that comments can be made about graphite's macroscopic performance in battery anodes. Here, only tilt grain boundaries will be considered in order to maintain the integrity of graphite galleries. If twist boundaries were considered, galleries in each half of the bi-crystal would not align, thereby severely inhibiting transfer between crystals. Details on the creation of grain boundaries for this study will be discussed in a later section.

2.4 Computational Methods

2.4.1 Atomistic Simulations

The study of atomic motion and interactions have long been of interest to the scientific community, as it provides insight into the unseen world; it sheds light on the underlying mechanisms that control macroscopic behavior. Before the advent of computer simulations, researchers in the 1930's used gelatine spheres in an attempt to simulate the motion of a liquid and did so quite successfully [5]. However, despite the apparent accuracy of these

first studies, they were never able to neglect the effects of gravity and it was hypothesized that numerical solutions would prove more useful than physical representations of atomic systems.

The earliest computational work in atomistics was performed by Metropolis *et al.* at Los Alamos National Labs on MANIAC and served as the basis for Monte Carlo (MC) simulations, which allowed for the first time, connections to be made to experiments via thermodynamic output data [5]. As simulations continued to advance with ever increasing computing power, Molecular Dynamics (MD) entered alongside MC methods to form the current realm of atomistic modeling. Figure 2.21 details the role of computer simulations in scientific research and discovery.

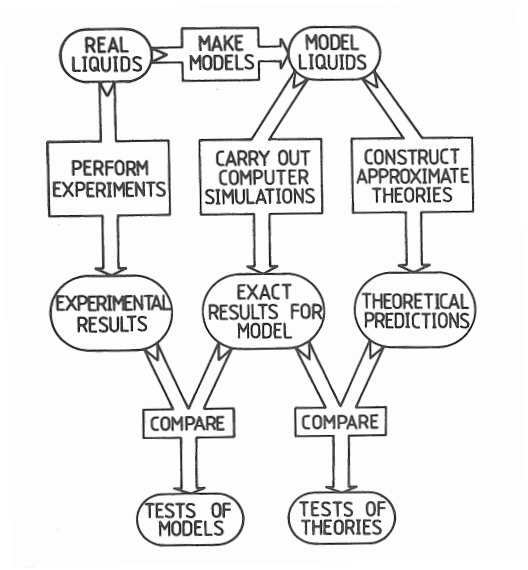

Figure 2.21: The role of computer simulations in modern scientific research [5].

Models are based on their real world counterparts and the properties that dictate these models can vary based on the intent of a study. Even today, most models will not inherently capture all behavior of a physical system, but rather small pieces of the bigger picture. Still, these models provide valuable information to researchers. Once models are created they can be used in one of two ways. First, simulations may be carried out and compared to experiments to verify the accuracy of the previously constructed models. Second, the model can be used as a test of hypotheses for various systems. For example, the work presented

here is testing the theory that grain boundaries are a source of diffusional variability in graphite. While the resulting model may match experimental data closely, the goal is rather to understand the differences and intricacies of said systems relative to one another. This is a test of *relevant theory* rather than the model. However, Chapter 3 investigates aspects of the model relative to experiment to verify its correctness and provide input for improvement.

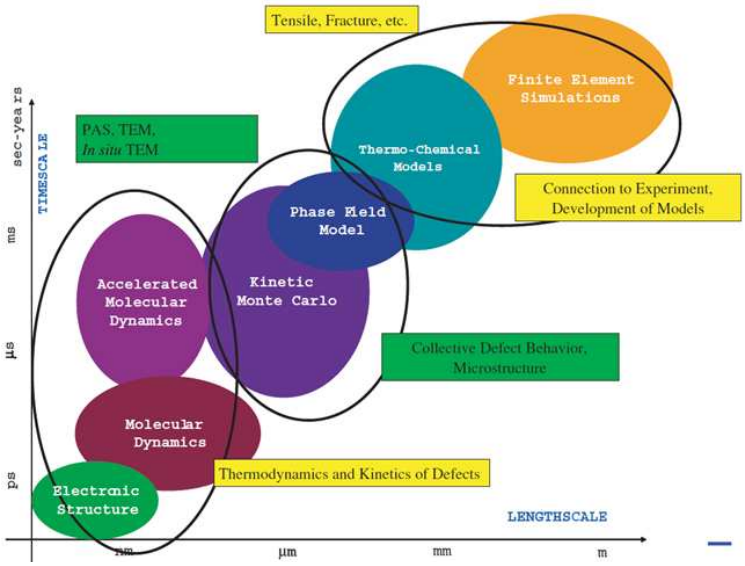

Figure 2.22: Computational modeling techniques as a function of length and time scales with possible applications [64].

MD simulations are highly appropriate for this work as the goal is to understand material differences, specially grain boundaries and their role in mass transport. Grain boundaries are on the order of nanometers to micrometers in length and thus first-principles calculations such as Density Functional Theory (DFT) are not practical in those length scales for their computational expense. While DFT may represent the Lithium-Carbon interactions with greater accuracy than the interatomic potentials used here, the computing time would far exceed the usefulness in establishing GB diffusion data. The ability of MD to provide constant trajectory information allows for transport processes to be broken down into step-by-step pieces leading to an intricate understanding of long-range atomic motion over time. While MD sounds like an unparalleled method for atomic-scale calculations, model assumptions and computational accuracy limit its usefulness in exceedingly

large simulations. Figure 2.22 details current computational modeling approaches as function of their applicable time and length scales. This dissertation addresses multi-scale issues in that there is concern over equilibrium structures, such as those determined by ab initio (electronic structures) as well as diffusion (MD/KMC), and defect behavior (MD). However, with careful thought into assumptions and considerations from other scales, MD studies provide a wealth of knowledge on Li transport mechanisms especially as they relate to inherent crystal structure.

Molecular Dynamics is rooted in the idea that particles within a certain distance to one another will interact and thus have a force and energy between them [32]. This force is related to the separation distance, r of the two particles through the interatomic potential, which defines the potential energy U of the system. The connection to force between each set of particles is:

$$F(r) = -\frac{\partial U(r)}{\partial r} \tag{2.15}$$

and is applied to all sets within a cutoff radius (for simulations), which is determined *a priori*. The choice of the interatomic potential is not random and is related back to the establishment of a proper model. These potentials take careful consideration such that the important parameters for the study are captured correctly. The simplest form is a pair-potential, which is aptly named for its role in computing the energy between sets of particles. The Lennard-Jones potential, as seen in Figure 2.23 is a widely used example of a pair potential and takes the form,

$$U(r) = 4\epsilon\left(\left(\frac{\sigma}{r}\right)^{12} - \left(\frac{\sigma}{r}\right)^{6}\right) \tag{2.16}$$

where ϵ is the depth of the potential energy well and σ is the point at which the energy is equal to zero [44, 5]. In simulations, it is not uncommon for interactions of sets of elements to be described by separate interatomic potentials. For example, if one potential form is used for interactions between elements of Type X, another could be used for Type Y. Yet another potential could describe the interactions between the two elements (totaling three

separate interatomic potentials). The selection of interatomic potentials for this work will be discussed in depth later on.

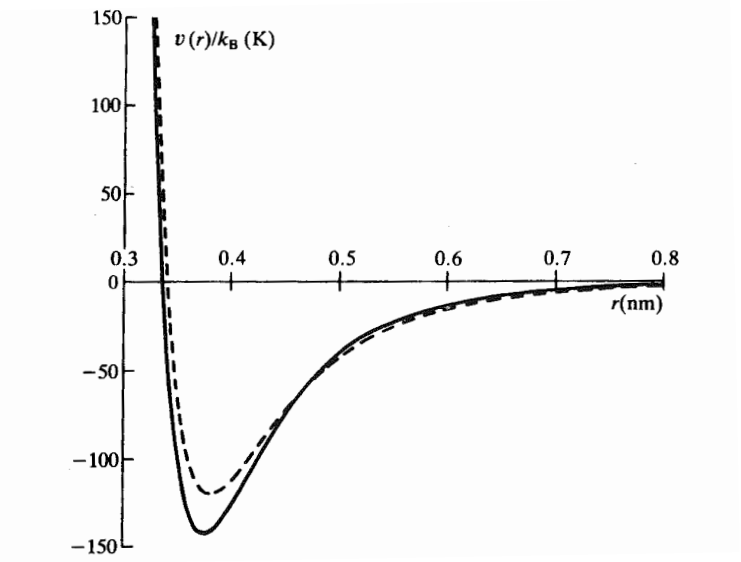

Figure 2.23: Lennard Jones pair-potential (dashed-line) for liquid argon simulations [5].

2.4.2 Molecular Dynamics

MD can be thought to closely model experiments, in the method with which simulations are performed [32]. A model is created, analogous to a physical sample, the sample is then prepared (the system is equilibrated), and then an experiment is run and data collected. If equilibration or preparation is handled incorrectly, the collected data could be wrong or at the very least unreliable in either case. Accordingly, great care should be taken not only in running simulations, but also with the processes that are used to set up and equilibrate the desired systems.

The majority of the work within this thesis was completed using MD techniques, which are based on the aforementioned relationship between interatomic potential energy and force. However, to model dynamics, particle positions and velocities must be computed. Since the masses of each particle are known (based on atomic weights), Newton's Second Law of Motion can be applied to determine velocities or in other words, the trajectories of the particles such that new positions at a time $t + \delta t$ can be established. To solve the

position at new time, Newton's second law is integrated numerically (by finite difference approximations), however this requires the previous two atomic positions as initial conditions [32]. Instead, the Velocity Verlet method is used in which the acceleration, velocity, and position at time t are known and used to compute values at the next step in time, some δt ahead. Regardless of the method used, once the new variables are computed, several other quantities can be calculated that are of use in post-processing analysis of the system.

For MD computations, the state of a system is identified by the positions $(q_1 \dots q_N)$ and momenta $(p_1 \dots p_N)$ of a set of particles, either atoms or molecules, whose electronic properties are not directly considered [5]. Thus, for a system of N particles with masses m_i, a classical description can be formed by the Hamiltonian, $\mathcal{H}$, which describes the total energy of the system as a sum of kinetic and potential energies, as shown in Equation 2.17.

$$\mathcal{H}\left(\mathbf{q},\ \mathbf{p}\right) = \mathcal{K}\left(\mathbf{p}\right) + \mathcal{V}\left(\mathbf{q}\right) \tag{2.17}$$

Subsequently, the kinetic and potential energy of the system are represented by,

$$\mathcal{K} = \sum_{i=1}^{N} \sum_{\alpha} p_{i\alpha}^2 / 2m_i \tag{2.18}$$

$$\mathcal{V} = \sum_{i} v_1\left(\mathbf{r}_i\right) + \sum_{i} \sum_{j>i} v_2\left(\mathbf{r}_i,\ \mathbf{r}_j\right) + + \sum_{i} \sum_{j>i} \sum_{k>j>i} v_3\left(\mathbf{r}_i,\ \mathbf{r}_j,\ \mathbf{r}_k\right) + \dots \tag{2.19}$$

The kinetic energy is directly related to the momenta of all particles in the system, while the potential energy is constructed from particle interactions based on position. System temperature is directly related to the kinetic energy. The first term in the potential energy equation describes any external forces acting on the particle, whereas the rest are interaction terms, which will be described in detail later. For computational efficiency, the potential energy term is usually truncated after the three-body interaction term, thus resulting in an effective interatomic potential energy, V_{eff}. From the Hamiltonian, equations of motion for the system are derived (as mentioned above) which dictates overall behavior of the set of particles. Finally, it is important to note that, the time derivative of the

Hamiltonian is zero, and thus energy in the system is conserved.

In MD calculations, it's easily shown that the number of atoms in the system can quickly grow into the billions if the model is trying to capture larger scale behavior. As the number of particles in the system grows, so does the computing time required to solve Newton's equations of motion. Additionally, if systems terminate a given distance away from the simulation box center, edge and surface effects must be considered, further complicating MD simulations. To combat these issues and still provide useful information regarding physical systems, MD simulations employ the technique of periodic boundary conditions (PBCs) show in a 2-D representation in Figure 2.24. Here, the shaded region of dimension L^2, is the actual simulation space which contains all the atoms in the current simulation. Atoms in boxes A-H represent the images of each atom, 1-5, in the shaded region and move in the same manner. It's worth noting that the properties of such images do not need to be stored, but rather this diagram is strictly for visualization purposes. Should an atom in the central region move out of the shaded box and into an outside position, that atoms image will take its place, as shown with Atom 1. The position of the new atom image in the simulation cell will be a distance L away from the last known position of the original atom.

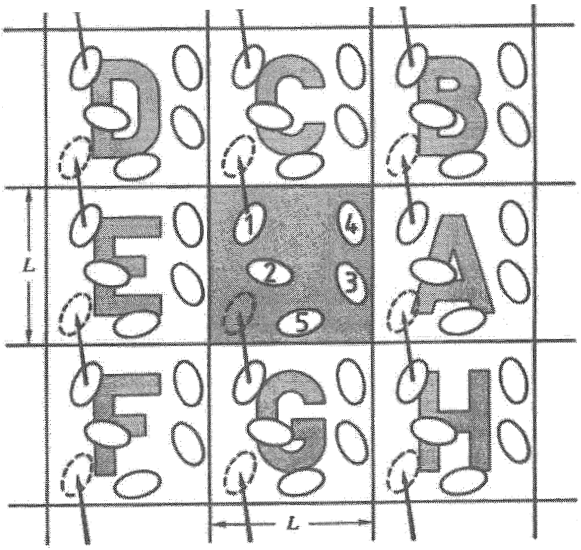

Figure 2.24: Diagram of periodic boundary conditions for atomistic simulations. The central gray box in the actual simulation space where the lettered spaces A-H represent the periodic images of atoms [5].

An impending question is how large must the central region be such that it correctly models the intended physical behavior? One of the main driving factors is the cutoff radius of the interatomic potential. Forces are computed for any pair of atoms within this radius and if the simulation space is on the same order of magnitude or smaller than this radius, forces will be computed between an atom and its own image, obviously a non-physical quantity. A general guideline established for liquids is that any dimension L of the simulation cell should be no smaller than 6σ in order to prevent this self-imaging phenomena [5]. Further complications arise when potentials have long-range interactions to consider, which is discussed in depth in Ref. [5].

When performing MD simulations, the above information is all pertinent however it does not fully relate these systems to macroscopic quantities such as pressure and temperature. To accomplish such a relationship, ensemble averaging is performed. For this work, several different ensembles are used, including the micro-canonical (NVE), canonical (NVT), and isothermal-isobaric (NPT) ensembles. N represents the number of particles in a system, V is the system volume, E is total energy, P is total pressure, and T is of course temperature. For each of these ensembles, the variables in parentheses are held fixed while others allowed to fluctuate, representing a connection to macroscopic experiment. For example, an experiment may be performed under constant P and T, which is commensurable to the canonical ensemble.

Beyond MD, another computational method used in this work are energy minimizations, which are a form of Molecular Statics (MS). When constructing atomic systems for computation, there is no guarantee that the as-built positions will correspond to the minimum energy configuration for the system. Therefore, energy minimizations are performed prior to enabling dynamics such that the system starts at a minimum energy. For this study, the conjugate gradient method is used, such that new atomic positions are calculated from known interatomic potentials and previous atom locations [69]. The stopping criteria for a given minimization can either be the energy tolerance or interatomic force between atoms.

There are many MD codes available for use including AMBER, CHARMM, and GRO-

MACS some of which are open-source while others are not. This work solely uses LAMMPS, the Large-scale Atomic/Molecular Massively Parallel Simulator developed by Steve Plimpton at Sandia National Labs [73]. LAMMPS, as its name implies, has great application to parallel computing, which is the focus of this work, utilizing Lehigh's Corona cluster. In addition, versions of LAMMPS in recent years include many advancements in user control over their predecessors including atomic deposition, which proves very useful for the studies to be discussed in later chapters. While not used directly in this thesis, it is necessary to highlight the advantages and important features of Monte Carlo methods, which are frequently used when studying material systems.

2.4.3 The Monte Carlo Method

As seen in Figure 2.22, Monte Carlo methods handle system sizes (both in time and length scale) that are slightly larger than MD. MC simulations are aptly named for their heavy use of random numbers, specifically to determine probabilities of specific outcomes over many trials [5]. For molecular systems, MC methods use equilibrium statistical mechanics and the associated Boltzmann probabilities to determine states of systems, whereas MD, does as the name implies- models complete system dynamics. When comparing the methods on similar time and length scales, one is not better than the other, rather the needs of the researcher dictate the best practice for the application.

Figure 2.25 dictates a simple example of the MC algorithm in which darts are thrown at a surface. Here, random sets of coordinates are chosen such that they lie in square OABC and may be contained within the circle OAC. If they are contained within the circle they are considered a 'hit'. Therefore, for some total number of shots attempted, τ_{shot}, there is an associated success numbers, τ_{hit}. From this and the given relationship between the areas of OABC and OAC, the following can be deduced,

$$\pi \approx \frac{4 \times Area\ of\ OAC}{Area\ of\ OABC} = \frac{4\tau_{hit}}{\tau_{shot}} \tag{2.20}$$

This approximation will continue to grow in accuracy as the number of shots taken increases. In this trial, π was correctly estimated to 4 digits after 10^7 shots [5]. While

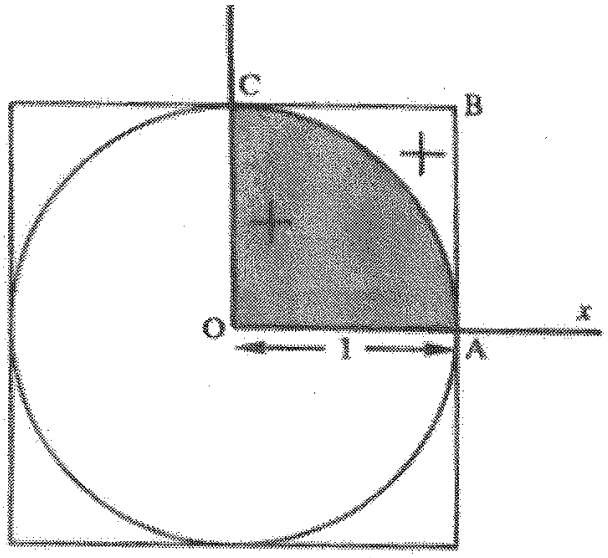

Figure 2.25: Example of the application of Monte Carlo methods for approximating π [5].

this is a straightforward trial, it underlines the importance and key to MC methods- the process of choosing random numbers from a uniform distribution. Details of this process are available at length in Ref. [5]. In relation to physical systems, MC methods use elementary system changes, including changes to an atoms position, atomic swaps between two particles, or adjustment of the simulation space to probe changes in potential energy. Figure 2.26 shows one possible change in a system, where an atom, r_i in State m is moved to a new State n by changing the atom's position. The probability of any given state from the state space occurring is dictated by Equation 2.21. The state space is the collective set of all possible outcomes, Γ, in the system.

$$p_i = \frac{e^{\frac{-\epsilon_i}{kT}}}{\sum_{i=1}^{M} e^{\frac{-\epsilon_i}{kT}}} \tag{2.21}$$

Such changes are accepted if doing so lowers the potential energy ($\delta V \leq 0$) of the system. Additionally, if the move raises the system's energy ($\delta V > 0$), it can be accepted if it meets a probability requirement. Here, the energy difference between the two states in question is calculated and the probability ratio ρ_n/ρ_m, established. Subsequently, a random number ξ is generated and if ξ is less than the probability ratio, the move is

accepted, otherwise it is rejected. This theory is illustrated in Figure 2.27.

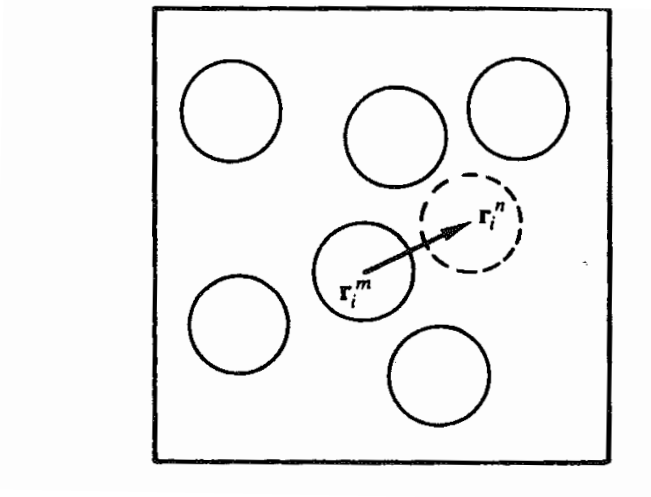

Figure 2.26: One possible MC move to change the state of the system [5].

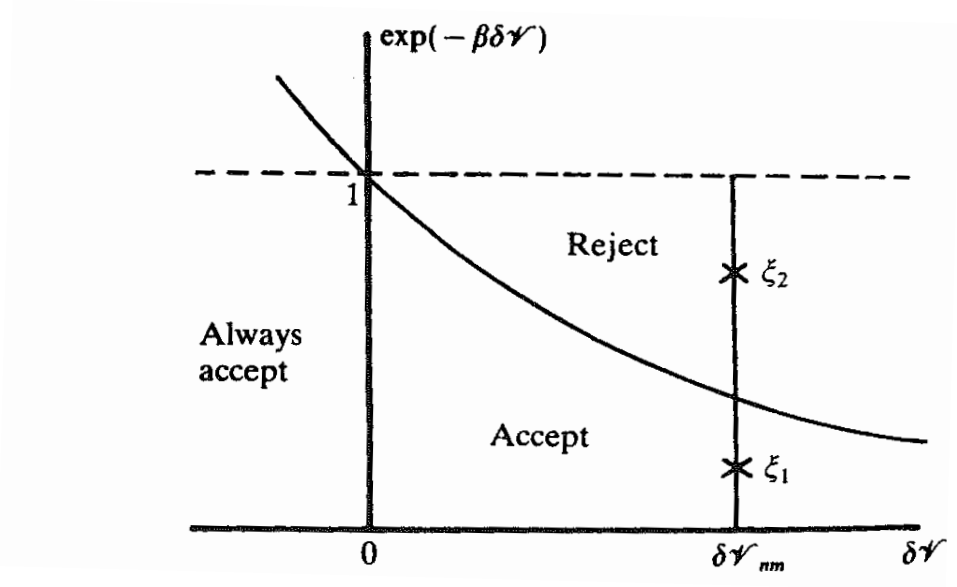

Figure 2.27: Probability that a move from state m to n is accepted during a simulation [5].

MC methods are very useful in quickly and efficiently sampling the equilibrium positions of a system. Beyond traditional MC, there are methods that mend MC with other simulation techniques such as quantum calculations. Additionally, although MC by trade does not model dynamics, they can be estimated via Kinetic Monte Carlo, in which the rate characteristics are known *a priori*.

Like mentioned above, the entirety of this research study utilizes Molecular Dynamics

(with limited Molecular Statics) simulations to study mass transport. It is not out of the question though that future work in this project considers MC methods to bolster the trends observed with MD. The remaining sections in this Chapter address the interatomic potentials which are necessary for correctly calculating potential energy of simulations. These potentials are also applicable to MC methods in a similar manner.

2.4.4 AIREBO Potential

Early simulations in MD studied metallic interactions and dynamics of liquids. However, that represents only a small percentage of physical interactions in the world of materials science and chemistry. Covalently bonded systems such as silicon and graphite cannot be described by simple pair-potentials developed early in the history of MD and the need for more advanced multi-body potentials arose (i.e. considering additional terms in $\mathcal{V}$). Although several iterations and hypotheses had been formed regarding how to correctly and efficiently model such systems in MD, Jerry Tersoff is credited with creating the useful form [92, 90, 91]. Originally formulated using silicon because of its numerous polymorphs with rather similar cohesive energies, it incorporates the dependence on bond-order to described covalent systems [91]. Bond-order is defined as the number of bonds between two atoms; three for carbon atoms in graphite. In its most basic form, the Tersoff potential is as follows

$$E = \sum_i E_i = \frac{1}{2} \sum_{i \neq j} V_{ij} \tag{2.22}$$

$$V_{ij} = f_C(r_{ij})[a_{ij} f_R(r_{ij}) + b_{ij} f_A(r_{ij})] \tag{2.23}$$

where V_{ij} describes the bond energy of the system. Notably, the b_{ij} term shown above controls all of the advanced bonding characteristics of covalent systems. This includes coordination numbers (number of nearest neighbors), bond angles, and conjugate effects [91]. It is important to note that the Tersoff-type potential by nature includes no quantum mechanical effects or considerations, even though the potentials include information

regarding bond-order. This hybridization effect rather comes from the geometry of the system and considers electric degrees of freedom empirically [85]. To calculate hybridization in MD with such potentials, one simply needs to know the equilibrium bond length of the potential and material at which point nearest neighbors can be found.

Derived from the Tersoff-type potential is the Reactive Empirical Bond-Order (REBO) potential developed by Brenner:

$$E_{ij}^{REBO} = V_{ij}^{R}(r_{ij}) + b_{ij}V_{ij}^{A}(r_{ij}) \tag{2.24}$$

Here V_{ij}^{R} and V_{ij}^{A} represent the repulsive and attractive pair potentials, respectively. Stuart notes that the REBO potential describes intramolecular interactions extremely well because of the method of handling bonds, but fails to correctly capture intermolecular interactions seen in many hydrocarbon materials [85]. Thus, to capture such intermolecular interactions, Stuart chose to expand on the original potential and renamed it the Adaptive Intermolecular Reactive Empirical Bond Order (AIREBO) Potential. To start expanding on the original work, Stuart chose to integrate a Lennard-Jones potential with the existing REBO potential, in the following form:

$$V_{ij}^{LJ}(r_{ij}) = 4\epsilon_{ij}\left[\left(\frac{\sigma_{ij}}{r_{ij}}\right)^{12} - \left(\frac{\sigma_{ij}}{r_{ij}}\right)^{6}\right] \tag{2.25}$$

While this will enhance the existing potential in terms of intermolecular forces, it should be noted that the LJ component will interfere with REBO at short distances. For example, if two atoms were to form a covalent bond according to the REBO potential, their close proximity may impinge on the repulsive wall of the LJ potential, thereby preventing the bond from forming. To combat this, switching functions were implemented such that the LJ component of the AIREBO potential would act only if certain conditions are met. First, minimum and maximum LJ interaction distances are set where the Lennard-Jones component is turned off below r_{min}^{LJ}, taken as σ_{ij} for AIREBO, and again at r_{max}^{LJ}. Second, another switching function is implemented based on the bonding conditions established by the REBO component. If two atoms in questions are likely to establish a covalent bond,

related back to the b_{ij} term in the original potential, the repulsive LJ interactions will not be active. Conversely, if such bonding is unlikely, the atoms will indeed experience LJ repulsion. Finally, if atom pairs in question are first or second neighbors, LJ interactions are not present because of how well REBO describes such bonding configurations. Each of these three cases are crucial to meshing intramolecular and intermolecular interactions and it should noted that care has been taken by Stuart to ensure the potential remains smooth and continuous under the cutoff distance.

The final addition Stuart made to the existing REBO potential was a torsional term, as Brenner's original potential focuses on network solids and lacked any torsional interactions [85]. Torsional considerations are important depending on the compounds of interest because a rotation of a single bond in a molecule is associated with an energy change comparable to standard thermal energies [5]. Since the original purpose for the development of AIREBO was for applications to hydrocarbon chains, the torsional effects about single bonds must be considered and are done so in the form:

$$V^{tors}(\omega) = \epsilon \left[\frac{256}{405} \cos^{10} \frac{\omega}{2} - \frac{1}{10} \right] \tag{2.26}$$

This differs from traditional incorporations of torsional potential energy because AIREBO by nature is a bond-order potential. It therefore must consider local environment of the molecule as opposed to a general parameter for the entire simulation [85]. After considering the addition of torsional effects, the complete AIREBO potential is:

$$E^{AIREBO} = \frac{1}{2} \sum_{i} \sum_{j \neq i} \left[E_{ij}^{REBO} + E_{ij}^{LJ} + \sum_{k \neq i,j} \sum_{l \neq i,j,k} E_{kijl}^{tors} \right] \tag{2.27}$$

where indices i,j,k, and l represent atoms in the system.

While the intended application is for hydrocarbons, much of the parametrization for AIREBO occurred using graphite, which is the focus of this study. Therefore, there was ample data with which to compare when implementing the potential in LAMMPS. One of the most important parameters in terms of fundamental crystal construction is the equilibrium lattice constant. For graphite, Stuart reports an out-of-plane lattice constant

of $c = 6.7080$ Å at $T = 298$ K and a bond length of $r_{cc} = 1.396$ Å [85]. LAMMPS in its current form does not support long-range tail corrections for AIREBO, which are van der Waals interactions added to combat the effects of potential cutoffs and PBCs [86]. Hence, the equilibrium lattice and bonding distance for this study vary slightly, with $c = 6.8391$ Å and $r_{cc} = 1.41$ Å at $T = 300$ K. This difference results in a 1.95% expansion over the AIREBO potential as developed. Although there is a slight deviation in lattice constants, the energy per atom of carbon in graphite shows excellent agreement ($error \approx 0.06\%$) with Stuart calculating $E_c = 7.47164$ eV against $E_c = 7.4765$ eV calculated here.

2.4.5 Lithium Interactions

While the AIREBO potential serves as a crucial component of this work, it only represents one of three interatomic potentials necessary for describing the Lithium-Carbon system studied here. Graphite and its associated interatomic potentials are well-described like discussed above. However, the Li-C system, especially in MD, is not as clear cut. Ideally, Li-C interactions are modeled using dynamic charge transfer, which incorporates quantum effects like the work by Ohba *et al.*. However, for computational efficiency this work utilized existing empirical potentials developed for lithium-carbon pairs. More specifically, pair potentials developed for application to Li transport in carbon nanotubes were used and subsequently optimized for the goals of this thesis. Full details regarding interatomic potentials for Lithium-Lithium and Lithium-Carbon interactions will be discussed at length in Chapter 3.

2.5 Grain Boundary Structure

2.5.1 Misorientation Angle Selection

Grain boundaries, although found in abundance in reality, pose unique challenges for the modeling community. Like mentioned previously, they form naturally when two or more crystals of the same phase meet. This process as a whole is extremely complicated to model and thus boundaries are created artificially. This does not however affect the ther-

modynamics or structure of the boundary, provided care is taken in constructing each boundary. The challenges of creating such GBs in MD simulations is presented in the following sections, with specific examples of how GBs were created for intercalation and diffusion simulations performed here.

For this study, it was necessary to create several different grain boundaries to evaluate the possible range of diffusion characteristics. For computational efficiency and ease, we chose to create symmetric twin-tilt grain boundaries like the one seen in Figure 2.28. In this orientation, one graphite crystal is rotated about an axis perpendicular to the $\langle 0001 \rangle$ basal plane relative to the other half crystal. In our simulations, this axis, noted as the $\langle 0001 \rangle$ axis in Bravais notation, was aligned with the z-axis of our simulation cell in LAMMPS. To differentiate each boundary, we define a misorientation angle α which is the angle necessary to rotate one half crystal into alignment with the other. Based on GB diffusion work by Kofke *et al*, we chose to model five unique values of α.

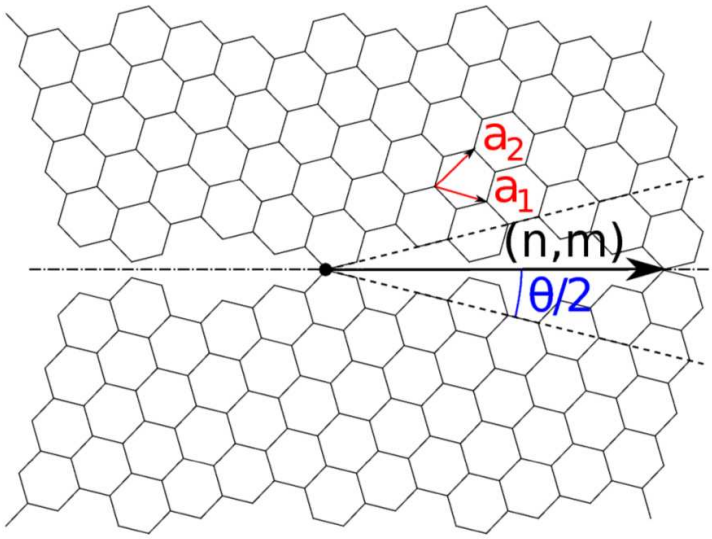

Figure 2.28: Example symmetric-twin tilt grain boundary in one plane of graphite. Vectors a_1 and a_2 correspond to the two in-plane lattice vectors while (n, m) defines the rotation angle, label here as $\theta/2$ [13].

A program was written to create the symmetric twin GBs in which a large plane of carbon atoms was mapped to the positive XY plane. Any carbon atom in the plane could be selected and a vector was drawn from the origin to said atom, indicating one edge of the

rotated graphite lattice. This is partially detailed in Figure 2.29, where the graphite unit cell is shown in the lower left, along with several repeated lattices. The coordinate (n, m) dictates a position somewhere in the lattice away from the origin of the original unit cell. As shown, $(n, 0)$ lies along the x axis and does not signify a rotation vector. Instead, if some orientation, say (n, n) was chosen, the new lattice would be oriented at 45° to the original unit cell. In reality, grains of any size come together to form a grain boundary. The macroscopic material sample has surface and edge planes, which have unique characteristics from the the lattice and GBs. In MD, these surface effects are unwanted when studying bulk grain boundary properties and need to be avoided. With periodic boundary conditions, care must be taken such that grains appear to be of infinite extent such that surface and edge effects do not manifest. This is accomplished by creating grains that reside perfectly within an orthogonal cell.

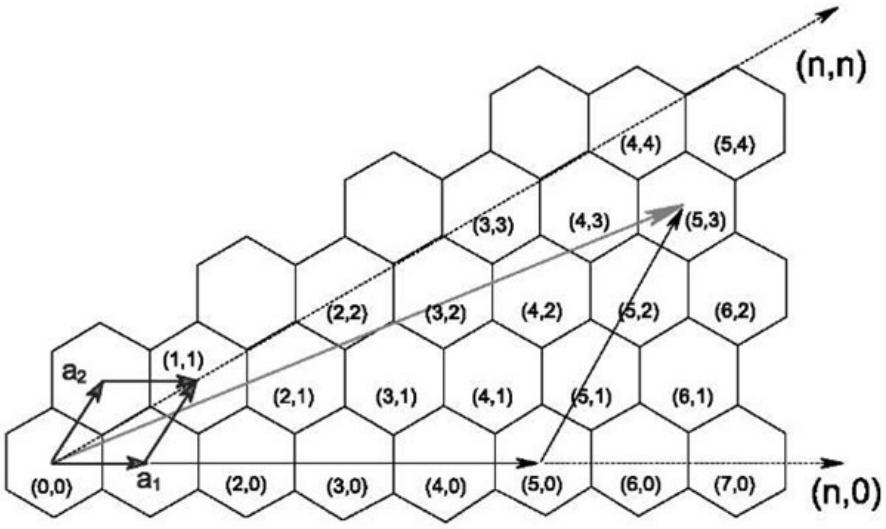

Figure 2.29: Schematic showing the graphite unit cell in the lower left and a repeated graphite lattice. Selection of two multiplication factors allows for any set of rotation vectors for creation of a grain boundary [23].

Since the goal was to create such a cell for use with LAMMPS, the program created a second vector at 90° to the first and searched for any atom that fell along its path, within a certain tolerance, taken as 10^{-04} Å in this case. If a match was found, this signified that a set of orthogonal vectors exist, and a rotated unit cell could be formed. It is important

to note that *any* rotation vector (n, m) could be chosen to form a rotated graphite crystal. The limiting factor, as with many things in computer simulation, is the the size of the simulation cell. For example, suppose a rotation vector was chosen such that $n \gg m$ along a perfect lattice, corresponding to a very small value of θ. Given the size of a hexagonal graphite ring, the distance to reach another atom that would represent the periodic pair of the original atom, would be very large. In other words, the simulation cell would need to be sizeable, to the point where computational expense starts to be an issue. To avoid this problem, a maximum size was chosen for rotated crystal unit cells. This way, any set of vectors that are found will be of reasonable size for the goals of this study. If computational limits are not an issue, an infinite array of boundaries can be constructed, which will be discussed later.

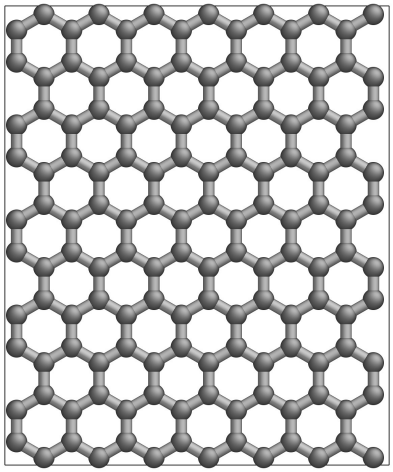

Figure 2.30: Two-dimensional image of one graphite plane to show bonding configuration. Notice there are two configurations present in the lattice and the plane has six-fold symmetry.

When two orthogonal lattice vectors are found, a secondary check of atomic configuration occurs. Carbon atoms and their neighbors take on two arrangements in a graphite lattice as seen in Figure 2.30. For a central atom, there can be a NN directly above or below it in the y direction at a distance of 1.41 Å. Opposite that, are two additional atoms, 120° apart and offset in the x direction. Based on periodic boundary conditions, the atom at the origin will be mirrored at the other 3 corners and thus the atoms dictating the other corners of the rotated unit cell must have the same arrangement as the original atom. If it

does not, the program will not count the new atom as a successful pair and thereby restart the search.

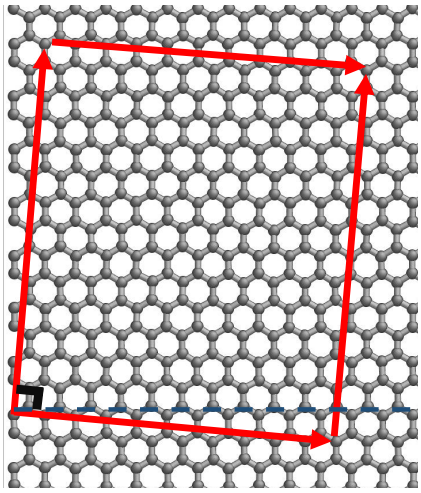

Figure 2.31: Atomic positions of a rotated unit cell along with the unit cell vectors that complete an orthogonal box required for simulations in LAMMPS for a low-angle GB.

Once two successful vectors have been located with endpoint atoms having the same orientation as the origin atom, an orthogonal box can be formed by adding two new vectors, each parallel to the first two. Now, any atom that lies within this cell is kept while any atom positions lying outside are discarded. It is important to note that any atom lying along the original two vectors is kept but those on the final two are discarded. This again is related to periodicity as the first two vectors actually symbolize mirrored lines of the second two. Figure 2.31 shows an example of a successfully created orthogonal lattice, with the red vectors marking edges of the new orthogonal unit cell. Although visually one graphite layer is shown, the above process is applied to two graphite planes. The graphite unit cell contains atoms in two planes because of the ABAB stacking sequence and thus the two layers must be considered simultaneously. An alternative method would be to create a single rotated graphite plane and then create a second plane of carbon atoms at $+c/2$ with a translation along the a_2 unit vector.

This orthogonal unit cell is then rotated by negative θ to align the rotation vectors with the global x and y directions. Now, the cell can be repeated in any direction to form a graphite crystal of any size with a rotated unit cell with misorientation angle, θ.

2.5.2 Grain Boundary Construction

The lattice created above is equilibrated under a canonical ensemble at $T = 300$ K and behaves the same way as a crystal built without applying any misorientation would. In principle, LAMMPS does not see the two any differently, as long as the crystal is periodic in the three orthogonal directions. If this periodicity is violated for any reason, atoms on the lattice could lie either closer or farther from their equilibrium positions, resulting in artificial stress and strain. If the program to create rotated unit cells incorrectly selected a set of rotation vectors, the equilibration would expose such faults.

At this point, a symmetric-twin GB can be formed. To do so, the equilibrated atomic positions are mirrored across the right-most edge of the simulation cell (in the x direction), such that each atom in the original cell now has a second atom in the new cell, which is a mirrored image of itself. This process has created a grain boundary located at $x_{max}/2$ in the new simulation box. However, periodicity once again comes into play so we in fact have a second boundary located at x_{max} or simply $x = 0$.

There are a few intricacies about these GBs worth noting. Firstly, when the GB was produced, there is no guarantee that atoms lying at either GB are at their respective equilibrium bond length from their nearest-neighbors. Secondly, there is no guarantee that the boundary formed is a minimum energy structure since no dynamics have been considered- the boundary was created out of artificial means. To remedy both issues, the procedures of Olmsted *et al.* are followed [68, 40].

In this procedure, one half of the bi-crystal, labeled 'A' in Figure 2.32 is held fixed while crystal 'B' is shifted systematically in the x and y direction. For these simulations, the step size was to be no larger than 1.41 Å which is the equilibrium bond length for graphite in our model. If, after completing the shift, any atoms in y have exceeded the box dimensions in that direction, they are wrapped back into the simulation cell by the distance ΔY. The x direction is slightly more complicated but follows the same principle. If any atom exceeds the maximum x position of the cell, it is wrapped through the periodic bound a distance of $\Delta X/2$ such that atoms are returned to the cell at the central GB and remain part of crystal 'B'.

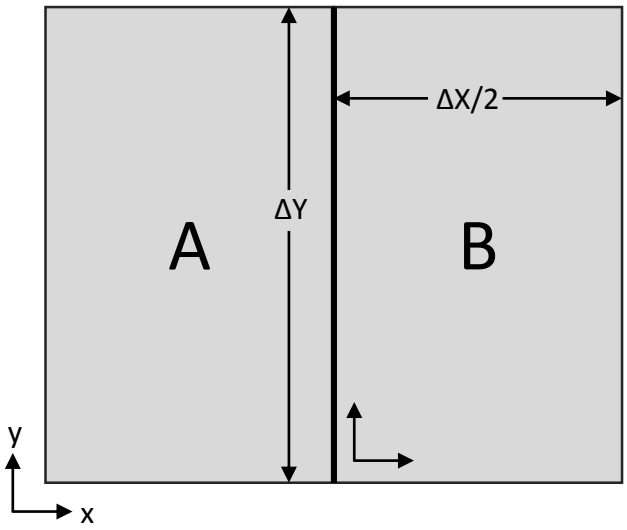

Figure 2.32: Schematic showing the grain boundary creation procedure used in this work. Grain B is shifted in the x and y directions through the periodic boundary of the half crystal and then the structure is minimized to find the lowest energy configuration.

Next, the issue of atomic overlap at the GB must be addressed. If atoms lie much closer to one another than their equilibrium bond length, the forces between these atoms will be highly repulsive as noted by the interatomic potentials, which could result in atoms being ejected from the simulation cell. Before minimizing the shifted structure, LAMMPS checks for atoms that lie within a user-defined separation distance from one another and if such a case is present, one atom from the pair is deleted. At first glance, there is no intuition in choosing the deletion criteria, thus work was done to probe the dependence of system stability on this distance. It is well understood that if the deletion criteria is greater than the bond length, atoms away from the grain boundary would be removed from the system. Contrary to this, if the deletion criteria is too small, atoms will remain in close proximity to one another and the large localized compressive stresses will not be abated.

Therefore, a procedure was put in place to perform three separate energy minimizations on the boundary structures instead of one. Three overlap distances, d were chosen; $d = 0.75,\ 1.0,\ 1.25$ Å to offer a range of equilibrium structures. Each structure was minimized using the conjugate gradient approach and the GB energy calculated according to equation 2.28.

$$\sigma = \frac{\partial U}{\partial A} \tag{2.28}$$

The GB energy, σ is defined as the internal energy of the boundary per GB unit area [51]. During MD simulations, our reference state is a carbon atom in bulk graphite single crystal, computed as $E_C = -7.4768$ eV. Additionally, periodic boundary conditions lead to the creation of two grain boundaries, therefore, the GB energy equation becomes:

$$\sigma = \frac{E_{Total} - E_{Graphite}}{2A} \tag{2.29}$$

where $E_{Graphite}$ is the product of E_C and the total number of atoms, N_C in the grain boundary system. Regardless of misorientation angle, the $d = 0.75$ Å case resulted in the minimum energy configuration every time, as seen in Figure 2.33. One possible explanation is that as the atomic separation at the boundary grows, strains are induced at the boundary, causing higher energies. Concurrent to the Olmsted procedure, several other methods were tried to understand their effect on GB structure and equilibrium. One procedure involved the deletion of atoms selectively at the grain boundary, which sit closer than 1.5 Å from their nearest neighbor. This created a large tensile stress perpendicular to the boundary plane, which was removed by artificially inducing a compressive strain in the same direction. While this procedure produced a near zero net stress, there was not sufficient reasoning toward the strains induced and the procedure was abandoned for the more rigorous and supported Olmsted approach.

Once the minimum energy configuration was found, the GB was constructed using the aforementioned procedure and equilibrated under the canonical ensemble at $T = 300$ K. For intercalation studies, this was done with a free surface present in both positive and negative z direction, whereas GBs for diffusion studies did not include a free surface.

In practice, there is no guarantee that the observed structure is the absolute minimum energy configuration, thus this study probes the dependence of transport on GB energy by pursuing simulations of both low and intermediate energy GBs. Table 2.5.2 describes each of the grain boundaries tested, arranged by α.

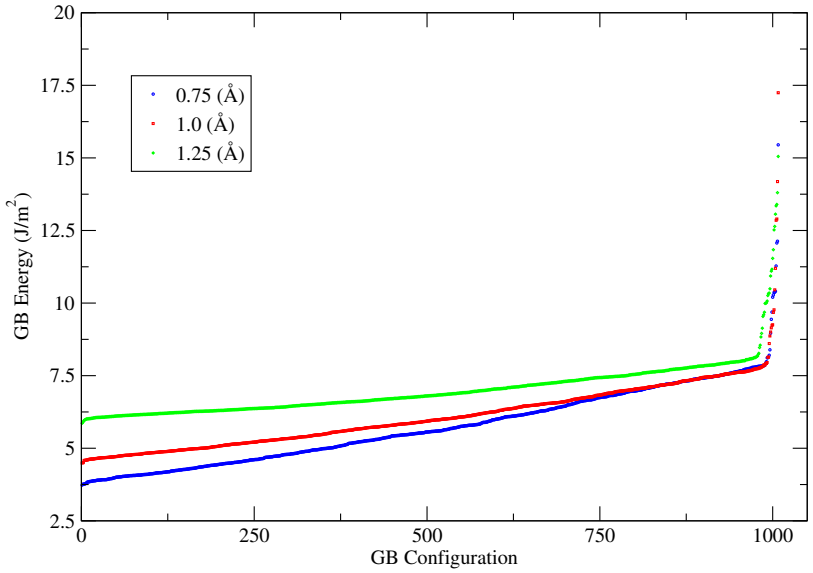

Figure 2.33: Grain boundary energy versus configuration iteration for 3 separate atomic deletion criteria at the $\alpha = 8.26°$ boundary, sorted by lowest energy.

Table 2.2: Grain boundary geometric details for all MD simulations.

α $(Deg.)$	x (nm)	y (nm)	z (nm)	N	σ $\left(J/m^2\right)$
8.26	11.6	13.4	3.4	61526	5.712
8.26	11.6	13.4	3.4	61710	3.731
9.44	15.3	8.8	3.4	53240	3.989
9.44	15.3	8.8	3.4	53252	3.658
21.79	11.1	10.2	3.4	44782	4.696
21.79	11.1	10.2	3.4	44764	4.558
29.60	29.5	25.5	3.4	297723	5.983
29.60	29.5	25.5	3.4	297813	3.813
30.16	11.3	6.5	3.4	28902	4.842
30.16	11.3	6.5	3.4	28926	3.789

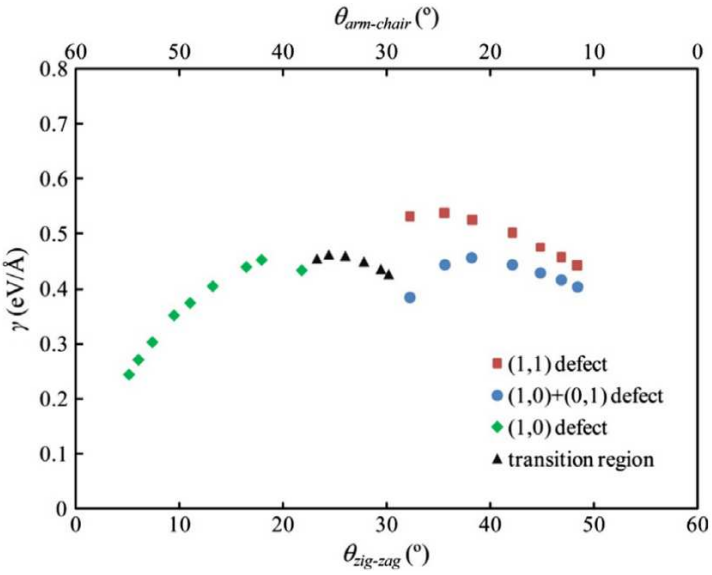

Figure 2.34: Graphene grain boundary energies as a function of misorientation angle [54].

The largest GB system is 29.5 × 25.5 × 3.4 nm and contains 297813 atoms while the smallest system is 11.3 × 6.5 × 3.4 nm with 28902 atoms. All systems tested at the same number of graphite planes and thus the same length in z. For a given value of α the number of atoms and subsequent GB energy changed based on the configuration output from the Olmsted procedure, but the total system volume V remained constant. The range of GB energies presented here is approximately 3.8 to 6.0 J/m^2 which are an order of magnitude greater than GBs in metallic systems such as copper and nickel [96, 16, 76, 78, 105, 106, 87]. However, when compared to edge-plane surface energies in graphite and graphene grain boundaries, the results presented here are well within the published range [54, 4]. Figure 2.34 displays a range of grain boundary energies for graphene grain boundaries, which although are 2-D structures, still mimic the in-plane behavior of graphite grain boundaries in this study.

Figure 2.35 shows a rendering of one of the grain boundaries used in this thesis. The grain boundary runs vertically as well as into and out of the page, with periodic boundary conditions present in all directions. The buckled regions at the GB are exacerbated by the projection of the atoms into a 2-D plane. Liu *et al.* also saw buckling in graphene grain boundaries on the order of 2-3 Å as a result of dislocations local to the GB [54]. A

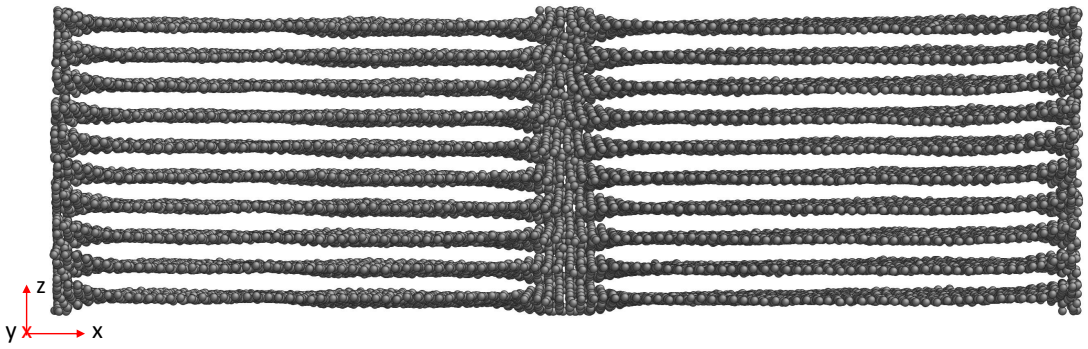

Figure 2.35: Atomistic rendering of the $\alpha = 8.26°$ grain boundary system. A grain boundary is present at the center of the image as well as the edge.

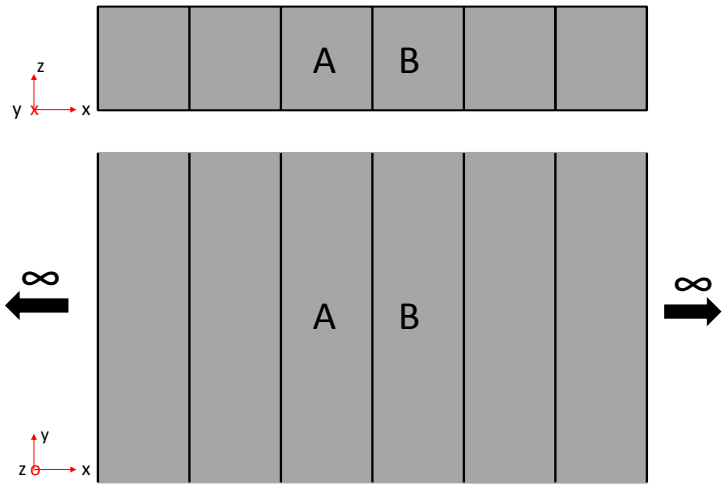

Figure 2.36: Schematic showing the relation between simulated system and the physical equivalent. Grains A and B are constructed in LAMMPS, but have infinite extent because of periodic boundary conditions.

closer investigation of the GB shows that the lattice disruption is highly localized and the structure returns to normal within one lattice constant of the GB in either direction.

The periodic boundary conditions used in here actually create an array of infinite grain boundaries, with grains of infinite extent in the the y direction, as well as the z direction for bulk GB diffusion studies. Figure 2.36 showcases the physicality of the system, as viewed by LAMMPS. The only grains that truly exist in the sense of atomic positions, velocities, etc, are those labeled 'A' and 'B' in the figure. The black lines represent the grain boundaries in two separation projections.

The data and procedure presented here could be used to simulate and study graphite

grain boundaries on their own, in the absence of lithium. As will be discussed later, a great deal of information can be gained from an investigation of structure alone. However, to probe the theories detailed at the beginning of this dissertation, supplemental parameters (notably additional interatomic potentials) must be addressed to facilitate the incorporation of Li into the proposed model.

Chapter 3

Lithium-Carbon Interatomic Potential Optimization

3.1 Introduction

Lithium-ion batteries (LIBs) are the most popular form of rechargeable batteries on the market today. They appear in various portable electronic devices, ranging from cell phones to advanced hybrid and electric vehicles [37]. Their charge density, portability, and cost all lead to the widespread use over previous battery technologies. LIBs consist of three main components, a positive electrode (cathode), a negative electrode (anode), and an electrolyte serving as a interface between the two electrodes. The flow of electrons from the cathode to the anode represents the charging process, while the opposite represents discharging. Although at the forefront of advancing battery technologies, high performance variability remains, sometimes leading to catastrophic failure in the form of fires or explosions as in the case of the Boeing 787 [104].

Graphite is a commonly used anode material for its lightweight, durability under cycling, and relatively low cost [71]. Consisting of stacked planes of carbon atoms, lithium-ions site in the empty space between these planes, known as galleries. The weak van der Waals forces holding the graphite planes together hardly resist lithium motion, thereby promoting rapid diffusion. On the contrary, each graphite plane consists of carbon atoms

arranged in a hexagonal lattice with covalent bonding. This arrangement causes lithium motion through the graphite lattice to be extreme energetically unfavorable, such that edge-plane or defect diffusion are the sole modes for lithium diffusion or intercalation.

Some researchers believed that graphene, which is a single layer of graphite, would supersede graphite as the common anode material in LIBs. It was believed that pristine graphene had a theoretical capacity six times that of graphite or Li_6C_6 [50]. Lee *et al.* hypothesized that researchers were using an incorrect reference state for Li when computing binding energies, leading to the stable Li_6C_6 state. Computing binding energies with bulk metallic lithium as the reference state led to no stable configurations for Li absorption and Lee noted that if the gaseous state was used, there were some stable configurations like those noted in other computational studies [50]. Instead, it is believed that favorable configurations of graphene come from defects, rather than pristine graphene [30].

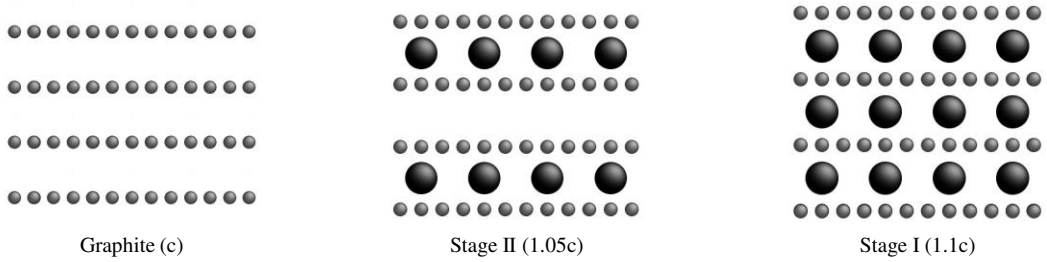

Figure 3.1: Lithium stacking sequences in graphite. Pure graphite, having a basal plane lattice constant c, Stage II $Li_{0.5}C_6$ with 5% expansion, and Stage I LiC_6 exhibiting a 10% expansion over pure graphite.

As lithium fills graphite crystals, it does so in well-defined stages [71]. Rather than lithium-ions intercalating into all empty galleries simultaneously, it will preferentially accumulate in a gallery before filling subsequent empty galleries. This leads to the behavior seen in Figure 3.1, where the staging number refers to the number of empty galleries between filled ones. A crystal with n empty layers between filled ones has staging in the form of $n + 1$ such that LiC_6 forms a Stage I compound (no empty layers). To further clarify this behavior, Stage I LiC_6 and Stage II $Li_{0.5}C_6$ contain the same number of lithium atoms in filled galleries but the total number of lithium atoms in the $x = 0.5$ is obviously half that of $x = 1$ for Li_xC_6. This staging notation continues until no lithium is

present ($n = \infty$), which is obviously bulk graphite. Also associated with this staging during charging is an expansion of the graphite lattice in the basal direction [24]. As lithium concentration grows, the repulsive interaction between lithium atoms in different galleries increases as well, overcoming the attractive van der Waals C-C forces leading to crystallographic expansion. Experiments show that this expansion is approximately 5% at $Li_{0.5}C_6$ and 10% at LiC_6 [24]. This expansion and subsequent compression cycling under repeated charge/discharge cycles are certainly reason to believe that local and global stress fields manifest during normal battery operation. Over time, fatigue and further anode degradation may come into play leading to anomalous battery behavior, warranting further studies in such transient processes.

The aforementioned modes of lithium intercalation and subsequent diffusion lead to varying rates of lithium motion in graphite anodes. Experiments and computational studies report several orders of magnitude difference, ranging from 10^{-6} to 10^{-11} cm^2/s [70, 108, 88]. Concentration effects and diffusional anisotropy are leading explanations as to the large assortment of diffusion rates, but are certainly not the only possible explanations. Previous computational studies have focused on first-principles to produce important quantities such as minimum energy configurations and binding energies along with extrapolated diffusivities, but only allow for limited trajectory data. This speaks volumes to the importance of classical simulations for investigating longer range behaviors in both time and length scales which can be used in conjunction with existing studies to better explain observed performance.

One unique aspect of LIBs that had not yet been investigated is the role of grain boundaries on diffusion rates of lithium in graphite. As mentioned earlier, the goal of this thesis is to show that grain boundary geometry and structure can explain the diffusional differences and intended to simulate intercalation into and transport through, graphite grain boundaries using Molecular Dynamics (MD).

In the remaining sections of this Chapter, existing interatomic potentials will be introduced, along with their strengths and weaknesses. Further, a modification procedure will be detailed to the existing potentials that allows for various studies of the Li-C sys-

tem including single atom diffusivity, bulk single-crystal diffusivity, and grain boundary intercalation and diffusion. Finally, any shortcomings in the modified potentials will be discussed as well as possible remedies and advancements for future work.

3.2 Classical Potentials for the Li-C System

While there have been countless experimental and computational studies on the Lithium-Carbon system, there is a lack of available interatomic potentials for classical simulations with Lithium-Lithium and Lithium-Carbon interactions. Alternatively, Carbon-Carbon interactions are well-described by such potentials as the Adaptive Intermolecular Reactive Empirical Bond Order (AIREBO) potential developed by Stuart or the Tersoff Potential [85, 90, 92, 91]. These potentials are highly accurate for graphite and closely reproduce many experimental aspects of the system. Similar potentials were desired for Li-C and Li-Li and thus various options were explored to accomplish this.

Existing potentials could correctly model bulk lithium-metal behavior such as ReaxFF developed by van Duin *et al.*, but they were not well suited for applications to LIB studies [36]. Based on the goals of this study, a fully (QM) or partial (QM-CL) first-principles approach would not be practical. Within the MD realm, a charge transfer model would provide high levels of accuracy but are highly computationally expensive and again not practical for the duration of simulations needed here. Therefore, a simpler approach was desired for modeling the interatomic interactions.

An existing set of empirical pair potentials were found that were developed for use in finding stable assemblages in Li-C systems by Particle Swarm Optimization and Differential Evolution [21]. Additionally, the authors set out to study advanced anode configurations for LIBs, specifically carbon nanotubes [20]. These potentials were developed by Chakraborti *et al.* using a least-squares fitting procedure with DFT of the C-Li+ dimer [21]. Equations 3.1 and 3.2 represent the pair potential energy as a function of separation distance, r, for Li-C and Li-Li, respectively. Full details of the associated constants are presented in Ref. [21] and [20]. The Li-C potential has an attractive and repulsive regime while the Li-Li potential is a strictly repulsive potential and behaves similar to a Coulombic interaction;

it therefore cannot model bulk metallic lithium. Notably these are not charge transfer models and again are restricted to pair interactions.

The original authors provided system energies for several small Li-C clusters via MD which were verified by performing energy minimizations using LAMMPS with a Tersoff Carbon-Carbon Potential [73, 90].

$$U_{LiC} = \frac{A_1}{r_{ij}^{\lambda_1}} exp\left(-\alpha_1 r_{ij}^2\right) - \frac{A_2}{r_{ij}^{\lambda_2}} exp\left(-\alpha_2 r_{ij}^2\right) \tag{3.1}$$

$$U_{LiLi} = \frac{a'}{r_{ij}} exp\left(-b' r_{ij}\right) \tag{3.2}$$

3.2.1 Single-ion Diffusivity

To compare to both experiments and simulations, mass transport characteristics of lithium needed to be established for this system of interatomic potentials. In doing so, single-ion diffusivity tests in bulk graphite were performed to compare to existing QM-CL data. Ohba *et al.* performed QM-CL simulations of single lithium-ions in bulk graphite to probe the dependence of diffusivity rates on interlayer spacing [67]. The authors provided thorough mean-squared displacement (MSD) data, which is related to particle diffusivity and shown in Equation 3.3, as a means of comparison.

$$MSD \equiv \left\langle \left(x\left(t\right) - x_0\right)^2 \right\rangle \tag{3.3}$$

This work used AIREBO for C-C interactions and the two potentials developed by Chakraborti *et al.* to simulate single particle diffusion. A single lithium atom was inserted into a graphite crystal containing 15,680 atoms and run dynamically using a microcanonical (NVE) ensemble at $T = 423$ K for 250 ps. Lithium's light weight necessitated the use of a $t = 0.0001$ ps timestep to fully capture atomic trajectories which is 1/10 of the typical timestep used for metallic systems. MSD data was calculated in 12 ps lengths, with a new calculation window beginning every 0.1 ps to collect an increased number of data sets while maintaining statistical independence. The inset of Figure 3.2 shows MSD data from

Ohba and this work, over 3 ps. Based on differences in C-C potentials used, the interlayer spacing of this work (6.8391 Å) corresponds to an approximately 2.5% expansion of the lattice in Ohba's work, which is the case presented in Figure 3.2. In both works, the single-ion exhibited largely ballistic motion rather than site hops, which in graphite equates to approximately 5.85 $Å^2$. The close correlation between the data sets confirmed the accuracy of the Li-C potential for diffusion studies and hence further verification of the Li-Li system was needed before continuing.

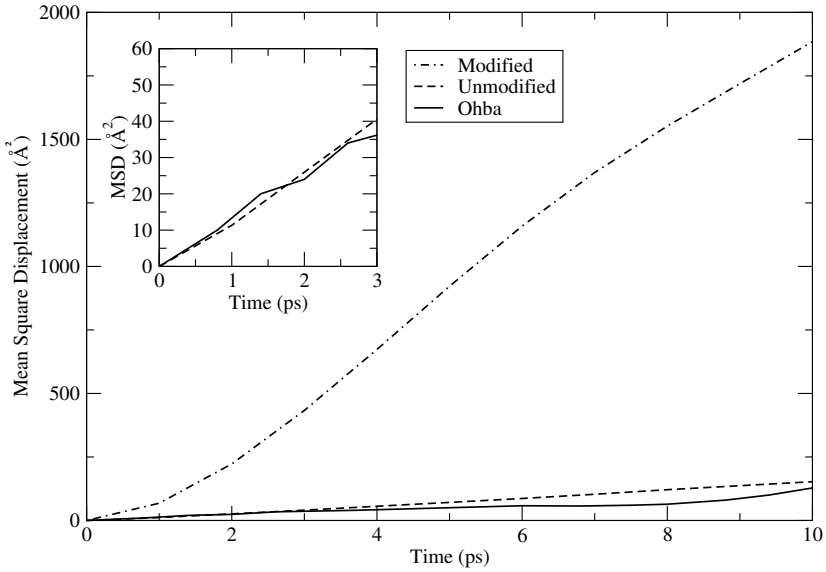

Figure 3.2: Mean squared displacement for single Li atom simulations for the potentials developed here and the original authors, compared to QM-CL simulations by Ohba *et al.* [67]. Inset focuses on early time of trends shown in main panel.

Many groups have shown the strong dependence of diffusivity on Li concentration and the next goal was to verify this dependence in bulk graphite via MD [70, 108, 88]. To test the Li-Li potential, several systems were created with varying Li concentrations ranging from $x = 0.25$ to $x = 1.0$ in Li_xC_6. Like previously mentioned, expansion of the lattice in the basal direction should be noted for all Li concentrations, with a maximum expansion of 10% at LiC_6.

Each system tested was equilibrated using an isobaric-isothermal (NPT) ensemble at $T = 300$ K and zero pressure to allow for relaxation in the basal direction such that each diffusion study takes place at the equilibrium lattice constant for that loading. Upon

relaxing the compounds, average interlayer spacing was computed to verify the accuracy of the Li-Li potential at various loadings. For all concentrations of Li the system showed compression in the basal direction, which is not seen experimentally, peaking at 17% for $Li_{0.5}C_6$. Figure 3.3 compares Chakraborti's potentials with experiments by Dahn and first principles by Persson *et al.*, showing compression across all concentrations versus expansion everywhere for the contrary [24, 70]. This compression corresponds to an overpowering Li-C attraction across several planes of C atoms, resisted only by the very weak vdW forces. The cutoff distance of 10.2 Å (chosen to match cutoff radius for AIREBO potential by Stuart) allows for lithium atoms in a gallery to pair with carbon atoms in the three nearest planes, across an empty gallery in Stage II cases which occurs when $x \leq 0.50$. Lithium bonds with the six nearest-neighbor carbon atoms in the stable configuration thus the high levels of attraction as the Li concentration increases.

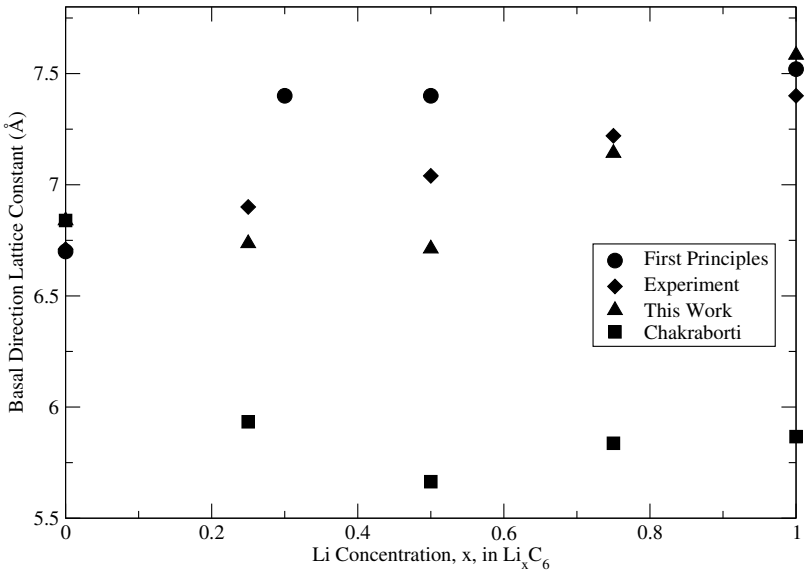

Figure 3.3: Basal direction lattice spacing (c) as a function of Lithium concentration at $T = 300$ K from Chakraborti *et al.*, this work, experiment by Dahn, and first-principles by Persson *et al.* [21, 24, 70]. The $x = 0$ values corresponds to bulk graphite for each work.

The goal of this work was to study grain boundary intercalation and subsequent diffusion, thus it was decided that although there was good agreement with single Li data, the potentials needed modification to fit the needs of this dissertation. These modifications understandably alter single Li results significantly but should provide valuable insight

into the behavior of mass transport in a covalently bonded grain boundary; something not previously studied with application to energy storage materials.

3.3 Potential Modification Procedure

Like mentioned above, there was a lot of excitement soon after the discovery of graphene with thoughts that it could have a higher theoretical storage capacity than graphite. However, it has since been proven that pristine graphene falls well short of the charge capacity of graphite. When evaluating this hypothesis, Lee and Persson published extensive absorption energy data for lithium concentrations on graphene ranging from pure graphite to Li_6C_6 as computed by first-principles. It was believed that this data would provide an appropriate baseline for potential modifications as it accentuates both the Li-C attraction and the Li-Li repulsion with Li atoms straddling either side of the graphene layer. However, graphene is a two-dimensional material and therefore this study alone will not probe any change to the interlayer spacing with increases in Li concentration. Therefore, experimental expansion data is also considered to provide additional parameters for modifying the existing empirical potentials.

Using conjugate-gradient energy minimizations, Lee's calculations were repeated for two configurations of Li on graphene, $Li_{1.5}C_6$ and Li_6C_6. The total number of atoms in the system were 810 and 1296 across 108 fundamental units (FU), which is equivalent to those constructed by previous work. Although a range of energies were reported at each loading, values of 0.8 and 3.1 eV as calculated by Lee *et al.* using VASP were used. Equation 3.4 represents the absorption energy calculation performed, where $E(x)$ is the computed absorption energy per FU of Li_xC_6, $E(0)$ is the energy of pure graphene, x is Li concentration, and E_{Li} is the energy of a bulk metallic Li atom, taken as -1.67 eV/FU [48].

$$E_a(x) = E(x) - E(0) - xE_{Li} \tag{3.4}$$

From the onset, this modification was not intended to be a full potential development,

Table 3.1: Possible scaling factor combinations based on a least-squares fit to absorption energy data from Lee and Persson and energy minimizations performed by the authors [50].

δ_1	δ_2	$E_a\,(1.5)$	$E_a\,(6)$	Error
0.1014	0.0628	0.3397	3.2047	0.2229
0.0885	0.050	0.6314	3.8105	0.5333
0.1142	0.0885	0.1036	3.3768	0.5616
0.1014	0.0500	0.2840	2.4245	0.7225
0.1142	0.0757	0.047	2.5989	0.8169
0.1014	0.0757	0.3954	3.9832	0.9438

thus a simple scaling approach of the existing potentials was taken, as noted in Equations 3.5 & 3.6.

$$U^*_{LiC} = \delta_1 U_{LiC} \tag{3.5}$$

$$U^*_{LiLi} = \delta_2 U_{LiLi} \tag{3.6}$$

Scaling factors ranging from 0 to 1 were applied to both the Li-C and Li-Li potential and implemented in LAMMPS prior to performing energy minimizations. The absorption energy for the configuration was recorded along with the error calculated by a least-squares fit to Lee's data for each scaling combination. Scaling factors were only considered acceptable if they produced positive absorption energies at both the low and high Li concentrations, consistent with previous studies. This produced numerous combinations of acceptable scales, thus further refinement was necessary. Deeming an error less than 1.0 as a suitable starting point, several combinations of scaling factors were returned as viable options based on the initial criteria, as seen in Table 3.1.

Upon investigation of Table 3.1 it is obvious that scaling factors of $\delta_1 = 0.1014$ and $\delta_2 = 0.0628$ lead to the greatest correlation to Lee and Persson's findings. With the first of two modification criteria satisfied, dynamic simulations were performed on a bulk LiC_6

system to quantify changes in interlayer spacing. Like the original potentials, the new selections resulted in compression of the graphite lattice, which again is non-physical.

Aside from contradicting experiment, compression of the graphite lattice has been shown to greatly stifle intraplanar diffusion of lithium [67]. With the driving force of potential redevelopment being diffusion studies, this suppression would severely increase simulation times and perhaps alter the dynamics of the system from a ballistic nature to more site hops or no motion at all for lower Li concentrations.

The obvious issue with both this choice and the original potentials is that the relative magnitude of Li-C and Li-Li potentials are quite skewed. The overwhelming nature of the Li-C attraction fails to allow the Li-Li strictly repulsive potential to become effective and increase the layer spacing of the system. When the potentials are scaled back such as those selected from the authors' optimization, there is less system-wide compression however again the Li-Li repulsions are not strong enough to overcome attractive forces.

At this point, it is understood that the best scaling parameters for the desired application must deviate from the published *ab initio* data to correctly capture crystallographic expansion. Like previously stated, experimental data shows that fully-liathiated graphite expands 10% in the basal direction. Provided that this effect could be captured while maintaining positive absorption energies, albeit it with greater errors than before, the scaling factors would be considered acceptable.

Various scaling factors were chosen and applied to a LiC_6 system running dynamically with an isobaric-isothermal ensemble at $T = 300$ K. The basal plane lattice constant was measured and compared to the pure graphite lattice constant to verify expansion. One such combination that resulted in an approximate 10% expansion at LiC_6 was $\delta_1 = 0.0885$ and $\delta_2 = 0.90$. For these factors, the absorption energies were 4.33 and 41.0 eV, respectively. While the $Li_{1.5}C_6$ energies remained reasonable, the Li_6C_6 grew quite rapidly leading to the large deviations from published data. However, it was decided that these factors accomplished the initial goals of this modification with adequate precision and were selected as the final values. Figure 3.4 shows Chakraborti's original potentials alongside the scaled potentials developed in this work.

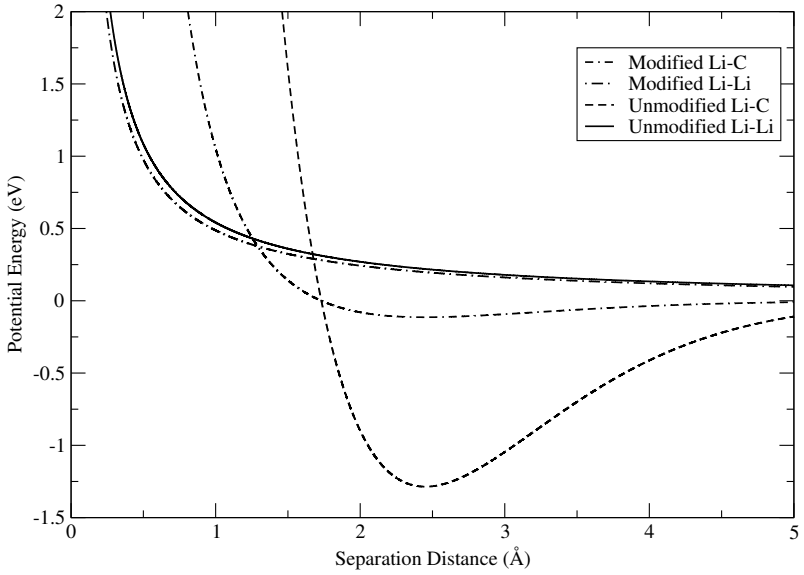

Figure 3.4: Potential energy as a function of particle separation distance for both Lithium-Carbon and Lithium-Lithium potentials. Shown are the unmodified potentials from Chakraborti *et al.* as well as the two potentials modified here. Although not shown, the cutoff radius for each potential is 10.2 $\mathring{A}$.

3.4 Transport Calculations

With new scaling factors established, focus moved forward with studies of Li transport in bulk graphite. These simulations would serve as baseline analyses for the potentials to determine relative diffusion rates in defects such as grain boundaries. Speaking in relative magnitudes allows differences to be established between GBs and lends itself toward the development of a GB diffusion model for this covalent system. For bulk diffusion, four systems were constructed with Li concentrations of $x = 0.25,\ 0.5,\ 0.75$ and 1.0. The lower two concentrations were Stage II configurations, while the latter were both Stage I. The $x = 0.50$ and $x = 1.0$ cases have the same number of Li atoms in filled galleries, however the former case has half the total number of Li atoms in the system. The motivation behind these concentrations was to span the entire range of possible loadings but also address concerns with the competing effects of the potentials. The cases with identical in-plane loading will have the same in-plane Li-Li repulsion, but the out-of-plane repulsion will be much different for the $x = 0.5$ case as the nearest neighbor in that direction is c Å away as opposed to $c/2$.

Each system was equilibrated under a isobaric-isothermal ensemble (NPT) for 50ps at zero pressure and $T = 300$ K to allow for relaxation in the basal direction. For diffusion simulations, C atoms of the relaxed system were run under a canonical ensemble (NVT) also at $T = 300$ K while Li atoms used a microcanonical ensemble (NVE). The same four loadings were simulated using the existing potentials as well as those modified in this work. This will expand on single-ion studies such that a complete diffusion picture is formed in terms of changes caused by these modifications.

While dynamics are certainly important with regards to potential optimizations, equilibrium structures should also be considered. Planes in pure graphite exhibit an ABAB stacking sequence however this can change when lithium intercalates into a crystal [71]. For low concentrations of Li, below approximately $x = 0.25$, the Li-C attraction is not strong enough to overcome the C-C interlayer interactions and hence Li atoms sit slightly horizontally offset from the hexagonal carbon ring in the plane above or below its current position. However, when Li concentration exceeds $x \sim 0.25$, the Li-C attraction overcomes the weak van der Waals forces such that the graphite planes undergo a shift and the entire crystal assumes an AA stacking sequence [34]. This shift ensures that Li atoms are centered between two concentric hexagonal rings in the adjacent layers. For Stage I LiC_6 and Stage II $Li_{0.5}C_6$, this leads to a $\sqrt{3} \times \sqrt{3}$ ordering in a loaded gallery as seen in the left panel of Figure 3.6. This ordering sequence dictates the nearest neighbor distance for in-plane Li atoms, which is outlined in Figure 3.5. The nomenclature for the ordering defines the edge length of the red triangle in the Figure, with each side being $a\sqrt{3}$ Å long where a is the in-plane graphene lattice constant. It became evident rather quickly under equilibration that the existing potentials do not maintain the prescribed in-plane ordering for Li but rather a labyrinthine arrangement shown in the right panel of Figure 3.6. In the Figure, Li atoms appear black, with larger radii than the gray carbon atoms that compose the graphite lattice. The modified potentials on the other hand have well-defined Li sites consistent with results by Persson *et al.* [70].

Dynamic simulations of the modified and unmodified potentials uncovered vastly different transport behavior that warrant discussion. Like previously mentioned, the ratio of the

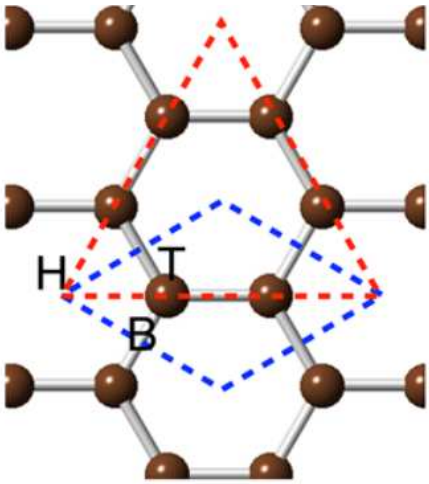

Figure 3.5: Graphic of the graphene unit cell (blue line) and the nearest neighbor Li ordering of a fully lithiated graphene plane (red line) [50].

two potentials was greatly skewed, such that the Li-C attraction did not allow for sufficient crystallographic expansion. For example, with the exception of the $Li_{0.25}C_6$ case, soon after dynamics are instituted, the Li dissociate from their expected sites and form amorphous chains. This behavior may in fact be directly coupled with the high levels of basal direction compression noted above, as Ohba noted such compression has great negative effect on Li transport [67]. Very little, if any, transport occurs over the simulated regime, such that it is not possible to discuss hop frequency or any sort of diffusive characteristics.

Figure 3.7 shows transport behavior for the modified potentials at three of the four loadings mentioned previously. Although hop frequency varies greatly across each case (as expected), hops are still attainable for some of the simulation durations studied here. The $Li_{0.25}C_6$ case (not pictured) behaves quite similarly to the single-ion case such that atomic transport is highly ballistic rather than site to site hops. The rate at which the MSD increases for this case is equivalent to the single-ion behavior from the unmodified potentials. This shows that although the magnitude of the Li-C attraction has been greatly reduced, the Li-Li repulsion is enough to suppress the extremely rapid transport seen in the single-ion case of the new potentials. The transition from ballistic motion to hopping motion occurred between $x = 0.25$ and $x = 0.50$, with all simulations above the latter exhibiting hop dynamics. This is expected, especially at $x = 0.50$ because of the in-plane

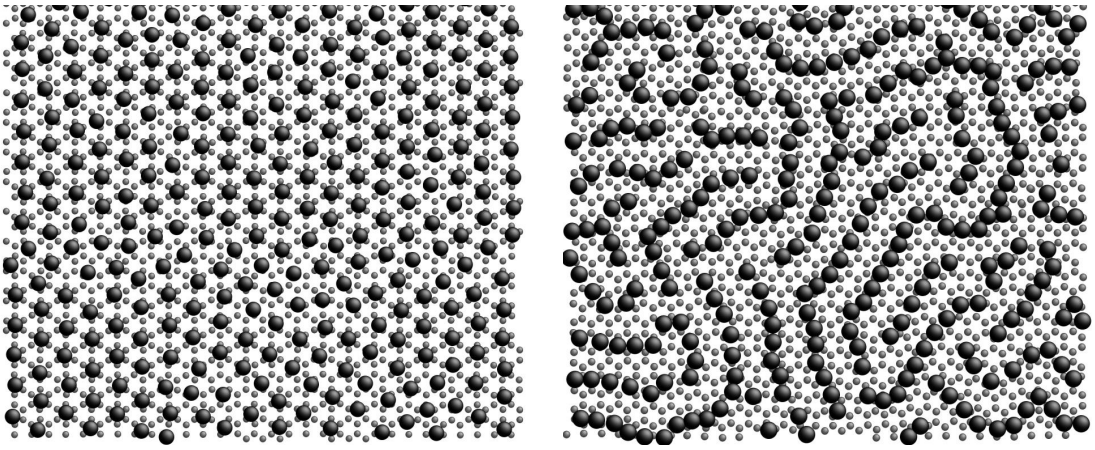

Figure 3.6: Li in-plane ordering during an MD simulation of Stage I LiC_6 for this work (left) as well as the original potentials (right). Li atoms assume a $\sqrt{3} \times \sqrt{3}$ ordering on the left like noted by Persson, while Li on the right site in a labyrinthine manner [71].

loading equal to that of LiC_6. Our simulations show that when hops do occur, they are occurring via the NN hop across a C-C bond to the adjacent vacant site, especially in the highest loading case. For intermediate loadings the image isn't as clear cut as the AA stacking sequence is not as distinct as with LiC_6.

For the present study, it is worth considering relative magnitudes of transport with the potentials optimized here. While the higher loadings exhibit very slow, if any, transport, diffusion rates can at least be estimated given the data calculated. Like mentioned above, diffusion rates of Li in graphite have varied by large orders of magnitude, from 10^{-06} to 10^{-12} cm^2/s. Here, we find that diffusion rates as a function of concentration range from 10^{-04} to 10^{-08} cm^2/s. While the overall magnitudes are more rapid than previous results, the variability is consistent with both experiment and simulation. The modified potentials clearly perform worst at lower loadings as the Li-C potential has been reduced by such a great amount. For higher loadings, the Li-Li repulsion can suppress rapid transport, as reported by others [70]. For the LiC_6 case, there were minimal Li site hops after 1.2 ns worth of simulation, with only a handful of atoms migrating from one site to another. This is to be expected, as Li atoms in this configuration need to pass in very close proximity to one another when diffusion, as seen in Figure 3.8. With no stable Li vacancies in LiC_6, it

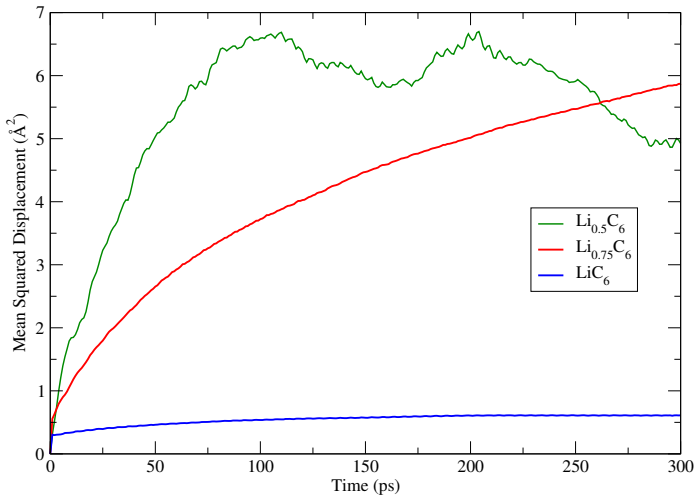

Figure 3.7: Mean-squared displacement plot of various Li concentrations with the potentials developed here.

is worth asking the question, what will the addition of a minimal number of Li vacancies do to in-plane diffusion?

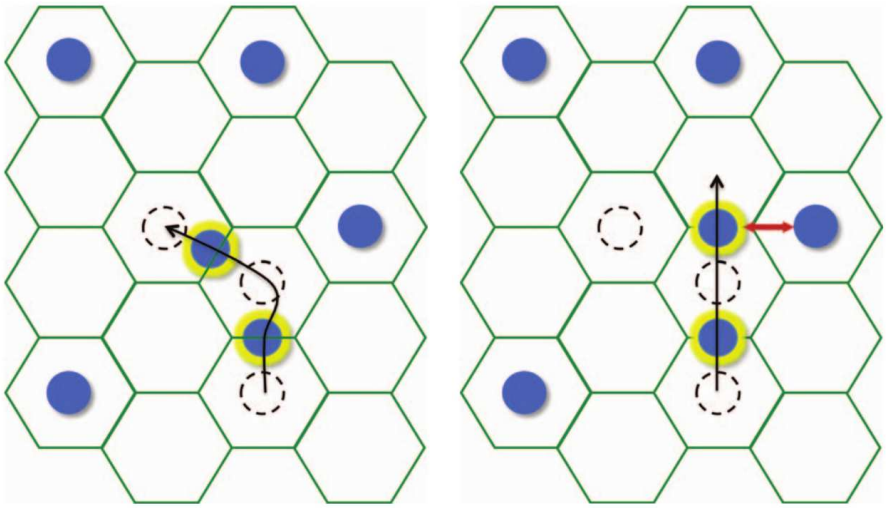

Figure 3.8: In-plane Li transport pathways from one site to another. The pathway as right is highly energetically unfavorable due to the proximity of one Li to its NN [70].

The $Li_{0.99}C_6$ case was investigated using the same MD techniques detailed above using the potentials developed here. The decrease in Li loading by 1.0% from the fully lithiated case corresponds to the addition of 3 Li vacancies per gallery for the system size used in these trials. Although it varies only slightly from LiC_6 in terms of loading, there is a

rather drastic change in transport behavior. While the fully loaded case showed very little diffusion, the addition of vacancies allows for more rapid and widespread transport system-wide. In fact, this slight change caused the $x = 0.99$ case to behave very similarly to the $x = 0.75$ loading and actually exhibited more rapid transport as seen in Figure 3.9. The reason behind the greater transport results from the stacking sequence change in graphite, which occurs at higher loadings for the potentials developed here than expected. At $Li_{0.75}C_6$, the graphene planes are no longer ABAB stacked, but are still slightly misaligned, thus resulting in convoluted vacancy sites and frustrated crystallographic behavior. For $Li_{0.99}C_6$, the crystal follows AA stacking, providing well defined Li and vacancy sites, abetting transport. This test of added vacancies demonstrates how energetically unfavorable lattice hops are for LiC_6, when atoms must pass in close proximity to other Li.

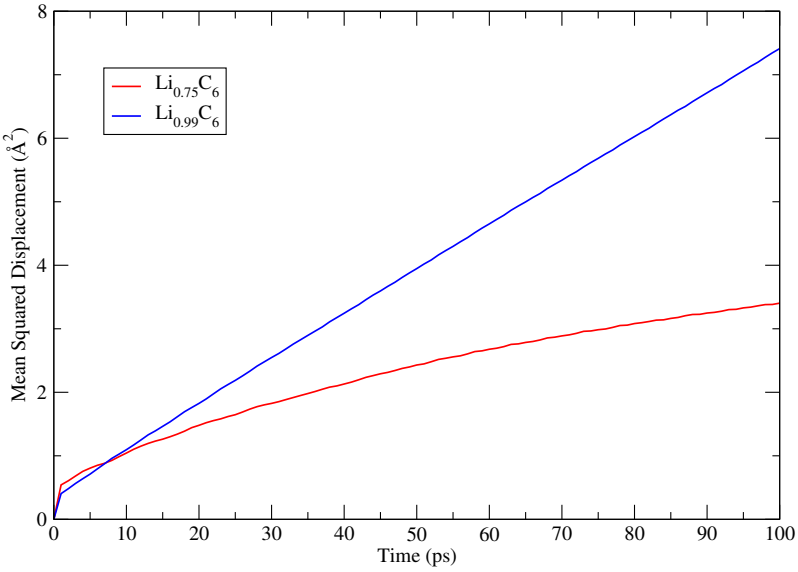

Figure 3.9: Single crystal mean squared displacement for $Li_{0.75}C_6$ and $Li_{0.99}C_6$ as a function of time.

Beyond bulk diffusion, the authors observed intercalation into graphite grain boundaries, which can be found in Ref. [81]. Although the new potentials meet the previously set goals of crystallographic expansion at LiC_6 and positive absorption energies, they do not fully capture the true structural behavior of the lithium-carbon system. Figure 3.3 shows basal direction lattice constants as a function of lithium concentrations from various sources. Like mentioned previously, experiments show expansion across the spectrum

of x concentrations, which is captured by Persson's first-principles studies of this system [70]. Although the modified potentials developed here shows expansion in the higher Li concentrations, there is still slight contraction of the lattice in loadings, specifically Stage II loadings with $x \leq 0.5$. While the potentials optimized in this Chpater show some basal direction compression, they are a significant improvement on the original potentials where there is compression across the concentration spectrum, peaking at 17% at $Li_{0.5}C_6$. This overcompensation of the Li-C attraction is evident in the need to scale down the potential by nearly 100% such that it provided reasonable physicality when compared to experiment. When discussing in-plane Li-Li equilibrium positions, the new potentials match existing data exactly, with a NN separation distance of 4.3 Å for fully liathiated galleries [72].

To further investigate the crystallographic behavior of the modified potentials, simulations testing the stress response of the crystal were performed. Here, an LiC_6 crystal was built and equilibrated at the equilibrium lattice constant for this work and then an external compressive pressure, ranging from $0 - 25$ GPa, was applied at constant temperature ($T = 300$ K). Relative lattice constants were calculated for both in-plane and out-of-plane behavior and compared to first-principles results by Kganyago *et al.* [47]. Figure 3.10 shows the results of the simulations, with the left panel displaying the interlayer lattice constant ratio c/c_0. and the right panel showing the in-plane constant fraction, a/a_0. While the calculated ratios differed from published work, the in-plane lattice showed very good agreement, with a error of only 0.22% at $P = 20$ GPa. The interplanar constants varied by approximately $5.5 - 8.5\%$ but maintained trends with first-principles. It's worth noting that the Lennard-Jones term in the AIREBO potential used here does exhibit shortcomings at high pressures, notably by overestimating the stiffness of graphite at small separations [65]. However, the data presented shows that the c lattice constant is actually softer for LiC_6 than reported. The likely cause is the reduced Li-Li potential, which controls the majority of the out-of-plane behavior. Additionally, the Li-C bonds screen the C-C vdW interactions, which is why there is a stacking shift upon intercalation, and therefore negate the issues seen in pure graphite with AIREBO [70]. In scaling back the repulsion, atoms in adjacent layers repel with less force than they would with the original potentials and

hence allow for greater compression. The in-plane $\sqrt{3} \times \sqrt{3}$ ordering is unaffected by the compression but like noted by others, diffusion has likely been suppressed completely [67]. Graphite's strong covalent bonds are responsible for the great in-plane stiffness and thus are largely unaffected by changes in pressure.

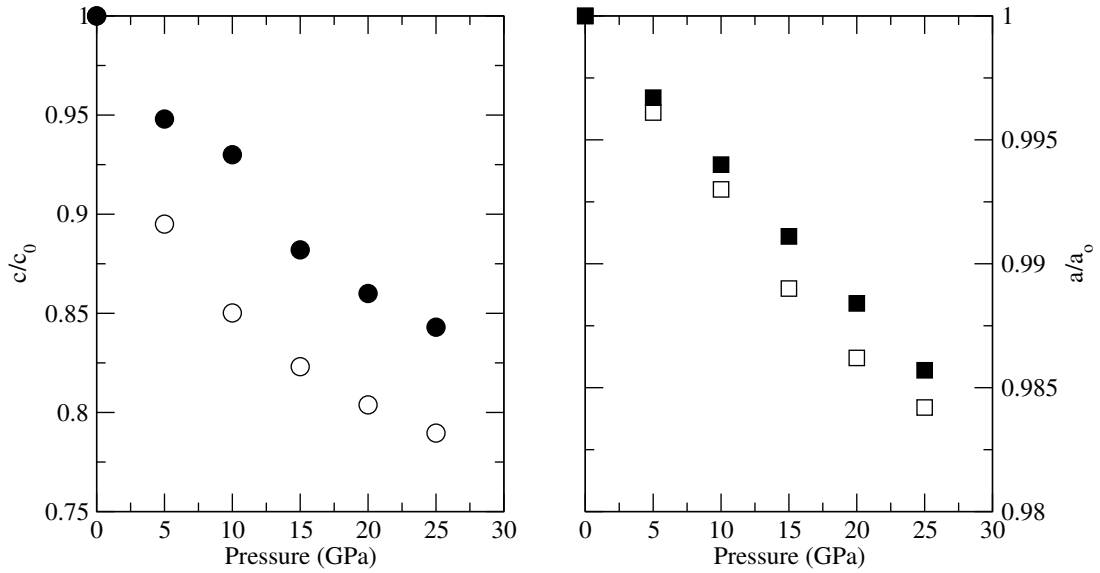

Figure 3.10: Comparison of LiC_6 relative lattice parameters for the modified potentials from this work (open symbols) and theory (psuedopotentials by Kganyago *et al.*, closed symbols) [47].

Since the new potentials still diverge slightly from experiment in regards to crystallographic behavior, the effect on diffusion was probed in the following manner. The basal direction lattice constant for these potentials was compared against experiment at each loading simulated above. The greatest error occurred for $Li_{0.5}C_6$ where this work underestimated expansion by 6.77%. Thus, a subsequent simulation was launched at this loading, however the crystal was forced to assume the correct expansion of 4.1% over the equilibrium lattice constant. Obviously this forces the crystal into a state of tension but the increased gallery size should abet diffusion or at the very least, have no negative effect. However, initial simulations show that the expansion of the lattice to the experimental value actually suppressed diffusion. One possible explanation is that the greater interlayer spacing between Li atoms lessened the Li-Li repulsion, which may promote diffusion. Therefore, it appears that both expansion or compression away from the equilibrium lattice constant

for a given concentration, Li_xC_6 has a great effect on diffusion rates.

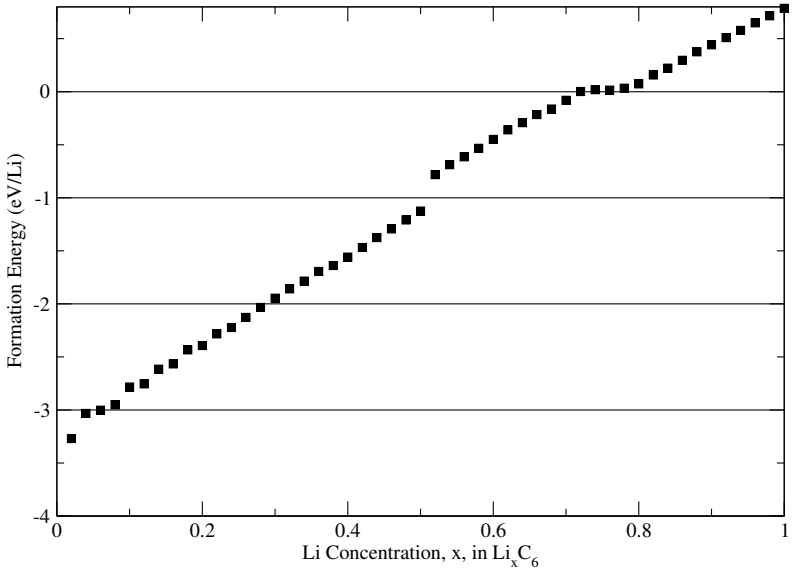

Figure 3.11: Formation energy as a function of lithium concentration in graphite. Calculated as difference in energy of the Li-C and pure graphite, per Lithium atom. The resulting transition from negative to positive formation energy around $x = 0.7$ corresponds well with simulation data showing gallery concentrations plateauing at $Li_{0.7}C_6$.

One interesting phenomenon that presented itself during intercalation simulations (to be presented later in this thesis) was that no gallery exhibited a lithium concentration greater than $x = 0.7$. Originally attributed to geometric factors at the grain boundary, an investigation into the formation energy led to a more explainable cause. Figure 3.11 shows formation energy as a function of Li concentration calculated by performing energy minimizations of bulk Li_xC_6. For the scaled potentials presented, the formation energy transitions from negative (stable) to positive (unstable) at approximately $x = 0.7$, corresponding well with the noted saturation point for each intercalation simulation. Additionally, a simulation probing edge-plane intercalation in graphite led to the same saturation point, further providing evidence that this is an artifact of the potentials and not a geometric constraint. There are several ways to calculate formation energy for the Li-C system based on the accepted reference state of Li. This work followed the model developed by Ganesh *et al.*, where formation energy is calculated as:

$$E_f(x) = \frac{E_{Total} - E_c N_c}{N_{Li}} \tag{3.7}$$

N_c and N_{Li} represent the total number of atoms of C and Li, respectively, while E_{Total} is the system energy at Li_xC_6 and E_c is the energy of one carbon atom, computed as -7.4786 eV here [34].

3.5 Further Recommendations

As shown, the lithium-carbon system is a rather complicated one with many factors contributing to the atomic interactions. One must ask the question if a simple pair potential is sufficient to fully capture these mechanisms. It is believed that a more complicated potential could fully address the shortcomings presented here however the goal of this work was to characterize grain boundary behavior relative to one other rather than address absolute lithium transport behavior in graphite. It is clear that gallery diffusion in graphite is the most rapid method of transport and this potential does not correctly capture the magnitude of this motion. However, the intent was to address what happens when gallery or edge-plane diffusion is suppressed by increased lithium levels in an anode. It is thought that any further refinement to the potentials or substitution with another potential would affect each study similarly since the actual graphite GB structure is well-defined by the well-regarded AIREBO potential. Instead, the actual transport rates may agree more closely with published data but the relative speed of transport through one GB relative to another would not change. A fast boundary would remain fast relative to other boundaries.

If further refinements were to be made to these potentials, it is useful to look at the structure of Li-Li and Li-C within a single crystal. Since atomic positions are known in MD simulations, these geometries are easily calculated via a radial distribution function or $g(r)$ plot. Knowing the equilibrium positions of nearest neighbors provides insight into the effects of each potential and provides hints at possible alterations. In this study, each potential has a cutoff of 10.2 Å, consistent with the C-C cutoff. Figure 3.12 shows the force-g(r) product for Li-C (left) and Li-Li (right) for LiC_6. It is easily seen that the Li-C

potential captures the nearest 2 graphene planes both above and below a Li atom, while the Li-Li potential extends much further. Extending the cutoff of Li-Li interactions or shortening that for Li-C could provide additional refinement without affecting the relative magnitude of the potentials.

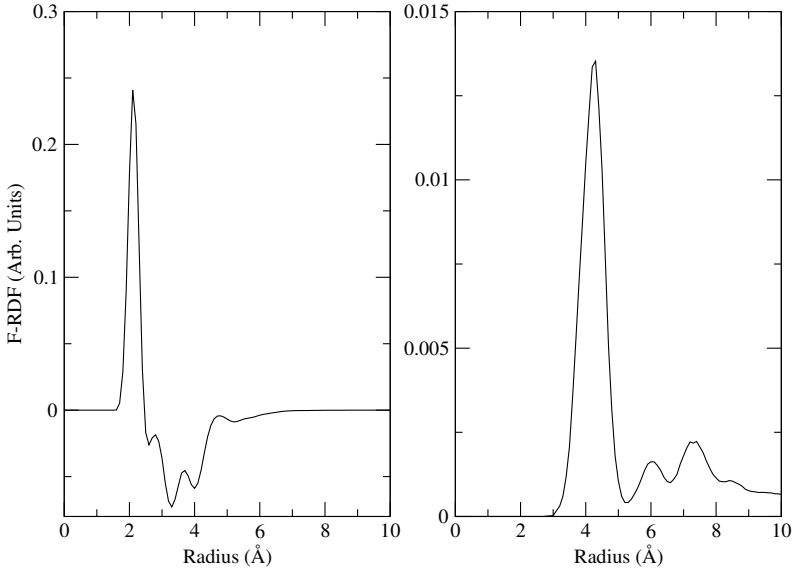

Figure 3.12: $F(r) \times g(r)$ for Lithium-Carbon (left) and Lithium-Lithium (right) interactions in Stage I LiC_6 using the modified potentials in this work. Li-C interactions decay much more rapidly than Li-Li interactions, exhibiting that separate cut-off distances for each potential may provide an area of further modification.

It's important to note that both the original and modified potentials do not support dynamic charge transfer and thus cannot handle the deintercalation process, which is essential to studying the entire charge/discharge cycle of an anode. If simulations were to be performed for the discharge process, artificial external force fields would need to be applied to drive Li atoms from graphite. This method would discredit any findings on rate and possibility even mechanisms and thus an entirely new approach is recommended for studies of that nature. Since such charge transfer is not modeled, subsequent chapters will refer to the Li particles in simulation work as atoms, rather than ions for clarification purposes.

The Li-C system is of great interest because of its importance in the LIB market. Although the cutting-edge of battery research has shifted to new geometries and charge carriers (to be discussed later), there is a large wealth of information still undiscovered for Lithium in graphite. Even with this relative importance, there is a shortage of interatomic

potentials that well describe this system in classical simulations. This work set out to simulate mass transport in single and polycrystalline graphite to address diffusional anisotropy and variability in anodes. However, existing empirical potentials exhibited shortcomings in modeling multi-atom transport. Existing Li-C and Li-Li potentials were optimized such that they couple well with both experiment and first-principles for the purposes of mass transport. While these new potentials have their own shortcomings, they are a still a vast improvement on existing potentials. Future refinement will no doubt increase the accuracy of these systems, but it may come in the form of multi-bodied potentials or charge transfer models.

Chapter 4

Grain Boundary Intercalation

4.1 Introduction

When LIBs charge, lithium-ions move from the cathode, through the electrolyte, and into the anode. Multiple studies have reinforced that, since diffusion through defect-free graphite layers is energetically unfavorable, intercalation must occur via edge-plane, grain boundary, or defect diffusion. Despite the highly ordered microstructure of HOPG, the atomic structure of electrolyte/HOPG interfaces cannot be precisely controlled during manufacturing of lithium-ion batteries. It is possible that a source of variation in graphite anodes is the composition of edge versus basal planes comprising the electrolyte/HOPG interface. Edge-plane intercalation is most rapid; however, when edge-plane pathways into graphite saturate, other paths into the bulk must abet continued anode intercalation. Prior studies show that surface diffusion of Li is very rapid $\left(D_{Li} = 5 \times 10^{-6}\ cm^2/s\right)$ at $T = 300$ K, but intercalation is negligible across defect-free basal planes such that transport into the anode at these interfaces occurs only at grain boundaries and defect sites on planar surfaces [57]. Other sources of variation in anode performance may then include the grain size distribution as well as the composition of grain boundaries present at basal planes in HOPG. Prior experiments noted the high diffusional anisotropy in graphite and showed that few-layer graphene with high defect concentration in the basal plane exhibit greater diffusion rates[108]. Other work illustrated a role of nanostructure and grain boundaries

in determining diffusivity in Nickel Oxide anodes [84]. Understanding Li grain boundary intercalation and diffusion in HOPG, including differences among boundaries, will provide insight into the observed range of diffusivity in graphitic anode materials.

4.2 Procedure

All simulations were performed using the LAMMPS Molecular Dynamics simulation package with constant temperature $T = 300$ K ensembles and a simulation time step of 0.1 fs throughout[73]. Particle interactions were modeled using the potentials outlined in Chapter 3 and the grain boundaries modeled are those discussed previously. Five symmetric twin, tilt grain boundary systems were modeled, with the axis of rotation parallel to the basal (c) direction and aligned along the z direction of all simulation volumes. For this study, GB misorientation angle, α, was defined as the angle through which crystals impinging on the GB must be rotated to achieve perfect alignment; α here ranged from 8.26° to 30.16°. Further preparation of GB systems for intercalation simulations followed the work of Olmsted, *et al.* [68]. Full details on potential optimization, grain boundary creation methodology, deposition modeling technique, and other numerical methods can be found elsewhere in this dissertation.

All GBs were modeled in yz planes and intersected a free surface in z. The top panel in Fig. 4.2 is representative of what was observed in all GBs modeled; however, the bonding structure in the buckled regions differed between GBs (see below). Similar to prior studies that explored single layer graphene, layers buckled near GBs [54]. The significant atomic overlap that appears to occur in the buckled region is an artifact of the orthographic projection used in the image along with the system thickness in y. As discussed below, well defined structure exists in the buckled region, albeit with characteristic differences from the ideal graphite crystal structure. A short distance to either side of the GB, the planar nature of graphite layers was restored. During charging of lithium ion batteries, intercalation occurs from an electrolyte material into graphite, typically through a reaction layer at the interface. Ion transport through the electrolyte and reaction layer are integral to battery performance. However, modeling the entire electrolyte/graphite interface requires

representation of the atomic structure of the reaction layer, a non-trivial activity with little experimental guidance. Most importantly, though, it is asserted that, at interfaces between electrolyte and basal planes of graphite, intercalation into GBs is a more significant source of variation than diffusion through the electrolyte or reaction layer. This is based on the premise that graphite exhibits greater long range order as well as anisotropy in structure. Given this, no electrolyte was modeled here and lithium atoms were deposited onto graphite surfaces from vacuum.

4.2.1 Deposition Procedure

To provide the same driving force for intercalation on each surface, a targeted deposition method was employed for all simulations. Initially, Li atoms were deposited randomly onto each surface over time and the total amount of Li deposited corresponded to an LiC_6 layer at the free surface. During this initialization, a small number of Li atoms intercalated into the crystal. Despite a random deposition process, Li atoms on the basal plane (i.e. away from where GBs intersected free surfaces) exhibited fairly ordered structures with Li atoms residing at the center of hexagonal C rings in the expected $\sqrt{3}\times\sqrt{3}$ ordering sequence. This initial surface deposition ensured that subsequent free surface diffusion of Li was largely suppressed due to the high loading of Li on each surface. Following initialization, a region was defined spanning in x from 1 nm before the central GB to 1 nm after it; the region spanned the length of the simulation box in y and extended to the simulation cell boundary in positive z; this region is schematically shown in the lower image of Fig. 4.1. Periodically throughout the simulation, the number of Li atoms contained in this region was computed. If the total number fell below the LiC_6 configuration for that region such that,

$$\frac{N_{Li}}{6N_C} < 1.0 \tag{4.1}$$

new Li atoms were deposited into random positions within the targeted deposition region with a very small velocity (0.01 Å/ps) in the negative z direction to ensure adsorption onto the surface. Thus, a relatively constant surface concentration of Li was maintained for all systems explored. It is possible that the original deposition to initialize the system

was the only time at which Li atoms were added to the system. Regardless of deposition, the thermodynamic ensemble remained the same in either case.

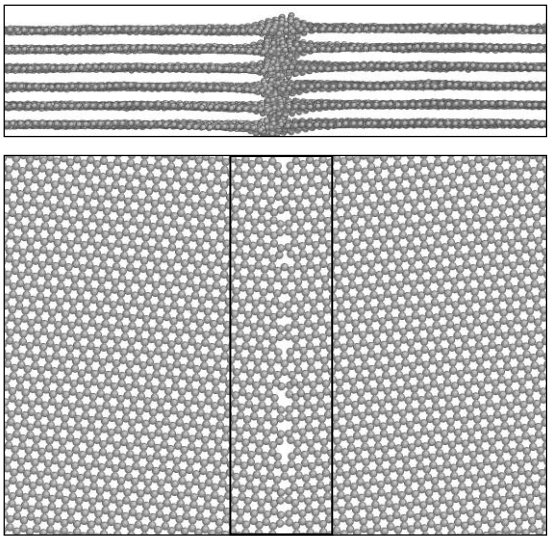

Figure 4.1: Simulation rendering for $\alpha = 8.26°$ boundary; in the top image, the simulation x/z directions are horizontal/vertical in the page and the y direction is normal to the page. In the bottom image, x/y directions are horizontal/vertical. In the first image, deposition occurs at the free surface at the top of the image. In the bottom image, targeted deposition is contained within the highlighted box.

4.3 Results

Figure 4.2 shows snapshots exhibiting a time progression during deposition onto the $\alpha = 8.26°$ GB graphite system, which exhibited one of the highest intercalation rates. Li atoms began intercalating into the boundary shortly after surface deposition commenced. This was similar for all systems modeled; however, significant differences quickly emerged in the rate of Li transport into different GBs. A common feature to intercalation, regardless of α, was that Li atoms initially intercalated primarily into the first gallery rather than diffusing deeper into the boundary. This behavior persisted until, for some systems, concentration in the first gallery grew sufficiently large to begin driving diffusion deeper into the crystal. This is shown qualitatively for the high rate boundary in Fig. 4.2 and is described as a staged intercalation process.

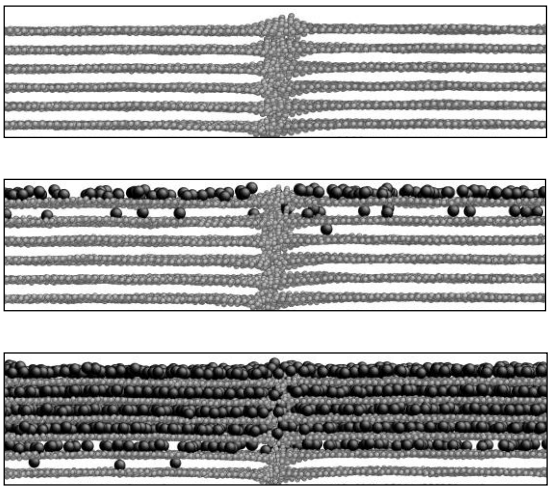

Figure 4.2: Simulation sequence for the $\alpha = 8.26°$ boundary; simulation x/z directions are horizontal/vertical in the page and the y direction is normal to the page. C/Li atoms are light/dark grey spheres; the free surface onto which deposition occurs is at the top of each image. (*top*) $t = 0$ ns; (*middle*) $t = 0.02$ ns; (*bottom*) $t = 1$ ns.

For all values of α studied, Fig. 4.3 shows the total number of Li atoms intercalated, normalized by the boundary length, as a function of time. Significant differences in intercalation rate are obvious. At early time, all systems had relatively empty internal graphite galleries such that the driving force for Li transport from the loaded free surface into the near surface region of the GB was highest and also consistent among different GBs. Slopes at early time for curves in the main panel of Fig. 4.3 are plotted in the inset of Fig. 4.3 and over two orders of magnitude exist between the highest and lowest observed intercalation rates. GB energy was computed for all boundaries modeled. It has been speculated that there exists a correlation between grain boundary energy and density of coincident sites in neighboring grains of metallic systems [68]. However, like Olmsted, *et al.*, we find no obvious correlation between grain boundary energy and misorientation angle, α for the covalent system studied here. Inset intercalation rate data are plotted versus GB energy and it can be seen that both relatively low and high energy boundaries show high rates with the lowest rate exhibited by a GB with intermediate energy. Thus, initial intercalation rate exhibits no obvious correlation with GB energy. However, for a given GB (i.e. value of α), data suggest that a dependence exists. For any given value of α, a range of boundary

energies can be obtained based on details of the GB creation methodology. The minimum energy boundary for each α (closed symbols on the inset curve) consistently exhibited lower intercalation rate than relatively higher energy versions of the same boundary.

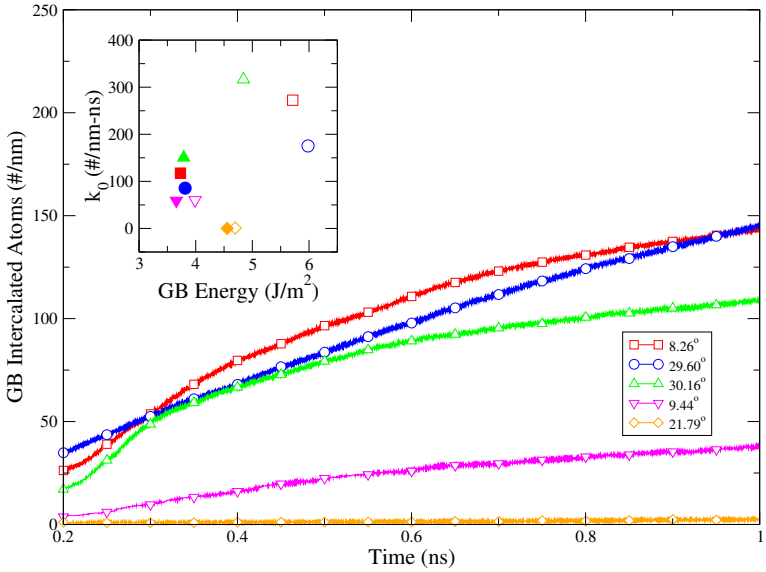

Figure 4.3: Amount of Li intercalated as a function of time for intermediate energy GBs; data are normalized by boundary length. (Inset) initial intercalation rate (k_0) computed between $t = 0.2$ ns and 0.3 ns versus GB energy. Open symbols correspond to data shown in the main panel; closed symbols were obtained using intercalation data from GB systems with the labeled α but lower GB energy.

Intercalation data for $\alpha = 30.16°$ and $\alpha = 8.26°$ show three distinct regimes in time with successively lower intercalation rate. This is a result of staged intercalation, where in-plane gallery diffusion of Li decreases with increasing concentration, forcing Li atoms to diffuse into deeper galleries via the GB [70]. Successively deeper galleries require more GB diffusion, such that overall intercalation rate decreased in a somewhat discontinuous manner as successive galleries filled. Intercalation into the largest unit cell GB ($\alpha = 29.60°$) was relatively fast; however, system size prevented the first gallery in that system from saturating during the time duration in Fig. 4.3 and only one kinetic regime is apparent in the data.

In Figure 4.4, four curves show the concentration of Li in the first four galleries below the surface for $\alpha = 8.26°$. Prior to $t \sim 0.3$ ns, intercalation beyond the first gallery was negligible. The first gallery composition at which intercalation slowed and intercalation

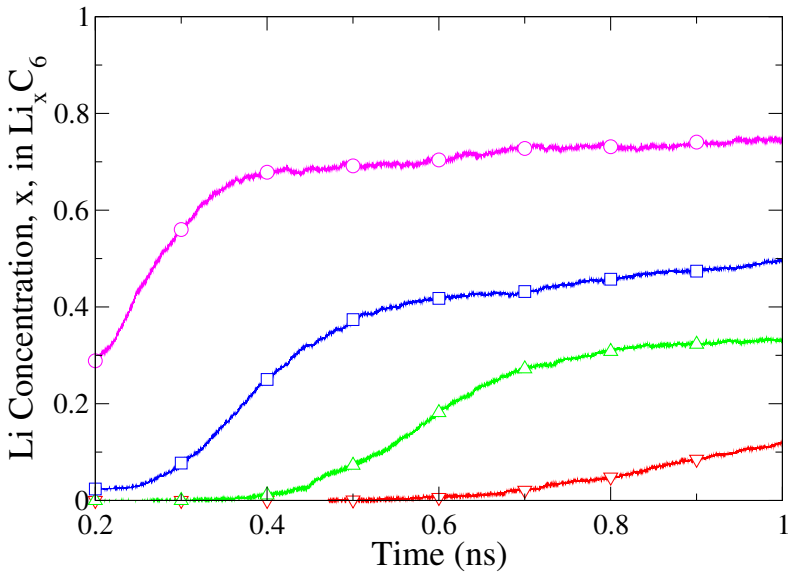

Figure 4.4: Concentration of Li in the first four galleries below the free surface for $\alpha = 8.26°$; curves for layers one to four order from top to bottom.

into the second gallery began was $x \sim 0.7$ for Li_xC_6. A similar transition was observed when intercalation into the third gallery began; however, the second gallery transition concentration was markedly lower than the first gallery transition concentration. This was reduced even more when intercalation into the third gallery slowed and intercalation into the fourth gallery began. This is in alignment with prior observations that intercalation into the first gallery occurs more readily than deeper galleries due to the first being adjacent to a free surface [50]. Since lattice expansion occurs local to where Li atoms absorb, evolving stress fields likely play a role in determining intercalation behavior into each gallery [82]. Additionally, the first gallery concentration at which second gallery diffusion ($x \sim 0.7$) begins is likely connected to the interatomic potentials more so than they physical nature of the system, as mentioned in Chapter 3.

4.3.1 Radial Distribution Analysis

As observed above, when comparing intercalation rate for different α GBs, there exists no obvious correlation with GB energy. Examining density local to GBs (and also to the free surface) revealed no correlation with rate either; the same was true for radial distribution analysis, a method for characterizing atomic order. The radial distribution functional

calculates the likelihood or probability of finding an atom a certain distance away from a central atom, averaged over a number of atoms, N. When referring to liquids, the probability tends towards 1, as there is no order in the system, especially when considering multiple snapshots in time [5]. The radial distribution function, sometimes referred to as $g(r)$ is computed by:

$$g(r) = \frac{\overline{n(r)}}{\rho V_{shell}} \tag{4.2}$$

where $\overline{n(r)}$ is the mean number of atoms in a given shell of volume $V_{shell} = 4\pi r^2 \delta r$. ρ is the mean atom density in the bulk crystal, which is 8 for the graphite unit cell, with a unit volume of $a\sqrt{3} \times a\sqrt{3} \times c$. The probability of the first peak in a $g(r)$ analysis is the greatest as it represents the nearest neighbor distance which is quite well-defined across all atoms. Interestingly, RDF can provide a connection to experiment, as it is a physical quantity that can be computed by neutron or x-ray diffraction, however that is not considered as part of this present study. The RDF is useful because it can help distinguish intricacies between crystallographic geometries across multiple systems or in this case, grain boundaries and surfaces. When discussing $g(r)$ and the interatomic potential $U(r)$, connections can be made to total system internal energy.

Figure 4.5 displays the radial distribution analysis of the ten grain boundaries explored during the present study. Here, an analysis region of size $2a \times c/2$ Å, running the length of the boundary in y was chosen to help identify differences in atomic order. This region captured only the GB region adjacent to the free surface, which is the key location for determining GB intercalation rate. Like mentioned above, there is no distinguishable differences among all the boundaries tested for the entire sampling volume. The inset shows a close-up of the first peak of the same boundaries and there are slight differences in the maximum peak values, however their ordering does not correlate with intercalation rates.

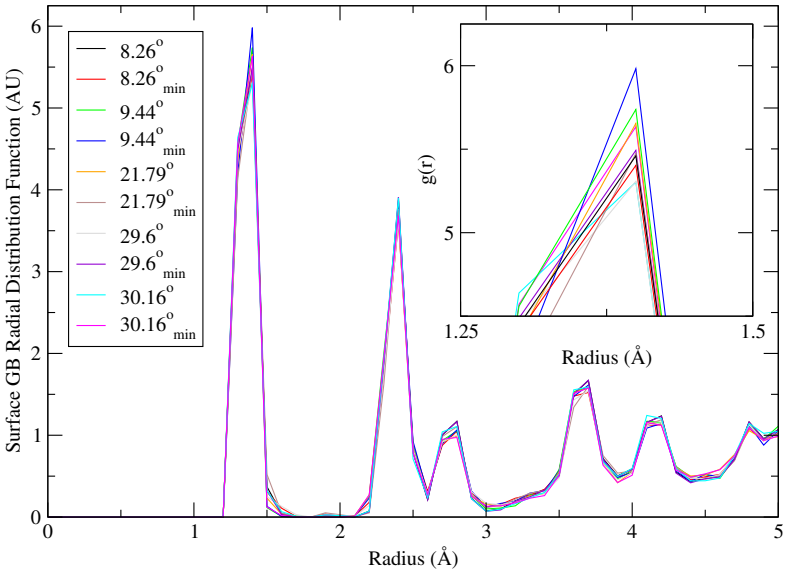

Figure 4.5: Radial distribution analysis for each grain boundary tested during intercalation simulations. An analysis region of $2a \times c/2$ Å running the length of the boundary was chosen for the analysis. The inset is a close-up view of the first peak shown in the main panel.

4.3.2 Resonance Times

As a means to try to expose differences among boundary intercalation rates, an analysis of atomic resonance times was performed. Resonance refers to the amount of time an atom spends in a defined region or structure. A program was created to track Li motion in a region adjacent to the free surface at the GB in the first layer of carbon atoms. The goal was to see how long atoms were remaining in this boundary region and where they were exiting the region after a given amount of time. If one boundary was being sampled much more frequently than the other, *i.e.* atoms were reaching the GB region more often, it would lead to the belief that the intercalation rate would be higher for that system. However, studies revealed that both high and low intercalation rate boundaries exhibited nearly identical attempt frequencies, consistent with the artificially induced flux noted in the deposition procedure. A secondary metric investigated was the actual success rate of intercalation versus deintercalation back to the free surface, and as expected, the success rate was much higher in the rapid intercalation boundaries. This leads to an interesting result; while boundary structure may allow for atoms to site at the GB for an extended period of time, the underlying structure of adjacent graphene planes may hinder intercalation through the

surface plane. Since no distinct conclusions could be drawn from the resonance analysis, a qualitative method was introduced to explain rate differences.

4.3.3 Intercalation Sites

Evidence for a mechanism controlling intercalation rate was found via visual inspection of the free surfaces near GBs, particularly near identified intercalation sites. Because atomic trajectories are known, it was straightforward to identify the position along the GB where any given Li atom entered the graphite crystal. All such sites were found for a high rate and the lowest rate system and data obtained are shown in Fig. 4.6. Three images are shown for each system; all views are along negative z, looking down on the free surface of the graphite bi-crystals and centered on one GB in each system. For each system, one image shows the bare surface plane; the second image shows the surface plane with intercalation sites labeled and the third image is a magnification on an intercalation site. The bare surface images show that structure in-plane was well maintained despite buckling that occurred near GBs. However, rings of size both greater and less than six formed, which were defect sites. For the high rate system, predominantly seven member rings formed; however, larger rings formed in a few regions. For the low rate system, an ordered alternation between five and seven member rings formed along the GB.

Dark spheres in Fig. 4.6 indicate sites where Li entered GBs. It can be seen that intercalation was not uniform along either GB and that there instead exist certain sites where intercalation preferentially occurred. In every case that was identified, Li atoms passed through rings with size seven or greater. As shown in the magnified view for the fast rate system, a significant amount of intercalation occurred where a twelve member ring was in close proximity to an eight member ring. Intercalation occurred through seven member rings but such events were rare relative to intercalation through larger rings. Because the largest rings that form on the lowest rate surface have seven members, intercalation occurs relatively rarely into that GB. Interestingly, not all rings larger than seven were observed to be intercalation sites. For example, near the center of the high rate system in Fig. 4.6, a ten member ring was observed in close proximity to a nine member ring;

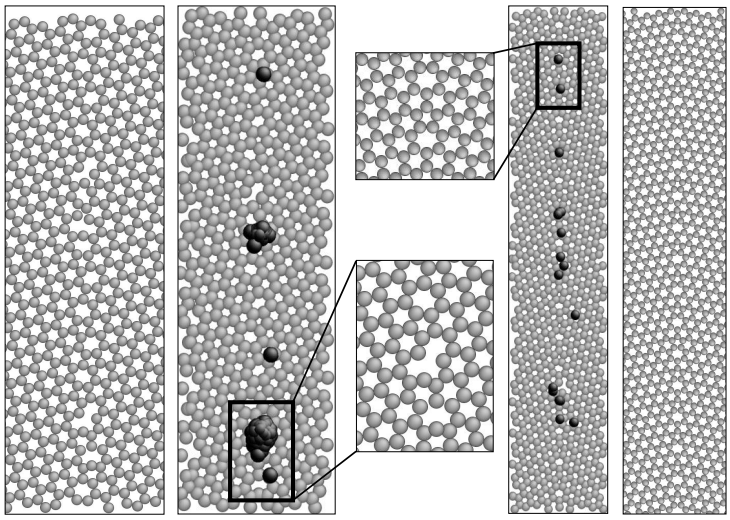

Figure 4.6: Two panels on the left show the bare graphite free surface intersected by a high intercalation rate GB ($\alpha = 30.16°$) as well as the same surface but with Li intercalation sites highlighted by dark spheres. Two panels on the right show the same views but for the lowest rate GB ($\alpha = 21.79°$). The central images show magnifications of Li intercalation sites.

however, intercalation occurred preferentially through the nine member ring. Thus, a more nuanced understanding is required of local atomic structure that abets intercalation from the free surface. However, one further observation was that such structure must be somehow similar to structure inside the GB because preliminary evidence suggests a correlation between the rate of free surface intercalation and GB diffusion rate. More work is necessary to quantitatively clarify this.

4.3.4 Hybridization Analysis

To support findings of the visual inspection of intercalation sites, subsequent analysis has been done on the boundary structure at the free surface. Like discussed previously, the AIREBO interatomic potential is a bond-order potential and thus allows researchers to investigate and locate bonding conditions for given atoms. Carbon atoms in graphite form sp^2 bonds in their equilibrium state, meaning each atom has three neighbors with double bonds. This structure can be disrupted at defects such as grain boundaries and thus may provide supporting evidence to previous claims about intercalation sites. Using the

same investigation region as the $g(r)$ analysis, the bonding conditions of each atom over time were recorded and any atoms in a bond order other than sp^2, such as sp (two NN) or sp^3 (four NN) were highlighted. The image at bottom center of Figure 4.6 contains multiple sp bonded atoms in the 12-member ring that was a high volume intercalation site. Alternatively, the 5-7-5 ring structure in the top center image contains only sp^2, even at the GB.

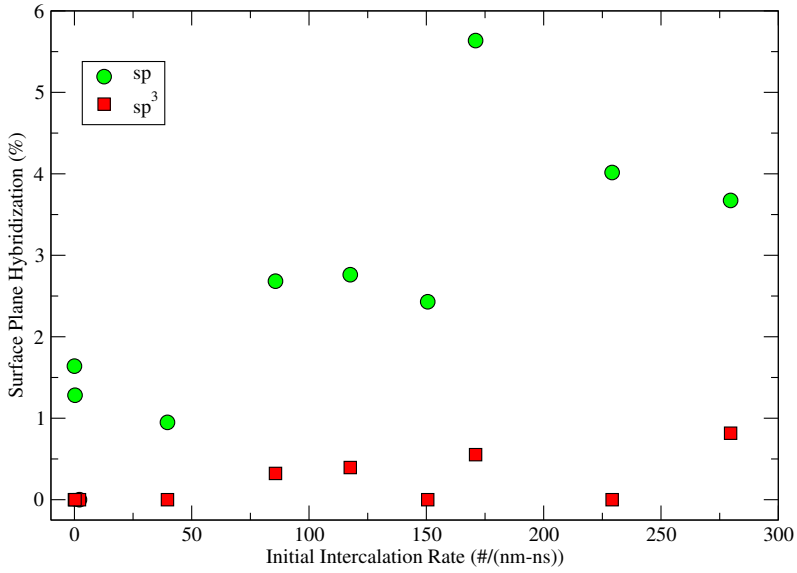

Figure 4.7: Percentage of sp and sp^3 bonding in the graphite plane adjacent to the free surface as a function of initial intercalation rate. Only atoms located where the grain boundary intersects the free surface are considered. Equilibrium bonding configuration in graphite is sp^2.

Figure 4.7 details the percentage of extraordinary bonding scenarios $\left(sp, sp^3\right)$ as a function of initial intercalation rate. The percentages were calculated by the sum of atoms with sp or sp^3 bonds divided by the total number of atoms in the analysis region. It's quite obvious that there is no correlation between intercalation rate and sp^3 bonds, or over-coordinated carbon atoms. Regardless of intercalation rate, all GBs at the surface show low levels of sp^3 bonding. Interestingly though, there is evidence of a trend between sp bonds, or under-coordinated carbon atoms, and initial rate, k_0. Although the trend is not absolute, it could be said that as the percentage of sp bonds increases, the number of larger carbon rings, or possible intercalation sites, at the surface are increasing, thereby growing the probability of a successful intercalation event. It's worth noting that one of

the slowest boundaries has an initial rate of 2.5 $Atoms/\left(nm-ns\right)$ but contains no 'special' bonds. Figure 4.8 shows such a boundary, where only sp^2 bonds are present, albeit some of them distorted in nature. This boundary has a unique 5-7-5 repeated hexagonal ring structure, which plays into earlier discussions regarding GB structural units. Interestingly, this is the simplest of GB structures studied here, where the remainder are much more disordered at the interface thus making identification of repeating structure units more difficult.

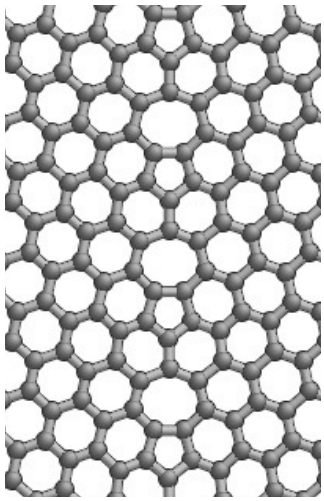

Figure 4.8: Surface geometry of the low intercalation rate boundary, $\alpha = 21.79°$, that contains only sp^2 bonds.

Since bond order can be determined with a potential such as AIREBO, it lends itself to further analysis of NN bonds via bond angle calculations. The covalent bonds in graphite are very well described and thus for bulk graphite remain very close to the equilibrium angle of $\theta = 120°$, as seen in Figure 4.9. For certain cases such as the slow rate boundary which exhibited no sp or sp^3 bonds, a bond angle analysis could reveal highly distorted bonds that abet increased intercalation. However, as Figure 4.9 shows, both the fast and slow boundaries have similar deviations from bulk graphite but there are no distinguishing features between them. In fact, all the boundaries investigated show comparable bond angle distributions with only minor, negligible differences. This analysis may prove more useful for grain boundary diffusion, as there is greater statistical averaging and larger amounts of three dimensional bonding throughout the boundary.

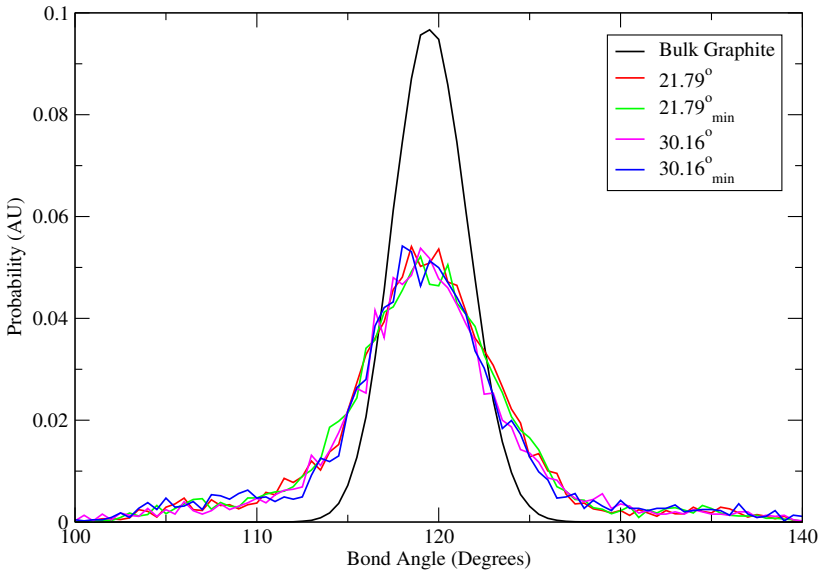

Figure 4.9: Bond angle analysis for fast and slow rate boundaries compared to bulk graphite. The 'min' subscript denotes a minimum energy configuration for a given angle. The standard bond angle in graph is 120°.

4.4 Conclusions

Certain aspects of models used here bear discussion. Systems modeled are chemically pure in Li and C; related to this, the electrolyte and any reaction layer at the electrolyte/anode interface were omitted from the model here. However, it is unknown how the reaction layer would influence ring structures near GBs on the graphite free surface. Regardless, details of the graphite/electrolyte interface do not influence the internal GB structure; thus, more rapid GB diffusion may still cause variation even if surface structure effects are disregarded. Another obvious omission from the current model is dynamic charge transfer between intercalating Li and host C atoms. Perssons,*et al.*, observed no C-C bond reconstruction as a result of Li intercalation and concomitant C charge transfer; thus, we do not expect that charge transfer would change the structure of our GBs and rate differences would thus persist [70]. Additionally, any such model would be equivalently implemented for all GBs studied; therefore, we assert that differences between intercalation rate for different GBs may change but that relatively fast versus slow boundaries would still be observed.

Significant variation in GB self-diffusion has been observed previously for metals [78,

87]. Here, a similar effect was revealed for a covalently bonded material with pronounced structural anisotropy where the diffusing material was another species. The further implication is that grain boundaries present on basal planes of HOPG at anode/electrolyte interfaces may present a source of variation for performance in Li ion batteries due to variations in GB mass transport. Nonetheless, predicting how observed differences in GB intercalation rate will affect performance in Li ion batteries requires additional consideration into GB diffusion mechanisms and energetics. An overarching goal is for understanding gleaned from atomic scale simulations to precipitate a diffusion model capable of more accurate continuum scale predictions of anode charge/discharge behavior.

Chapter 5

Grain Boundary Structure and Dynamics

5.1 Introduction

In Chapter 4, the role of grain boundary surface structure on intercalation rate was investigated for various symmetric-twin tilt GBs in graphite. Intercalation rates varied by over two orders of magnitude across the boundaries tested, providing another explanation for variability of Li diffusion in graphite. As informative as this study was, it focused solely on surface structure, which makes up an extremely small percentage of a grain boundary. Additionally, the solid-electrolyte interface was not modeled, so the mechanisms from the free surface into the GB may not truly reflect atomic motion in an anode. In this chapter, grain boundary diffusion will be investigated for a select number of boundaries from the intercalation studies. This study more closely reflects the work done in metallic systems, where bulk boundary diffusivity is addressed. An important connection to be made is the relative rates of diffusion across different boundaries, but also to the initial intercalation rates of the same boundary. An outstanding question is, if a boundary exhibited high intercalation rates, does that correlate to fast grain boundary diffusion? Do low intercalation rate boundaries exhibit little to no GB diffusion? Again, it is believed that GB structure plays a large role in diffusion through the boundary, but there are other variables

to consider as well.

During intercalation studies, specifically after the first gallery adjacent to the free surface had been sufficiently loaded, diffusion through the GB into subsequently deeper galleries began. This clues into the role of Li concentration on GB diffusion. Persson *et al.* noted a significant dependence on Li gallery diffusion on concentration and it leaves reason to believe that GB diffusion is no different [70, 71]. Therefore, in addition to probing diffusion rates as a function of misorientation angle, concentration effects will be investigated.

Here, Stage II $Li_{0.5}C_6$ and Stage I LiC_6 as seen in Figure 5.1 will be investigated for various grain boundaries. As mentioned previously, staging refers to the geometric configuration of Li-filled layers in graphite. Stage II corresponds to an empty gallery between Li filled galleries, while Stage I has Li in every gallery. The two loadings were chosen because they have identical in-plane Li concentrations but $Li_{0.5}C_6$ obviously contains half as many Li atoms as the fully-lithiated case. Previous work has noted that the $Li_{0.5}C_6$ case is mixed-phase and thus provides evidence that GB diffusion may be present to create such a configuration of both Stage I and Stage II arrangements.

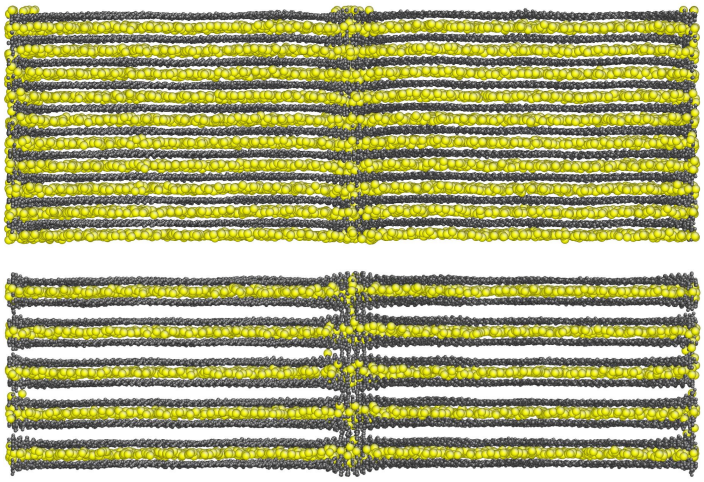

Figure 5.1: Initial Li configurations for GB diffusion studies. Top panel shows Stage I LiC_6 while the bottom represents Stage II $Li_{0.5}C_6$.

Table 5.1 provides details of the boundaries to be tested during these diffusion studies, along with the results from the intercalation studies detailed in Chapter 4. The initial

Table 5.1: Intercalation results for grain boundaries considered in diffusion studies.

α (Deg)	σ (J/m^2)	k_0 $(Atoms/(nm-ns))$
8.26	3.731	117.55
	5.712	229.16
21.79	4.555	0.01
	4.696	2.15

intercalation rate, k_0 was calculated when the diffusive flux for all boundaries was approximately the same, which was between 200 and 300 ps. Since the systems studied had different GB lengths, the units were chosen in an attempt to normalize such differences, and provide a clear picture as to the relative speed at which GBs abet intercalation. Like mentioned previously, intercalation from the free surface slowed greatly once the first gallery in each case had sufficiently filled. The reasoning here is that atoms must diffuse deeper through the GB before gaining access to subsequent galleries where rapid diffusion occurs. This intricacy will be better explored here, since the driving force was one gallery to the next will be uniform throughout since there is not an induced deposition or flux of atoms towards the GB. Finally, take note that for each misorientation angle, α, the higher energy boundary produced a markedly higher intercalation rate.

5.2 Procedure

For this study, symmetric-twin tilt grain boundaries with two different misorientation angles, α will be modeled, consistent with those considered in previous work [81]. Both intermediate and low energy boundaries are investigated, again to probe its effect on diffusion rates. While the intercalation studies were rather transient in that simulations began with an empty graphite bi-crystal, these diffusion studies are initialized and equilibrated with Li atoms present. Since graphite expansion occurs as concentration increases, it is evident that if dynamics were enacted immediately, these systems would become rather unstable as they try to accommodate rapid size changes. To combat this, energy minimizations are performed along with several different equilibration regimes before collecting transport data.

Each grain boundary system was constructed and subsequently minimized according to the previously stated methods with no Li atoms present. Lithium were then inserted, at random, into the bi-crystal, externally from LAMMPS to the appropriate loading of either $x = 0.5$ or $x = 1.0$. It's important to note that atoms were not preferentially deposited into the GB but there were no restrictions, other than overlap criteria, as to where an atom could be placed. Once each GB system was constructed, an energy minimization was performed and the simulation box was allowed to relax such that the system trended towards a zero pressure state. That way, the loaded cells could assume their equilibrium lattice constants, or close to it, before enabling dynamics.

Subsequently, an isobaric-isenthalpic (NPH) ensemble was activated for 50 ps with temperature rescaling to 300 K every timestep, again to minimize the chances for an unstable grain boundary. Such instabilities manifested when this equilibration step wasn't taken, in the form of transient pressure waves causing oscillations of the bi-crystal about the y axis. The final step of equilibration was an isobaric-isothermal ensemble at $p = 0.0$ bars and $T = 300$ K for another 50 ps before moving to diffusion runs. The diffusion simulations themselves use a canonical (NVT) ensemble for the graphite bi-crystal and a microcanical (NVE) ensemble for Li atoms, the same used for bulk diffusion studies in Chapter 3. A $t = 0.0001$ ps timestep was used for all dynamics simulations with Li position data recorded every picosecond.

During equilibration simulations, the Li atoms away from the boundary quickly assumed the expected ordering of $\sqrt{3}\times\sqrt{3}$ as noted by others [70]. Since graphite is so highly ordered, the lattice disturbances remain very tight to the GB such that this ordering is present within one lattice constant of the GB. As observed earlier, diffusion is highly suppressed when a crystal is fully loaded and thus the atoms in planes of the bi-crystal should follow similar dynamics of hopping motion rather than ballistic diffusion. Therefore, atoms near the GB may be exposed to transport pathways not ordinarily present in a single crystal. If an atom was to reach the GB and penetrate an open gallery in the Stage II case, its motion would certainly be ballistic in an empty gallery.

Since both starting configurations ($Li_{0.5}C_6$, LiC_6) for each boundary contain fully-

loaded galleries, a first approach to analyze differences is to see how, if any, atoms reach the grain boundary. While long-range grain boundary diffusion may not be evident at first, comments can be made as to the resonance times and short-range transport mechanisms for each type of boundary.

5.2.1 Free Volume

Grain boundaries are unique structural elements in that they differ greatly from the bulk lattice and from the structure in the middle of grains. This uniqueness manifests in the atomic arrangement at the GB, where the spacing between atoms is greater than elsewhere in a crystal. This difference in volume, noted as free volume (FV), has been shown by many to greatly affect the mechanical behavior of materials, most notably in metals [3]. In addition to mechanical effects, there has been evidence that excess FV at a GB can abet diffusion through the boundary. Not all boundaries have the same amount of FV and thus boundaries can exhibit different properties as the FV changes.

The goal of this work is to draw connections between locations of free volume in graphite grain boundaries and Li diffusion rates. With atomic trajectories known for the duration of simulations, pathways of Li atoms through the GB can be studied and referenced to FV pockets. Further, connections to boundary hybridization and bond angles can strengthen the importance of atomic composition at the boundary on diffusion rates.

Free volume is computed by creating a three-dimensional grid which covers the entirety of the simulation cell and measuring the distance from each grid point to the nearest atom [96]. If the distance to the nearest atom was greater than some distance, here taken as ca_0, where c is a constant and a_0 is the lattice constant, then that grid point was marked as free volume. If the distance was less than the parameter value, the grid point was marked as containing an atom. The maximum size of each grid point is $0.05a_0^3$ and the grid is constructed independently of atomic positions.

In this study, atomic positions every 10 ps for 50 ps were imported into the FV program and analyzed (performed by G.J. Tucker, Drexel University). For a given grid point, the total number of times it was counted as FV were summed and thus reported as a 'Total FV

Table 5.2: Grain boundary structural analysis for diffusion simulations.

α (Deg)	σ (J/m^2)	f ($\text{Å}^3/\text{Å}^3$)	sp (%)
8.26	3.731	0.0018	2.21
	5.712	0.0067	3.49
21.79	4.555	0.0081	3.56
	4.696	0.0070	4.21

Count' for that position in the simulation space. With minute changes in FV locations, the diffusive pathways through a boundary can be slightly altered and thus effect long term transport.

An area of interest here is to compute the volume fraction of free volume at the GB, as a means of comparing available *space* for Li transport [96]. This fraction, f, is be computed by:

$$f = \frac{\nu_b}{V_{GB}} \sum_{ijk} N_{ijk} \tag{5.1}$$

where ν_b is the grid point volume, V_{GB} is the grain boundary volume, defined as $4a \times \Delta y \times \Delta z$, and N_{ijk} is the free volume number (1 for FV, 0 for Atom) of grid point (i, j, k). Table 5.2 details the free volume fraction and sp hybridization percentages for each boundary tested here. At each GB energy, the 21.79° boundary showed a higher FV fraction and a greater amount of sp bonding at the GB, which appears contradictory to the trends observed in Chapter 4. Figure 5.2 shows FV locations for the two intermediate energy boundaries tested here. Each image in the Figure details FV clusters as opposed to atoms. The top panels are locations where FV was counted at least once by the above metric, thus galleries in the system show up as FV. The bottom panels show only those FV cells that were counted repeatedly during time-averaging to show continuity in FV pathways. The free-surface shown in all four panels is a manifestation of the analysis method and does not represent a physical vacuum space. The bottom panel shows that by inspection, both boundaries have what appears to be similar amounts of repeated FV, although the FV fraction is indeed different, as shown in Table 5.2.

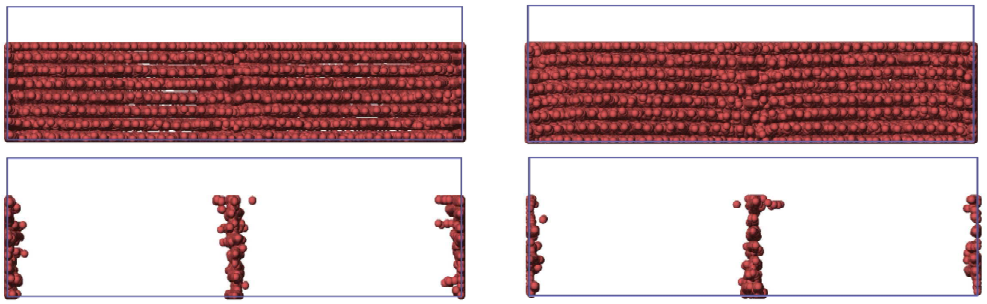

Figure 5.2: Free volume clusters for the 8.26° (left) and 21.79° (right) intermediate energy GBs. The top panels are all instances of FV while the bottom show areas of repeated FV over time.

5.3 Results

Compared to intercalation rate studies, measuring transport in a GB is not as absolute. In graphite especially, atoms constantly transition between the grain boundary and the galleries, making it difficult to track long-term diffusion. However, trends in transport can still be identified. To compare GB transport for high and low intercalation rate boundaries, Li atom positions over 250 ps were tracked, in a method similar to the resonance time mentioned in Chapter 4. An atom's position was logged when it entered the grain boundary, determined here as $\pm 2a$ in x, centered on the GB, running the length of the simulation cell in y and z. The atoms total time in the GB was tracked, along with atomic displacement. Figure 5.3 shows the total displacement over time, for two different misorientation angles and two different GB energies for LiC_6 configurations. Upon initial investigation, there is no obvious differences among the four boundaries after the simulation duration shown here. Over the same time frame in intercalation studies, significant differences had emerged, but there was also no concentration effect like there is here. Interestingly, there are outliers for all GBs, where some atoms exhibited ballistic motion over a short amount of time as well as atoms that showed almost no motion whatsoever. Since graphite grain boundaries are exceedingly narrow, it is not out of the question that atoms hopped from NN sites adjacent to the GB and remained there for an extended period of time. As shown in the Figure, a large number of atoms at least made NN hops, which is equivalent to the $a = 2.4187$Å.

To try to further distinguish between the boundaries, subsequent analysis looked at

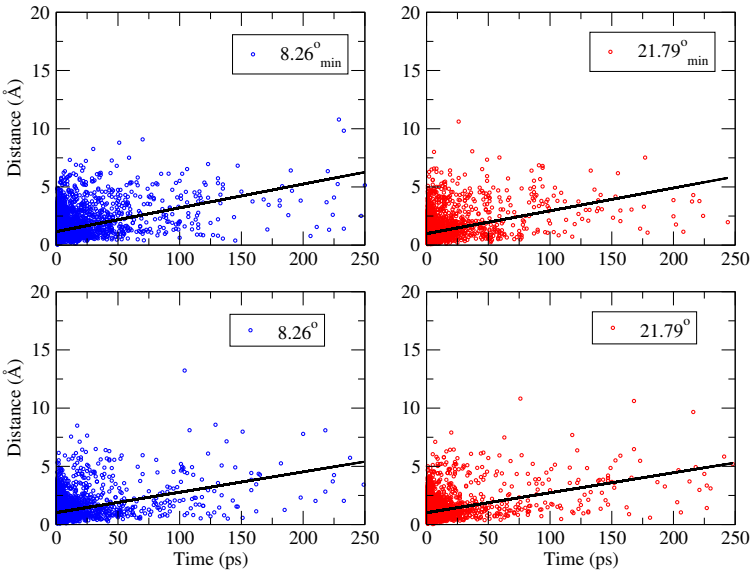

Figure 5.3: Total distance traveled in GB region over time for intermediate and low energy boundaries at LiC_6.

atomic displacements for fixed periods in time. For example, if an atom was in the boundary for at least t ps, its displacement at t was calculated and logged. This was done for 3 separate time windows: $t = 10,\ 25,\ and\ 50\ ps$. This method allows for a two-fold investigation into boundary behavior. First, it provides clear evidence of one boundary abetting longer diffusive pathways, and second, it details the sampling rate of each boundary. The more atoms reach the GB in a given amount of time may be correlated with increased gallery to gallery transport, although this proved not to be true for boundary intercalation. Figure 5.4 shows the number of atoms to travel a given distance over the displayed time for the minimum energy boundaries mentioned above. If at any point during the dynamics analysis, an atom resides in the GB, exits, and then re-enters, those two events will be considered separate, regardless of the amount of time it spends inside or outside of the boundary. Back in Chapter 4, it was discussed that for a given value of α, the lower energy boundary exhibited a lower initial intercalation rate than its higher energy counterpart. Therefore, it's worth noting that the cases in Figure 5.4 should show smaller displacements. As the figure indicates, the 8.26° boundary is sampled more frequently than the 21.79° GB. However, like shown above, there exists no obvious correlation between initial intercalation rate and bulk GB transport properties. Both the high and low k_0 boundaries show a larger

percentage of hops into and out of the boundary over short times, but very little long-range transport over the time durations studied here. One noteworthy difference is that the fast rate boundary shows a greater amount of short range transport in the $1 - 1.5$ Å range, as indicated by the third column from the left in each panel. Aside from that, no differences are evident.

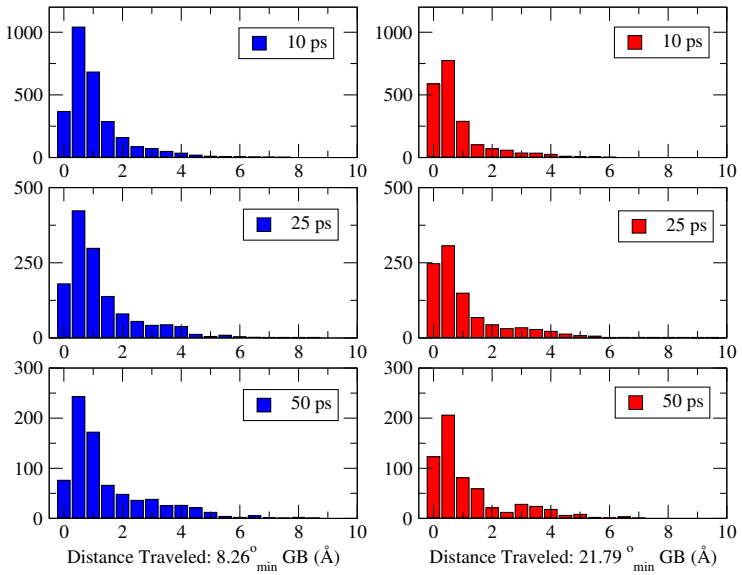

Figure 5.4: Low Energy GBs: Number of atoms versus distance traveled in GB for various amounts of time. The bar graphs on the left are for a boundary that exhibited rapid intercalation, whereas the right boundary showed minimal intercalation. Heights represent the number of atoms which exhibited that amount of transport in the given time window.

In addition to the low energy cases tested, the high energy equivalents for the high and low intercalation rate boundaries were simulated, as shown in Figure 5.5. Like in the previous Figure, the only difference is with the amount of atoms entering the high-rate boundary relative to its low rate counterpart. The length of dynamics simulations for the high energy boundaries are the same (350 ps), as are the low energy boundaries (950 ps). However, since the total amount of time data differs between the two sets, comments relating transport behavior will not be made. Interestingly,there is no long-range diffusion present after the time windows analzyed, but it's worth noting that the diffusive distances shown here, are all greater than those exhibited by bulk LiC_6. Therefore the presence of Li vacancies near the GB as well as disruption of traditional $\sqrt{3} \times \sqrt{3}$ Li order has abetted diffusion in all cases studied.

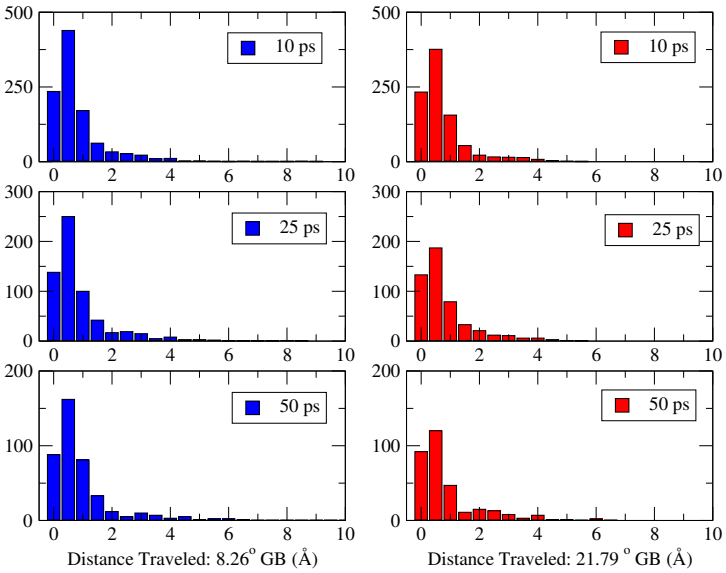

Figure 5.5: Intermediate Energy GBs: Number of atoms versus distance traveled in GB for various amounts of time. The bar graphs on the left are for a boundary that exhibited rapid intercalation, whereas the right boundary showed minimal intercalation. Heights represent the number of atoms which exhibited that amount of transport in the given time window.

As a final attempt to separate high and low rate intercalation behavior in terms of GB diffusion, displacement perpendicular to the graphite planes was investigated individually to directly probe transport between galleries. While the gallery to gallery interlayer spacing in LiC_6 for this model is 3.79 Å, the buckled region at the GB actually blends two adjacent galleries together and thus short vertical diffusion can still correlate with a change in gallery. Again, with the graphite GBs being very narrow, it's plausible that in-plane diffusion near the GB dominated the above analysis and no differences emerged. Figure 5.6 shows z direction displacement as a function of time for atoms traveling in the GB region (same as above). For the 21.79° boundaries, there is little, if any, z displacement greater than one Angstrom. Again, this can still correlate to a gallery transition, but it is not as clear cut as other cases. One could propose that the average distance from an Li atom in a gallery to the mean GB plane is $c/4$, or in this case, 1.895 Å. Therefore, the two low intercalation rate boundaries show no atoms that have traveled greater than this distance, signifying a definite gallery change. The 8.26° minimum energy boundary however shows z direction diffusion distances greater than 2.0 Å, which at the very least exhibit a transition into the

buckled region between two galleries.

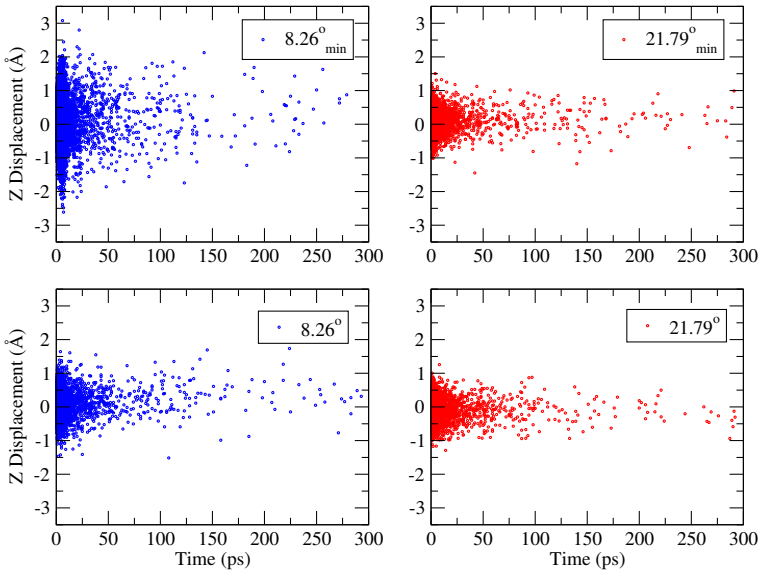

Figure 5.6: Li atom displacement perpendicular to the basal plane as a function of time.

Similar to the 21.79° boundaries, the higher energy 8.26° GB did not exhibit the longer distances like its lower energy counterpart, which is contrary to initial hypotheses that it would have one of the highest diffusion rates among all boundaries tested. Admittedly, more time data is needed before definitively addressing diffusion coefficients and trends. Longer times were investigated for the two minimum energy cases and the observed trends did continue, with the z displacement growing more rapidly in the 8.26° case. Thus, one could say that correlations are possible between initial intercalation rate and GB diffusion rate. For all boundaries tested, the atoms that displaced the greatest in z appeared to spend the shortest amount of time in the boundary. This could be a signal that atoms are reaching the boundary and either making a quick transition to an adjacent gallery or simply traversing the GB in y over greater time durations.

When considering GB structure alongside dynamics, the diffusion data presented thus far appears to contradict initial hypotheses. While the 8.26° GB did exhibit higher levels of diffusivity than the 21.79° boundary, the differences were minimal. In addition, the structural analysis detailed in Table 5.2 shows that the slower intercalation rate boundary actually provides more advantageous structural characteristics for diffusion (greater FV,

higher *sp* percentage). Perhaps the contradiction comes from the distribution of FV and *sp* bonds in the GB, rather than the shear numbers. To further study the structure of the GBs, analysis presented for intercalation simulations is also performed here. A radial distribution analysis focused at the grain boundary (same analysis region for FV) may show disorder at the GB that correlates with diffusion data presented. Additionally, a bond angle analysis of bonds at the GB could present a large variation in structure such that large voids could abet transport.

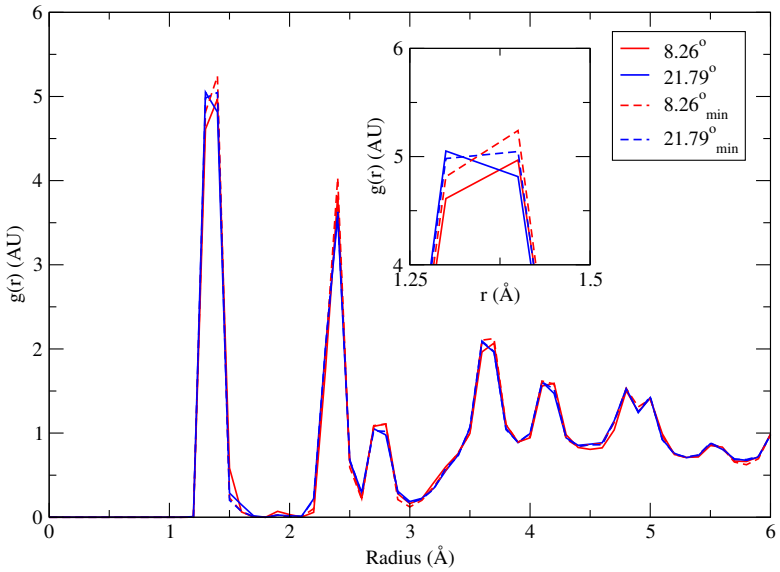

Figure 5.7: Radial distribution analysis of grain boundary atomic structure. (inset) Close-up view of first peak for the main panel. Indices apply to both figures.

As Figure 5.8 shows, there is no discernible differences in the RDF over 6.0 Å worth of neighbor analysis. To clarify further, the inset presents the RDF for the first peak shown in the main panel. Here, there are slight variations in NN probability, but again nothing obvious is shown. One could propose that the 8.26° minimum energy boundary exhibits the highest probability of finding a NN at the first peak, but the disparity is minimal. The bond angle data shown in Figure 5.8 provides some correlation to the diffusion relates in that both 8.26° boundaries exhibit greater bond angle order. This could be seen as advantageous for diffusion, but as shown earlier, diffusion through a perfect graphite lattice is energetically unfavorable. Thus distorted bonds are likely associated with variations in ring structure, which was shown to correlate well with intercalation sites in Chapter 4

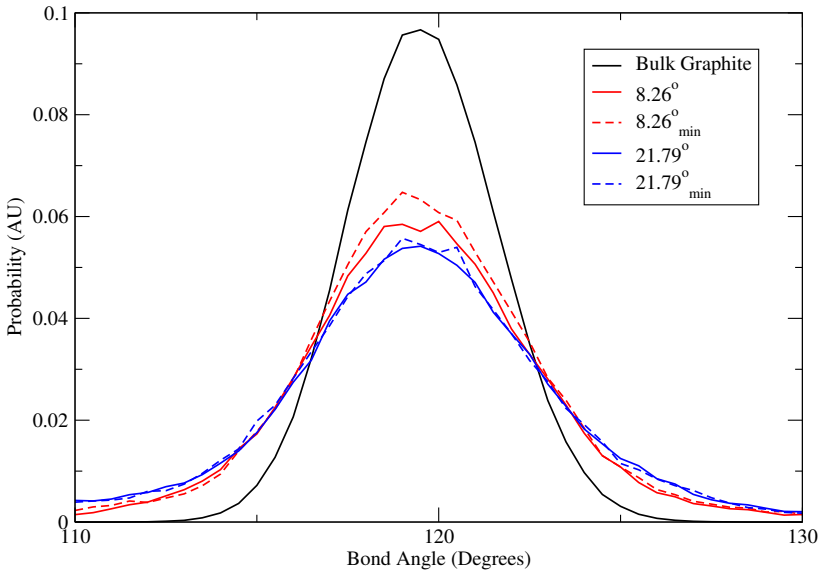

Figure 5.8: Bond angle distribution for atoms at the central GB in a fast and slow intercalation rate GB, compared to bulk graphite. Analysis region is $\pm 2a$ in x, running the length of the boundary in y and z.

and contradicts the diffusion studies presented here. Based on the structural analysis performed, there appears to be little direct correlation between observed structures and diffusion data. However, differences in diffusion rates still appear to be emerging and thus confirms the hypotheses from Chapter 4 and earlier that graphite grain boundaries are a source of variation for Li diffusion.

5.3.1 Concentration Effects

Like mentioned earlier and in detail in Chapter 3, there is a very large concentration effect of Li diffusion in graphite. It became evident in intercalation simulations, when concentration in a gallery would grow great enough such that diffusion would transition to a subsequent empty gallery. Therefore, it's only logical to study concentration effects on GB diffusion. Since the interatomic potentials here deviate from published data in terms of lattice constants at low Li loadings, it was decided that only high Li concentrations would be simulated. Figure 5.9 displays z direction displacements in the 21.79° boundary for $Li_{0.5}C_6$ and LiC_6 loadings as a function of time. The two profiles look quite similar, but there are distinct differences that correlate with staging effects. In the fully lithiated

case, if an atom diffuses from one gallery to the next, it will in theory, reach a gallery with equivalent loading from the one it left. In the $x = 0.5$ case, that same diffusion distance corresponds with reaching an empty or near empty gallery, in which transport is extremely rapid. There are several outliers in the Stage II case, with atoms diffusing 3-4 Å over short times. These distances are consistent with atleast one gallery transition, but may signify the beginning of a second transition.

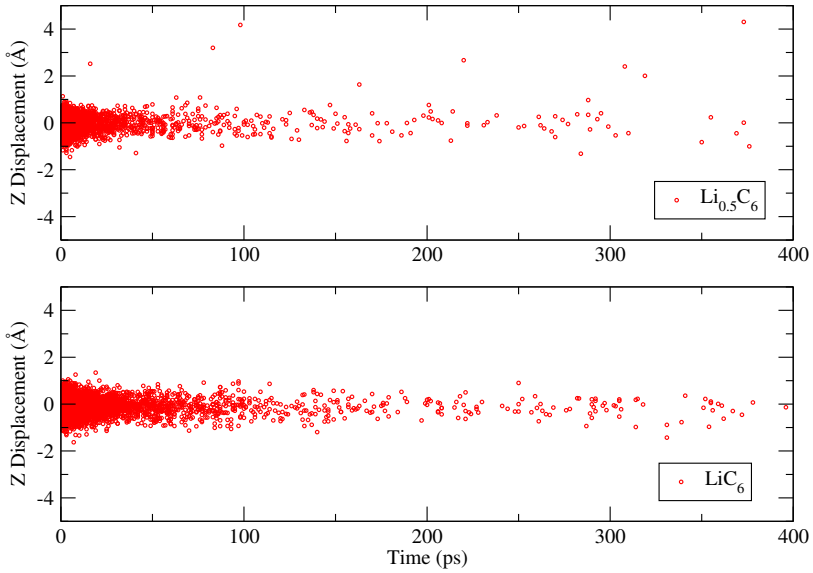

Figure 5.9: GB displacement perpendicular to graphite planes as a function of time for 21.79° $Li_{0.5}C_6$ (left) and LiC_6 (right).

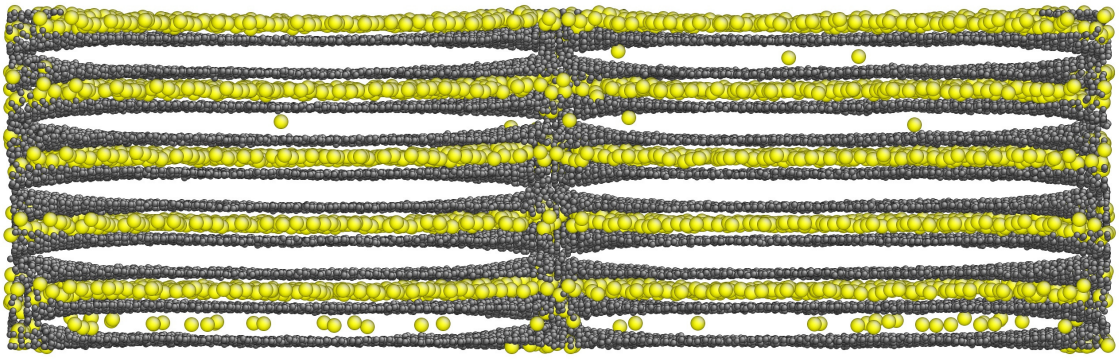

Figure 5.10: Atomic rendering of the 21.79° $Li_{0.5}C_6$ boundary after 850 ps.

Figure 5.10 is a rendering of the $x = 0.5$ loading after 850 ps. While there are some atoms in the originally vacant galleries, the important thing is that atoms do not remain

in the GB once reaching one a vacant gallery. With no atoms in either case diffusing 2+ Å in short times like the 8.26° boundary, it leads to the belief that atoms become trapped in the GB, resonate for an extended period of time, but eventually diffuse through the GB to an open gallery. This theory correlates well with the higher displacements (2+ Å) at longer times in the $x = 0.5$ case. Although hard to tell definitively, there is evidence that a mixed phase is forming in the lower three galleries of Figure 5.10.

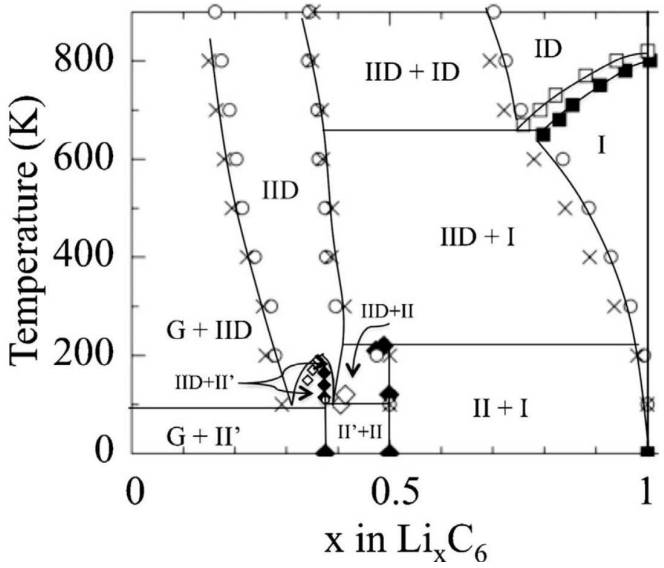

Figure 5.11: Phase diagram of Li-C from first principles [70]. Roman numerals correspond to the stable phases at a given T, G corresponds to graphite, and D represents a disordered phase.

According to first-principles calculations by Persson *et al.*, the stable phase at $T = 300$ K is actually mixed between Stage I and Stage II, as seen in Figure 5.12. Stage II layers are disordered, as the concentrations in that area are not high enough to force Li to assume the $\sqrt{3} \times \sqrt{3}$ loading sequence that is so well-defined at full lithiation. Thus, an interesting effect is at play in the above case as atoms transition to an open gallery. To further provide evidence of a change to a mixed phase, Figure 5.12 shows the gallery concentration versus time for each of the 10 galleries in the simulation. The gallery concentration is computed as:

$$x = \frac{6N_{Li}}{N_C} \tag{5.2}$$

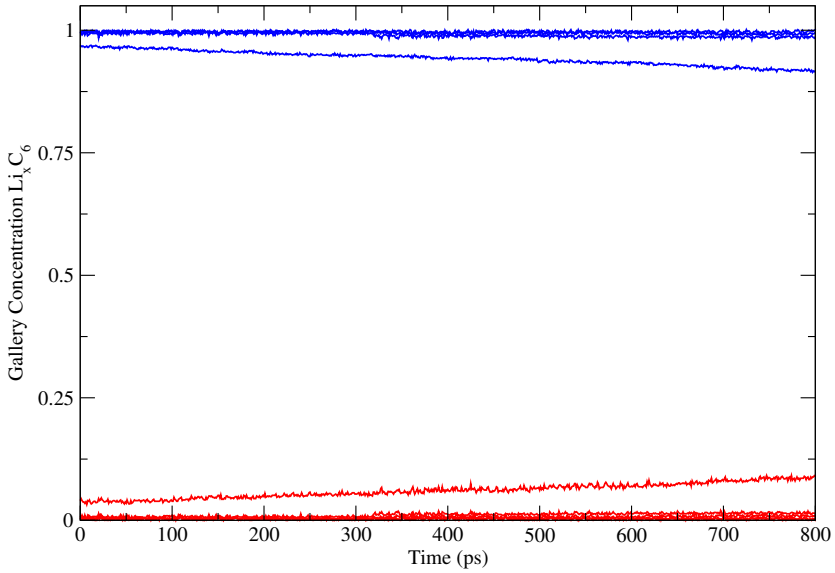

Figure 5.12: Gallery concentration Li_xC_6 as a function of time for a Stage II loading simulation. Galleries that began empty are red, those at started at LiC_6 are blue.

where N_{Li} is the number of Li atoms in the gallery and N_C is the number of carbon atoms per graphene layer. As the figure shows, there is a layer of decreasing concentration, while another layer is growing. The galleries at which the change is occurring are the lowest two rendered in Figure 5.10. This provides compelling evidence that structural elements at each graphene plane promote localized variation in diffusion. Although the driving force is identical for all open galleries in the simulation, only one showed significant changes in concentration. It appears as though the problem of grain boundary diffusion is not simply two-fold (intercalation and bulk diffusion).

5.4 Conclusions

Grain boundary diffusion simulations provide compelling evidence that correlates intercalation rates with bulk diffusion behavior. While there is some truth to the statement that fast intercalation rate boundaries show rapid grain boundary transport, there are many factors to consider and address. The fastest boundary show here was not the fastest from the previous studies. Rather, a lower energy boundary exhibited greater diffusion than its intermediate energy counterpart, which contradicts the results from Chapter 4, where every

low energy boundary has a lower initial intercalation rate. A wider range of boundaries, like those studied earlier, will certainly elucidate broader trends across all GBs.

Another point to consider is that which was uncovered while investigating the effect of staging and concentration as diffusion. With the Stage II simulation slowly beginning a transition to a mixed Stage I and II system, unique aspects of diffusion were uncovered. The fact that only certain galleries were decreasing in concentration to feed open galleries speaks to the overall structure of the GB. It shows that not every layer in the boundary is the same, even though the misorientation angle between crystals is identical. The boundary which exhibited the asymmetric diffusion was the 21.79° GB, which as shown above, is highly ordered. Thus, it is surprising that such diffusion between galleries is occurring. Perhaps the buckling at the GB, as a result of dislocations, is different between layers, thereby affecting transport characteristics separately. Determining the connectivity of free volume may provide further information about this observed phenomena. Two-point correlation functions (TPCF) determine the probability of finding free volume a distance r away from a free volume cluster, while lineal path functions (LPF) determine the probability of finding a free volume pathway all along the vector $\mathbf{r}$ [95]. Each of these methods, combined with trajectory information from MD simulations are important in fully understanding this unique GB behavior.

Finally, regardless of the mechanisms behind different behavior in each gallery, a larger question has been answered about grain boundary diffusion. When considering a grain boundary diffusion model in graphite, it appears that it is not sufficient to only consider intercalation data and bulk transport for a given misorientation angle, α. The simulations performed here show that each graphene layer can affect diffusion differently and thus any model constructed must consider such. If nothing else, this discovery exemplifies the difficult nature of quantifying not only lithium diffusion in grain boundaries, but overall.

Chapter 6

Further Grain Boundary Structural Characterization

6.1 Introduction

Chapter 5 presented first steps towards connecting grain boundary intercalation rates, like those discussed in Chapter 4, with bulk grain boundary diffusion rates. While the connections are certainly meaningful, it's worth expanding the data further to move toward creating a multi-scale model to explain LIB charging behavior. Structural and dynamical diffusion data has been presented for grain boundaries that exhibited fast and slow initial intercalation rates. Differences, although small, did emerge for the boundaries simulated. However, the structural data across the simulations did not exhibit much variation that would lend itself to form a concrete conclusion about causes of diffusional variability. Here, structural analysis has been extended to the remaining GBs investigated during intercalation studies. Dynamics data will be presented in forthcoming work.

Table 6.1 presents results from intercalation studies for the entire range of GBs tested. The previous chapter addressed diffusion for two misorientation angles, namely the 8.26° and 21.79° boundaries for both low and intermediate grain boundary energies. With a larger spectrum of simulations, greater connections can be made between intercalation and diffusion, again with the goal being a GB diffusion model. For clarity purposes, all 10 GBs

Table 6.1: Grain boundary energies and initial intercalation rates explored in this dissertation.

α (Deg)	σ (J/m^2)	k_0 $(Atoms/(nm-ns))$
8.26	3.731	117.55
	5.712	229.16
9.44	3.658	0.25
	3.989	39.65
21.79	4.555	0.01
	4.696	2.15
29.60	3.813	85.70
	5.983	170.97
30.16	3.789	150.58
	4.842	279.65

are investigated here, which includes the four discussed in the proceeding chapter. During intercalation studies, it was shown that grain boundary energy, for a given value of α correlated strongly with initial intercalation rate, k_0. While globally this did not appear true (see Fig. 4.3 inset), there was still a connection to some degree. A stronger connection was formed when investigating the relationship between bond hybridization and intercalation rate. There was no relationship between sp^3 bonding (single bonds) and intercalation rate, however a trend appeared with sp bonding, where the higher percentage of such bonding paralleled increasing rate. Because of this connection, it is worth showcasing the relationship to hybridization for the boundary surface plane, which was crucial in intercalation studies, with hybridization of the entire GB.

6.2 Boundary Hybridization

Figure 6.1 displays the sp hybridization of each boundary tested versus the sp bonding of the surface plane from intercalation studies. The boundary volume is consistent with previous studies, computed as $4a \times \Delta y \times \Delta z$. As expected, there is a positive relationship between the two, reaffirming the hypothesis that bulk diffusion behavior will follow the intercalation results for a given boundary. Another method for observing boundary trends is

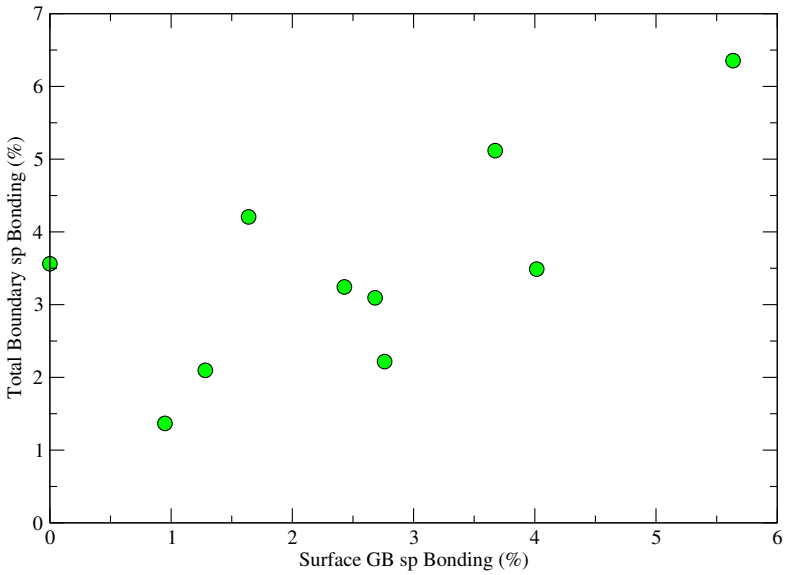

Figure 6.1: Percentage of *sp* bonds in the graphite plane adjacent to the free surface during intercalation studies compared with the percentage of bonds in the entire grain boundary.

comparing hybridization to GB energy, like seen in Figure 6.2. Again, there is little change in sp^3 hybridization as a function of grain boundary energy, signifying graphite's desire to avoid over-coordination. The sp^3 case is present in diamond, with each C having four nearest-neighbors [85]. Perhaps at high enough compressive pressures, some sp^3 would be present at graphite GBs. When looking at *sp* hybridization, there's a positive relationship with GB energy, which at first glance, could clue into the actual disorder at the boundary where larger ring structures are present. Although not every ring structure with greater than 6 C atoms showed *sp* bonding, this configuration was associated with some of the largest carbon rings in the higher intercalation rate simulations.

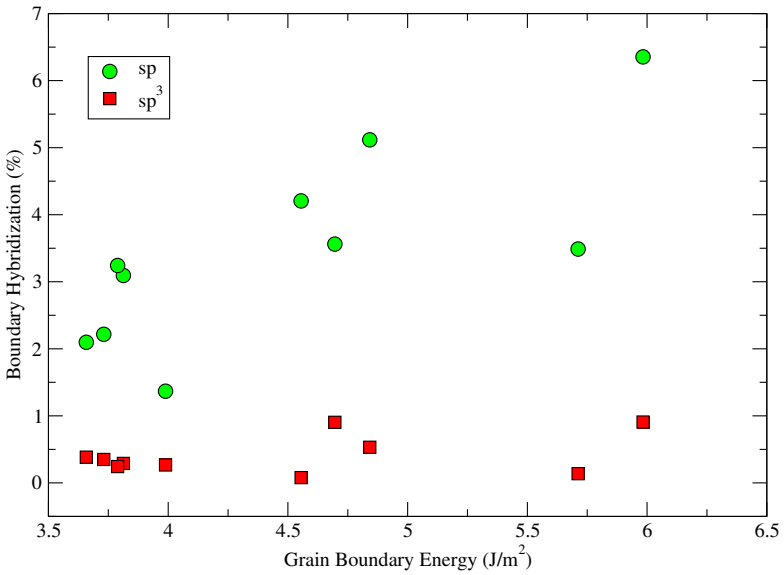

Figure 6.2: Percentage of *sp* and sp^3 bonding in the graphite grain boundary as a function of boundary energy.

6.3 Boundary Atomic Structure

Another set of structural analysis performed was the radial distribution function as well as bond angle distribution for the GB region. As a reminder, neither method exhibited large differences for both intercalation studies nor preliminary GB diffusion studies. Firstly, the g(r) data for all GBs tested is presented in Figure 6.3. Again, there are no distinct patterns visible in the RDF, with the exception of minuscule peak differences at 1.4 Å, the nearest-neighbor distance in graphite. A close-up of this is presented in the inset, with two low-energy, modest intercalation rate boundaries having the greatest peak. Beyond the two highest peaks, it's hard to distinguish between the remaining boundaries, except for the fact that the lowest peak (lowest probability) is for one of the two fastest intercalation rate simulations. Differences are present again the shoulder of the first peak, but ordering does not correlate with any earlier intercalation rate findings. The slight bulge just shy of 2.0 Å was present in the intercalation studies and is not present in bulk graphite. It may be a contribution from an *sp* hybridization, especially those presented in distorted ring structures like the ones seen in the fast boundary of Figure 4.6. Final differences are seen at the third neighbor peak, with two distinct regimes of RDF values. Again, no correlation

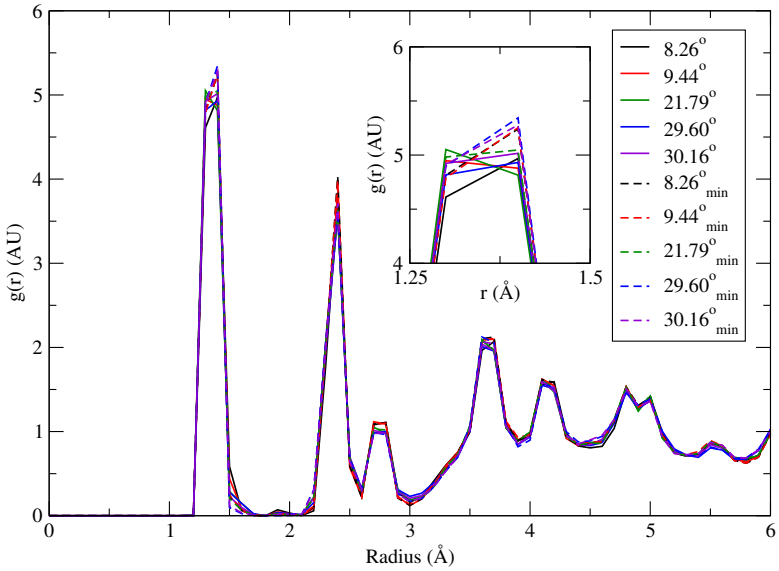

Figure 6.3: Radial distribution analysis of grain boundary atomic structure for five unique misorientation angles (low and intermediate energies). (inset) Close-up view of first peak for the main panel. Indices apply to both figures.

is seen with the intercalation results, but nevertheless the discrepancy is worth noting for diffusion studies.

Bond angle distributions for each GB, centered at 120°, the equilibrium bond angle for graphite (also shown), are presented in Figure 6.4. Like shown in the previous Chapter, the GB with the least amount of deviation from bulk graphite is the 8.26° minimum energy boundary, which showed the most amount of GB transport of the four boundaries originally tested. This idea that less distortion helps diffusion contradicts the RDF results where more distortion from equilibrium bonding was usually associated with larger carbon ring structures in graphene planes.

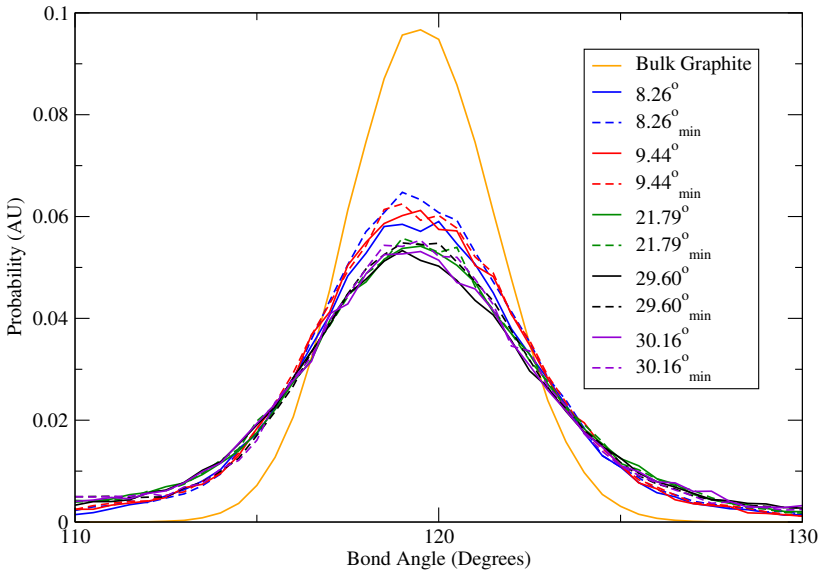

Figure 6.4: Bond angle distribution for atoms at the central GB in each system tested, compared to bulk graphite. Analysis region is $\pm 2a$ in x, running the length of the boundary in y and z.

6.4 Concluding Remarks

Structural analysis for ten, symmetric twin tilt GBs was presented here, consistent with the boundaries simulated during intercalation from a free surface. While there are minute differences with bond angles and radial distribution analysis, there are no definitive trends that allow strong hypotheses to be made about bulk diffusion rates. Rather, connections between hybridization, intercalation results, and grain boundary energy all point towards possible predictable behavior. While the preceding chapter highlighted that the amount of *sp* bonding doesn't necessarily correlate to the greatest diffusion, it can still play a role in defining what boundaries behave certain ways. For example, understanding the distribution of unique hybridizations, bond angles, and nearest neighbor distances could be key to predicting diffusion rates. Another important aspect to consider is the role of free volume connectivity, which will be presented in future work. These connecting networks of FV likely align with *sp* and distorted bonds, such that trajectories could be overlaid and would conceivable follow such paths.

Regardless of the results of future diffusion simulations, it's important note that definitively defining GB intercalation and diffusion in graphite is not intuitive. While certain

trends seem to emerge, they were soon disproved or contradicted by subsequent simulations. To fully quantify diffusion and provide clues to constructing a grain boundary diffusion model, one must fully consider long-term, long-range trajectories and understand that each gallery in a GB could behave entirely differently than the one adjacent to it. Having such an understanding will foster creativity in making connections and forming macroscopic coherence for overall grain boundary transport behavior.

Chapter 7

Future Work and Conclusions

7.1 Future Work

The effect of grain boundaries is rarely considered in covalent systems but as shown here, they serve as integral parts of the mass transport story, similar to transport in metals. While this study was extensive, there are several areas where this work could be extended.

7.1.1 Expanded Grain Boundary Dynamics

Chapter 5 provided evidence that differences exist not only between grain boundaries in terms of their diffusion behavior, but also how within one boundary, there is not an absolute rate as which atoms move into and through a GB. From this, Chapter 6 discussed the structure of several other boundaries and how their structural details may impact associated diffusion rates. Computational time, even in today's world, can be the rate-limiting factor in uncovering research trends. Thus, to further this work, the dynamics of the boundaries presented in the previous chapter need to be completed. Similarities have been exposed for both intercalation and diffusion rates, but increasing the total number of boundaries can only help to solidify any of these trends. Based on the previous studies, several nanoseconds worth of data will be necessary to capture enough motion to make definitive statements about diffusive trends. The intercalation rate cases were significantly faster because differences emerged well before concentration effects became a limiting fac-

tor. As shown in Chapter 3, high concentrations of Li severly inhibit long-range transport, thereby dictating the need for several nanoseconds worth of data. However, the disorder at the GBs here showed promise in abetting diffusion in close proximity to the boundary, and may in fact speed up transport relative to the bulk. Another pathway that could lead to faster results would be the investigation of GB diffusion at lower Li concentrations, but this would need additional consideration as the existing Li-C interatomic potentials fall short in correctly capturing dynamics in this realm. Nevertheless, these loadings may provide clues to the behavior observed in Chapter 4, where gallery diffusion ceased at markedly different Li concentrations.

7.1.2 Graphite GB Diffusion Model

Although the studies presented here looked at a number of different grain boundaries in graphite, each of them was a highly specialized case; the symmetric twin-tilt GB. The computational efficiency that these boundaries provided was the reason for their selection, but this by no means encapsulates the full array of GBs found in reality. To further this study, simulations looking at a general GB, or one at which there is no symmetry would provide insight into a more realistic case of diffusion. The reason these types of boundaries were avoided previously was for the required size of the systems to avoid dimensional mismatch at the interface. Two random grain orientations will form a general GB but there is no guarantee the two grains will have the same periodic repeat length. Systems without periodicity are possible using MD, however care must be taken such that these artificial effects do not interfere with desired properties such as diffusion and intercalation rates.

With a larger variety of grain boundaries quantified both during intercalation and subsequent gallery and boundary diffusion, it will be possible to build a grain boundary diffusion model similar to that developed by Whipple [103]. The goal of creating such a model is to provide connections to simulations beyond the nanoscale, pushing more towards mesoscale and continuum for more practical applications for future anode designs. Although graphite has long been used and studied for its applications to LIBs, there remain

many unanswered questions to which MD can provide insight.

If such a model was to be created with the knowledge gleaned from this study, it should consider the following:

- Intercalation rates from the free surface vary by two orders of magnitude, depending on surface structure.
- Grain boundary energy does not correlate with intercalation rate, but if two boundaries with identical α are present, the higher energy boundary should exhibit more rapid intercalation.
- During intercalation, concentrations in the bi-crystal grow as a function of distance from the free surface, regardless of intercalation rate.
- Rate differences in grain boundary diffusion are less evident than during intercalation.
- The connectivity of free volume likely plays a role in diffusion.
- Concentration near grain boundaries affects overall transport rates.
- Graphene planes in a bi-crystal can behave independently of adjacent planes, thereby dictating the need for multiple diffusive regimes per GB.

While this collection of parameters undoubtedly complicates the Whipple Model, it nevertheless details the important findings of this dissertation and provides guidance for future MD studies that may be used to develop such a model.

7.1.3 Advanced Anode Materials

Recent reviews of Carbon Nanotubes show that in the last decade, their production capacity has increase 10-fold with an increasing number of patents and publications on the topic every year, as noted in Figure 7.1 [26].

Single-walled CNTs (SWCNT), like the ones pictured in Figure 7.2, are a rolled monolayer of carbon atoms (graphene) while multi-walled CNTs (MWCNTs) consist of several concentric layers of graphene with a hollow core. Diameters usually measure around 0.4-2

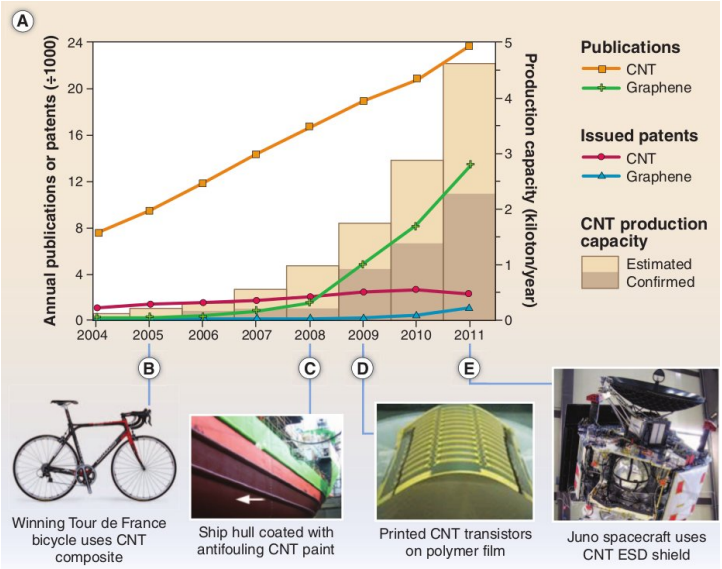

Figure 7.1: Current publishing and patent trends in Carbon Nanotubes and Graphene [26].

nm for SWCNTs, with lengths varying by several orders of magnitude, up to the μm sometimes even centimeter range [41]. Spacing between layers in MWCNTs is equivalent to graphite, or 3.4 Angstroms. MWCNTs were first discussed in the early 1950s by Russian scientists Radushkevich and Lukyanovich whereas SWCNTs weren't realized until the early 1990s by Iijima [60]. CNTs can be synthesized in many different ways however chemical vapor deposition is among the most common.

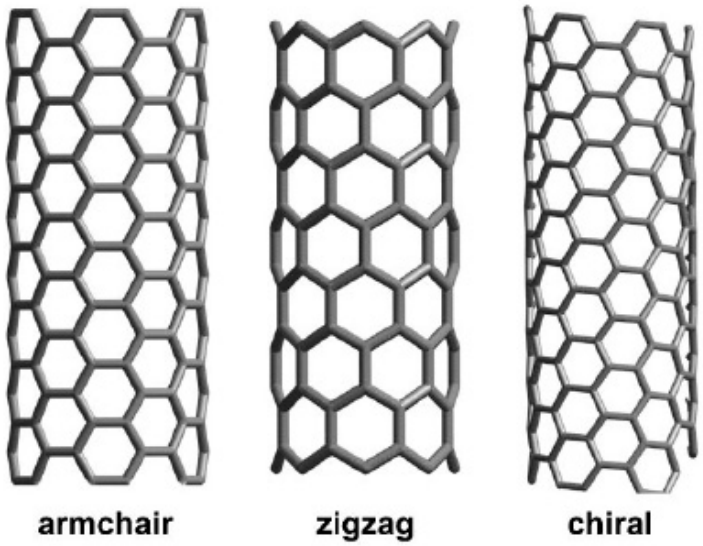

Figure 7.2: Single-walled carbon nanotubes of varying orientations [35].

CNTs are described in similar methods to graphite lattices, where two lattice vectors can be scaled to produce different orientation angles, as seen previously in Figure 2.29. Based on the scaling factors n and m, CNTs can be arm-chair, zig-zag, or chiral in nature. While traditional graphite has high cycle life and relatively low-cost, its low theoretical specific capacity of 372 mAh/g and even lower realized capacity (280-330 mAh/g) limits its use in high-capacity LIBs [107]. The bonding nature of LiC_6 or one lithium per hexagonal carbon ring in graphite is responsible for the low capacity, hence the desire for new materials for LIB anodes.

CNTs are a unique structure relative to graphite and provide increased theoretical storage capacities proposed upwards of 1000 mAh/g because of their high surface area ratio, among other factors [25]. This increased surface area over graphite allows for bonding on both the interior and exterior of CNTs, leading to theoretical phases upwards of LiC_2 [98]. In addition, CNTs have superior mechanical properties compared to other materials, with tensile strengths between 60 and 135 GPa, a Young's modulus approaching 1 TPa, and electrical conductivities of 106 S/m [25]. With these attractive properties, CNTs have also been shown to act as both the anode and current collector in LIB experiments, which removes the dead weight of a metallic current collector [22]. These properties lend CNTs toward being excellent materials for LIB anodes, however certain limitations such as cost effective production capability hinder practicality of their application.

LIBs can charge via two different mechanisms. In both cases, as a current is applied to the battery, lithium ions flow from the cathode, through the electrolyte, to the anode. However, upon reaching the anode, lithium forms two different compounds, depending on the anode material. For carbon-based materials such as graphite and CNTs, lithium forms intercalation compounds, whereas in metals as well as silicon, lithium forms an alloy. This difference relates directly to the theoretical charge capacity of each anode material. Materials than can form alloys with lithium have a much higher storage capacity, but with this comes significant volumetric changes that challenge the mechanical integrity of the material. In addition, alloyed anode materials have very slow diffusion rates $\left(10^{-11} - 10^{-13}\ cm^2/s\right)$ relative to carbon-based materials [63]. With volumetric changes in the hundreds of percent

each cycle, anodes degrade quickly and can separate from the current collector, deeming the battery unusable [25]. While carbon-based anodes are very stable, they have a low theoretical capacity, whereas metals and silicon exhibit the opposite behavior. Researchers are currently trying to uncover ways to capture the benefits of both material types in the development of the newest LIBs.

Recent progress in CNT synthesis has driven production costs down, especially with organized CNT networks such as vertically aligned forests [75]. One advantage of such forests is that each nanotube has robust contact with the metallic current collector, where this isn't always the case in random CNT networks [102]. Previous studies involving MWCNT forests discovered that they have a higher storage capacity than graphite as well as better rate capability, likely because of the uniform geometry. In forest configurations, like seen in Figure 7.3, not only can lithium-ions intercalate along the tube interior, but also in the voids formed between tubes. The problem here is that these triple junctions in CNT bunches form very strong bonds and can trap lithium-ions, leading to a rise in irreversibility, or an anodes failure to release lithium-ions during discharging.

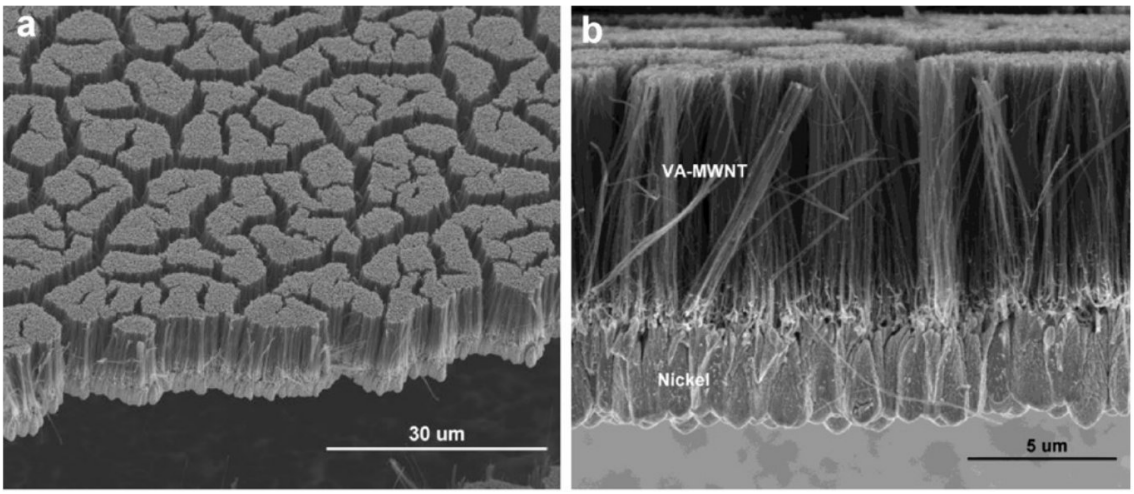

Figure 7.3: SEM image of a MWCNT [102].

One of the latest ideas in LIB anode materials is the advent of composites that consist of a structurally robust carbon support structure and a higher capacity material such as silicon. One idea is the use of CNTs with metallic nanoparticles or bulk silicon matrix. In this configuration, the CNTs prevent large expansions in the alloyed material thereby

preventing pulverization as well as act as a secondary charging method via intercalation and provide a connective diffusion network throughout the anode. Even if there are somewhat large volumetric changes relative to carbon-based anodes, the highly conductive CNTs will remain in contact with the current collector, thereby preserving the battery's integrity.

Both SWCNTs and MWCNTs have been studied for use in battery anodes, however the more interesting case appears to be that of SWCNTs. For larger MWCNTs, intercalation behavior begins to mimic graphite because of the similar interlayer bonding, which has been extensively studied (see Chapter 2). Also, MWCNTs have exhibited problems with exfoliation of graphene layers upon excessive loading and cycling, thereby limiting their use in anodes. This exfoliation leads to repeated solid-electrolyte interface (SEI) development, which first occurs under initial charging of the battery cell [107]. Each time a layer of graphene is exfoliated from a MWCNT, a new layer is exposed to the electrolyte, leading to increased SEI growth. This is similar to the problem with volumetric changes in transition-metal anodes. Repeated volumetric cycling leads to cracking, which exposes more of the anode to the electrolyte, which again fosters SEI growth.

Like graphite, diffusion through the hexagonal rings in a CNT is energetically unfavorable. Therefore, intercalation into the tube center can only occur if the tubes are not capped or there are defects in the sidewalls. Experimental work showed that defective CNTs had better rate capability than pristine CNTs, and ab initio work provided detail into how large defects must be to accommodate lithium diffusion in a given geometry [62, 80]. If defective carbon rings contained at least 9 atoms in the sidewall, a lithium-ion could diffuse through it, gaining access to bonding sites inside the CNT. Once lithium-ions intercalate into the interior of a CNT, they experience random walk diffusion, so if the nanotubes are quite long, there is a high probability that these ions will become trapped, decreasing the charge capacity for future cycles [25]. Defects aiding diffusion is not a new idea, but researchers must be cautious with their application in CNTs. Like any material, the introduction of defects can severely hinder mechanical properties, which is a big advantage of CNTs. In experiments, defects have been shown to reduce the ultimate tensile stress of CNTs to as low as 25 GPa depending on chirality, which could pose a problem in flexible LIBs [100].

Therefore, there must be a middle ground where defects enhance intercalation but do not sacrifice mechanical strength to the point where the anode is unstable.

Similar to defects having an effect on mechanical properties and intercalation, tube chirality and diameter also play a role. The chirality of a tube determines whether a CNT is either metallic or semiconducting by design. Kawasaki stated that metallic SWCNTs have a reversible capacity as much as 5 times greater than semiconducting nanotubes, however this was not a direct measurement because of difficulties in experimentally separating CNTs of different chirality [45]. Jaber-Ansari used ab initio calculations to show that while metallic CNTs do show increased capacity, there are dependencies on CNT spacing as well as diameter [42]. As diameter increases, ions are more likely to intercalate into the tube itself, whereas if the distance between adjacent nanotubes increases, so does the binding energy of lithium-ions. Interestingly, Jaber-Ansari noted that for binding energy versus separation distance in metallic and semiconducting SWCNTs there are points where each type of CNT has a higher binding energy than its counterpart, as shown in Figure 7.4. Also, he showed that binding energy varies versus Li concentration, noted by different bonding characteristics for each type of SWCNT. Again, many variables are at play in each simulation and experiment, so these results are very case-specific.

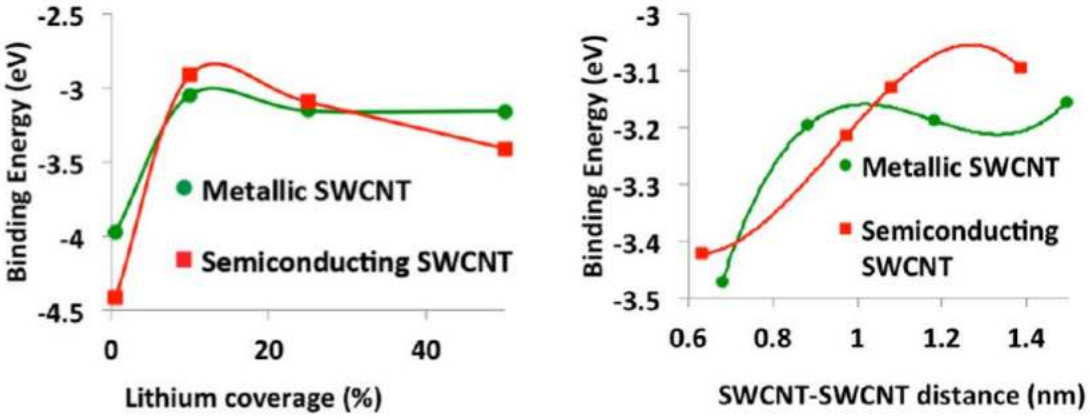

Figure 7.4: Binding energy in metallic and semiconducting CNTs as a function of lithium concentration and SWCNT separation distance [42].

Finally, orientation of CNTs can play a large role in capacity because of varying diffusive pathways throughout the anode. Vertically-aligned forests of CNTs provide a uniform

structure for lithium intercalation, but this can also lead to high irreversibility. On the other hand, random networks of CNTs may provide multiple diffusive pathways throughout the anode but their disordered geometry could lead to widely varied intercalation behavior, similar to the discoveries noted in this dissertation of differences among graphite grain boundaries. Both geometries need to be investigated further because each could have its own niche in anodes, depending on the application.

Current research appears to be moving toward CNTs as support structures in metal/transition-metal anodes, however there remains a large amount of variability in lithium-CNT behavior to the point where a concise composite fabrication decision cannot be made. Some of the latest experimental trials with CNT composites include titanium-oxide, silicon, and graphite/graphene oxide [53, 111, 63]. Although there are numerous experimental results analyzing many different aspects of CNTs, the aforementioned geometric variability among nanotubes limits their application until cost-effective production capabilities become known.

There are many variables at play in the field of SWCNTs and MD can provide new details that experiments cannot attain. Adanced research on these CNTS can be thought of in two stages, both useful towards integrating CNTs into composite battery anodes. The most significant computational challenge facing the advancement is the development and parameterization of interatomic potentials for the transition-metal matrix or nanoparticles with CNTs.

Since experiments have shown that vertically-aligned forests can have higher capacities than random CNT arrangements, they are the intended focus of advanced studies. Varying the diameter in these forests allows researchers to probe the transformation in intercalation mechanisms from exterior to interior diffusion in CNTs which could affect the role of defects. Another variable to address is chirality or graphene orientation relative to the tube axis. Udomvech performed ab-initio studies on chirality's effect on CNT intercalation and structural behavior. Three different chiral configurations were tested and differences emerged in the energetic and structural properties of ultra-small (4 Å diameter) CNTs. While only two lithium-ions were present in the system, very different interaction energy

curves were present. Some configurations exhibiting flat curves, associated with no local well, whereas others had a distinct well. In addition, localized strain was characterized around the lithium atom for each case and again each configuration had different reactions to C-C bond lengths around the intercalation site [98]. This result is important because it is in agreement with graphite's behavior upon lithiation between layers. While Udomvech's work provided key baselines for studying stress evolution, he admitted to shortcomings in understanding the whole picture because of computational constraints. Testing the intercalation differences between metallic and semiconducting CNTs with MD allows advancement from Udomvechs work as it applies to both pristine and defective CNTs.

While there has been extensive work on CNTs role in LIB anodes, very little literature has addressed the stress behavior in CNTs during intercalation events. For each of the above cases, the stress response under intercalation can be traced, in hopes of uncovering potential mechanisms leading to CNT breakdown, especially in the defective cases. With the intent to apply this work to composite or flexible anodes, understanding the intercalation response to stress is just as important as the converse effect. The CNTs will be a support network to prevent extreme volumetric changes under alloying, hence the need for exploring their behavior when exposed to stress and strain. The most interesting case will likely be in stress effects on defective CNTs. Defects are known to aid intercalation, while hindering mechanical response. Seeing how the two properties interact will hopefully provide an intriguing result and provide clues of possible trouble areas.

7.1.4 GB Dopants

The grain boundaries studied here were pure graphite GBs, consisting of carbon atoms either in infinite grains or adjacent to a vacuum. As it's been discussed above, it's rare that GBs are chemically pure. Dopants can be present and thus affect the macroscopic properties of the material. In the construction of a grain boundary diffusion or anode charging model, it's worth considering the effects of dopants. Material from the SEI interface is present, at least to a degree, which affects transport rates into the anode. It is therefore worth asking, could dopants be inserted to abet diffusion? There have been numerous studies showcasing

the effect of dopants on grain boundary diffusion in alumina (Al_2O_3) [59, 61].

7.1.5 Multi-valent Systems

The principles of transport presented here address lithium diffusion in graphite. There are certain characteristics unique to this system both physically and the models presented. Lithium, like that used in LIBs, gives up an electron to form Li^{1+} ions. However, there have been recent studies addressing the use of multi-valent elements, such as magnesium for new batteries. Here, Mg gives up two electrons and thus carries a plus two formal charge, forming Mg^{2+}. The thought as to why Mg may provide better batteries is that now each atom moving through the system can carry twice as much charge as with LIBs. While this is an exciting concept, the actual structure of the charge carrier has changed, bringing about new challenges [55]. It has been shown the the ionic radius of Mg^{2+} is too large to intercalate and diffuse through graphite like Li does so well. Nevertheless, there is a benefit to studying such a system, especially when it comes to GB transport. The thought that GBs are a source of variability in covalent materials can be widely applied and should contribute to advancing studies of Mg batteries. The role of defects (point or GBs) may lend itself to abetting intercalation or diffusion within graphite for Mg, thus making it a viable option for an anode in these batteries.

7.2 Conclusion

The research presented in this thesis exposed differences among intercalation and diffusion rates of a low-mass intercalant, in this case, lithium, in covalently bonded grain boundaries. Significant work was performed on enhancing previous interatomic potentials, which will be shared with the MD community for further refinement and enhancement. Although diffusional anisotropy has long been known in regards to graphitic anodes, no work to date has addressed the role of such grain boundaries. While the breadth of this study was rather focused, it nevertheless connected trends observed in metallic systems with the realm of energy storage materials. Connections between intercalation rate and subsequent GB diffusion were noted, thereby elucidating transport pathways for Li atoms during

charging. Structural characteristics were defined for each boundary as well as their role on ion transport. While there were trends between intercalation, diffusion, and a GB's structure, there was not one common factor that significantly promoted diffusion. While edge-plane intercalation and subsequent diffusion will always remain most rapid in regards to cell charging, these grain boundaries provide a secondary network for Li diffusion and may hold clues as to anomalous battery behavior like that seen on the Boeing 787. The models and techniques created herein can be applied to other systems of interest to battery researchers and thus help advance the every changing energy realm.

Bibliography

[1] Experts: Fire may burn dreamliners' rep, January 2013. URL: `http://www.bostonherald.com/news_opinion/local_coverage/2013/01/experts_fire_may_burn_dreamliners_rep`.

[2] Tesla ventures into solar power storage for home and business, May 2015.

[3] H B Aaron and G F Bolling. Free volume as a guide to grain boundary phenomena. *Scripta Metallurgica*, 6:553–562, 1972.

[4] J. Abrahamson. The surface energies of graphite. *Carbon*, 11:337–362, 1979.

[5] M P Allen and D J Tildesley. *Computer Simulation of Liquids*. Oxford University Press, 1st edition, 1987.

[6] K Ariyoshi, R Baddour-Hadjean, N Dimov, H Horie, Y Kato, J-M K, S Komaba, N Kumagai, Y Makimura, K Matsuki, H Nakamura, M Nakayama, T Ohzuku, S Okada, K Ozawa, J-P Pereira-Ramos, M Wakihara, J-i Yamaki, R Yazami, and M Yoshio. *Lithium Ion Rechargeable Batteries: Materials, Technology and New Applications*. WIley-VCH, 2009.

[7] M Armand and J-M Tarascon. Building better batteries. *Nature*, 451:652–657, 2008.

[8] H Awano, R J Brodd, J Cho, N Dimov, K Gotoh, T Horiba, K Kikuya, M Kono, A Kozawa, M Maeda, H Mori, A Nagai, Y Nishi, T Nishida, H Noguchi, K Numata, T Ogino, Z Ogumi, M Okada, T Okada, S, M Otsuki, B Park, P Ramadass, K Shimizu, M Spahr, Y-K Sun, K Tagawa, M Ue, M Ueda, H Wang, J-I Yamaki,

H Yamamoto, M Yoshio, H Yoshitake, and Z Zhang. *Lithium-Ion Batteries*. Springer, 2009.

[9] P G Balakrishnan, R Ramesh, and T P Kumar. Safety mechanisms in lithium-ion batteries. *Journal of Power Sources*, 155:401–414, 2006.

[10] M Barak, T Dickinson, U Falk, J L Sudworth, H R Thirsk, and F L Tye. *Electrochemical Power Sources: Primary and Secondary Batteries*. The Institution of Electrical Engineers, 1980.

[11] F Beguin, R J Brodd, D Cazorla-Amoros, J Chmiola, M Endo, T Enoki, J-F Fauvarque, E Frackowiak, R Gallay, D Goers, Gogotsi, H Gualous, M Inagaki, Y J Kim, T Kyotani, C Lamy, A Linares-Solano, D Lozano-Castello, P Novak, K C Park, L Radovic, E Raymundo-Pinero, P Simon, M Spahr, and F Suarez-Garcia. *Carbon for Electrochemical Energy Storage and Conversion Systems*. CRC Press, 2010.

[12] D Berndt, C-H Dustmann, H Franke, J L Fricke, W Jacobi, H A Kiehne, N Knudsen, W Konig, H K Kothe, E Nann, P Preuss, W Raudzsus, G Sassmannhausen, D Spahrbier, D Sprengel, U-C Stahl, H Tuphorn, E Wehrle, G Will, and H Willmes. *Battery Technology Handbook*. Marcel Dekker Inc, 2003.

[13] L P Biro and P Lambin. Grain boundaries in graphene grown by chemical vapor deposition. *New Journal of Physics*, 15, 2013.

[14] W J Boettinger, Johnson C E, Bendersky L A, K-W Moon, M-E Williams, and G R Stafford. Whisker and hillock formation on sn, sn-cu, and sn-pb electrodeposits. *Acta Materialia*, 2005.

[15] E Buchovecky, N Jadhav, A F Bower, and E Chason. Finite element modeling of stress evolution in sn films due to growth of the cu6sn5 intermetallic compound. *Journal of Electronic Materials*, 2009.

[16] John W. Cahn, Yuri Mishin, and Akira Suzuki. Coupling grain boundary motion to shear deformation. *Acta Materiala*, 54:4953–4975, 2006.

[17] P R Cantwell, M Tang, S J Dillon, J Luo, G S Rohrer, and M P Harmer. Grain boundary complexions. *Acta Materialia*, 2014.

[18] M Carbajales-Dale, C J Barnhart, and S M Benson. Can we afford storage? a dynamic net energy analysis of renewable electricity generation supported by energy storage. *The Royal Society of Chemistry*, 7:1538–1544, 2014.

[19] Asbury Carbons. Introduction to graphite. Website, 2013. URL: `http://asbury.com/technical-presentations-papers/introduction-to-graphite/`.

[20] N Chakraborti, S Das, R Jayakanth, R Pekoz, and S Erkoc. Genetic Algorithms Applied to Li+ Ions Contained in Carbon Nanotubes: An Investigation Using Particle Swarm Optimization and Differential Evolution Along with Molecular Dynamics. *Mater. Manuf. Processes*, 22:562–569, 2007.

[21] N Chakraborti, R Jayakanth, S Das, E D Calisir, and S Erkoc. Evolutionary and Genetic Algorithms Applied to a Li-C System: Calculations Using Differential Evolution and Particle Swarm Algorithm. *J. Phase Equilib. Diffus.*, 28(2):140–149, 2007.

[22] S. Y. Chew, S-H Ng, J. Wang, P. Novak, F. Krumeich, S-L Chou, J. Chen, and H-K Liu. Flexible free-standing carbon nanotube films for model lithium-ion batteries. *Carbon*, 47:2976–2983, 2009.

[23] Wikipedia Commons. "carbon nanotubes", August 2014. URL: `http://en.wikipedia.org/wiki/Carbon_nanotube`.

[24] J. R. Dahn. Suppression of staging in lithium-intercalated carbon by disorder in the host. *Physical Review B*, 42(10):6424–6432, 1990.

[25] C. de las Casas and W. Li. Ar review of application of carbon nanotubes for lithium ion battery anode material. *Journal of Power Sources*, 208:74–85, 2012.

[26] M. F. L. De Volder, S. H. Tawfick, R. H. Baughman, and A. J. Hart. Carbon nanotubes: Present and future commercial applications. *Science*, 339:535–539, 2013.

[27] M Devanathan and Z Stachurski. The adsorption and diffusion of electrolytic hydrogen in palladium. *Proceedings of the Royal Society of London. Series A, Mathematical and Physical Sciences*, 270(1340):90–102, 1962.

[28] S J Dillon, M Tang, W C Carter, and M P Harmer. Complexions: A new concept for kinetic engineering in materials science. *Acta Materialia*, 2007.

[29] Cadex Electronics. Bu 103: Global battery markets, 2015. URL: `http://batteryuniversity.com/learn/article/global_battery_markets`.

[30] Xiaofeng Fan, W T Zheng, and Jer-Lai Kuo. Adsorption and Diffusion of Li on Pristine and Defective Graphene. *ACS Applied Materials & Interfaces*, 4:2432–2438, 2012.

[31] P E J Flewitt and R K Wild. *Grain Boundaries: Their Microstructure and Chemistry*. John Wiley & Sons, 2001.

[32] Daan Frenkel and Berend Smit. *Understanding Molecular Simulation: From Algorithms to Applications*. Computational Sciences. Academic Press, 2nd edition, 2002.

[33] T Frolov and Y Mishin. Molecular dynamics modeling of self-diffusion along a triple-junction. *Physical Review B*, 79(174110), 2009.

[34] P. Ganesh, J. Kim, C. Park, M. Yoon, F. A. Reboredo, and Paul R. C. Kent. Binding and diffusion of lithium in graphite: Quantum monte carlo benchmarks and validation of van der waals density functional methods. *Journal of Chemical Theory and Computation*, 10:5318–5323, 2014.

[35] B Grady. Carbon nanotube composites, August 2014. URL: `http://coecs.ou.edu/Brian.P.Grady/nanotube.html`.

[36] S. S. Han, Adri C. T. van Duin, William A. Goddard III, and Hyuck M. Lee. Optimization and application of lithium parameters for the reactive force field, reaxff. *J. Phys. Chem. A*, 109:4575–4582, 2005.

[37] Stephen J Harris, Adam Timmons, Daniel R Baker, and Charles Monroe. Direct in situ measurements of Li transport in Li-ion battery negative electrodes. *Chem. Phys. Lett.*, 485:265–274, December 2010.

[38] E. Hazarati, G. A. de Wijs, and G. Brocks. Li intercalation in graphite: A van der waals density-functional study. *Physical Review B*, 90, 2014.

[39] B Hehr, A Hawari, and V Gillette. Molecular dynamics ssimulation of graphite at high temperatures. *Nuclear Technology*, 160:251–256, 2007.

[40] E A Holm, D L Olmsted, and S M Foiles. Comparing grain boundary energies in face-centered cubic metals: Al, au, cu and ni. *Scripta Materialia*, 63:905–908, 2010.

[41] S. Huang, M. Woodson, R. Smalley, and J. Liu. Growth mechanism of oriented long single walled carbon nanotubes using "fast-heating" chemical vapor deposition process. *Nano Letters*, 4:1025–1028, 2004.

[42] L. Jaber-Ansari, H. Iddir, L. A. Curtiss, and M. C. Hersam. Influence of eletronic type purity on the lithiation of single-walled carbon nanotubes. *ACS Nano*, 8(3):2399–2409, 2014.

[43] K Jackson. *Kinetic Processes: Crystal Growth, Diffusion, and Phase Transitions in Materials*. Wiley-VCH, 2010.

[44] J E Jones. On the determination of molecular fields. *Royal Society of London*, 106(738), 1924.

[45] S. Kawasaki, T. Hara, Y. Iwai, and Y. Suzuki. Metallic and semiconducting single-walled carbon nanotubes as the anode material of li ion secondary battery. *Materials Letters*, 62:2917–2920, 2008.

[46] P T Keyser. The purpose of the parthian galvanic cells: A first-century a. d. electric battery used for analgesia. *Journal of Near Eastern Studies*, 52(2):81–98, 1993.

[47] K R Kganyago and P E Ngoepe. Structural and electronic properties of lithium intercalated graphite LiC6. *Phys. Rev. B*, 68(205111):1–16, 2003.

[48] J. Klimes, D. R. Bowler, and A. Michaelides. Van der waals density ffunctional applied to solids. *Physical Review B*, 83, 2011.

[49] R Kobayashi, N. Ohba, T. Tamura, and S. Ogata. A monte carlo study of host-material deformation effect on li migration in graphite. *Journal of the Physical Society of Japan*, 82(094603), 2013.

[50] Eunseok Lee and Kristin Persson. Li Absorption and Intercalation in Single Layer Graphene and Few Layer Graphene by First Principles. *Nano Lett.*, 12:4624–4628, 2012.

[51] P Lejcek. *Grain Boundary Segregation in Metals*. Springer, 2010.

[52] H Lipson and A R Stokes. The structure of graphite. *The Royal Society Proceedings A*, 181, 1942.

[53] J. Liu, H. Feng, J. Jiang, D. Qian, J. Li, S. Peng, and Y. Liu. Anatase-tio2/cnts nanocomposite as a super high-rate material for lihtium-ion batteries. *Journal of Alloys and Compounds*, 603:144–148, 2014.

[54] Te-Huan Liu, Grzegorz Gajewski, Chun-Wei Pao, and Chien-Cheng Chang. Structure, energy, and structural transformations of graphene grain boundaries from atomistic simulations. *Carbon*, 49:2306–2317, 2011.

[55] A. Luntz. Beyond lithium ion batteries. *The Journal of Physical Chemistry Letters*, 6:300–301, 2015.

[56] A Magerl, H Zabel, and I S Anderson. In-Plane Jump Diffusion of Li in LiC6. *Phys. Rev. Lett.*, 55(2):222–225, July 1985.

[57] Lynn Mandeltort and Yates Jr John T. Rapid Atomic Li Surface Diffusion and Intercalation on Graphite: A Surface Science Study. *J. Phys. Chem. C*, 116:24962–24967, October 2012.

[58] A Manthiram. Materials challeneges and oppurtunities of lithium ion batteries. *The Journal of Physical Chemistry Letters*, 2:176–184, 2011.

[59] M M Moghadam, J M Rickman, M P Harmer, and H M Chan. The role of boundary variability in polycrystalline grain-boundary diffusion. *Journal of Applied Physics*, 117, 2015.

[60] M. Montioux and V. L. Kuznetsov. Who should be the credit for discovery of carbon nanotubes. *Carbon*, 44(9):1621–1623, 2006.

[61] T Nakagawa, I Sakaguchi, N Shibata, K Matsunaga, T Mizoguchi, T Yamamoto, H Haneda, and Y Ikuhara. Yttrium doping effect on oxygen grain boundary diffusion in alpha-al2o3. *Acta Materialia*, 55:6627–6633, 2007.

[62] K. Nishidate and M. Hasegawa. Energetics of lithium ion adsorption on defective carbon nanotubes. *Physical Review B*, 71:1–6, 2005.

[63] N. Nitta and G. Yushin. High-capacity anode materials for lithium-ion batteries: Choice of elements and structures for active particles. *Particle and Particle Systems Characterization*, 31:317–336, 2014.

[64] A Oaks. Development of generalized kmc code to study defect mobility in ceramic materials towards nuclear fuel applications, 2010. URL: `https://courses.physics.illinois.edu/phys466/sp2013/projects/2010/Oaks/html/final.html`.

[65] T C O'Connor, J Andzelm, and M O Robbins. Airebo-m: A reactive model for hydrocarbons at extreme pressures. *The Journal of Chemical Physics*, 142, 2015.

[66] Nobuko Ohba, Shuji Ogata, T Tamura, R Kobayashi, S Yamakawa, and R Ashai. Enhanced Thermal Diffusion of Li in Graphite by Alternating Vertical Electric Field: A Hybrid Quantum-Classical Simulation Study. *J. Phys. Soc. Jpn.*, 81(023601), 1-4 2012.

[67] Nobuko Ohba, Shuji Ogata, T Tamura, S Yamakawa, and R Ashai. A Hybrid Quantum-Classical Simulation Study on Stress-Dependence of Li Diffusivity in Graphite. *Computer Modeling in Engineering & Sciences*, 75(4):247–264, 2011.

[68] David L Olmsted, Stephen M Foiles, and Elizabeth A Holm. Survey of computed grain boundary properties in face-centered cubic metals: I. Grain boundary energy. *Acta Mater.*, 57:3694–3703, 2009.

[69] M C Payne, M P Teter, D C Allan, T A Arias, and J D Joannopoulus. Iterative minimization techniques for ab initio total energy calculations: Molecular dynamics and conjugate gradients. *Reviews of Modern Physics*, 64(4):1045–1097, 1992.

[70] Kristin Persson, Yoyo Hinuma, Ying Shirley Meng, Gerbrand Ceder, and Anton van der Ven. Thermodynamic and kinetic properties of the Li-graphite system from first-principle calculations. *Phys. Rev. B*, 82(125416), 2010.

[71] Kristin Persson, Vijay A. Sethuraman, Laurence J. Hardwick, Yoyo Hinuma, Ying Shirley Meng, Anton van der Ven, Venkat Srinivasan, Robert Kostecki, and Gerbrand Ceder. Lithium Diffusion in Graphitic Carbon. *J. Phys. Chem. Lett.*, 2010.

[72] G Pistoia. *Batteries for Portable Devices*. Elsevier, 2005.

[73] Steve Plimpton. Fast Parallel Algorithms for Short-Range Molecular Dynamics. *J. Comput. Phys.*, 117:1–19, 1995.

[74] Y Qi, H Guo, L G Hector Jr, and A Timmons. Threefold increase in the young's modulus of graphite negative electrode during lithium intercalation. *Journal of the Electrochemical Society*, 157(5):A558–A566, 2010.

[75] Z. F. Ren, Z. P. Huang, J. W. Xu, J. H. Huang, H. P. Bush, M. P. Siegal, and P. N. Provencio. Synthesis of large arracys of well-aligned carbon nanotubes on glass. *Science*, 282:1105–1107, 1998.

[76] G S Rohrer, E A Holm, A D Rollet, S M Foiles, J Li, and D L Olmsted. Comparing calculated and measured grain boundary energies in nickel. *Acta Mater.*, 58:5063–5069, 2010.

[77] T J Rupert, D S Gianola, and K J Hemker. Experimental observations of stress-driven grain boundary migration. *Science*, 236:1686–1690, 2009.

[78] Michael S Sellers, Andrew J Schultz, Cemal Basaran, and David A Kofke. Beta-Sn grain-boundary structure and self-diffusivity via molecular dynamics simulations. *Phys. Rev. B*, 81(134111):1–10, April 2010.

[79] V. A. Sethuraman, L. J. Hardwick, V. Srinivasan, and R. Kostecki. Surface structural disordering in graphite upon lihtium intercalation/deintercalation. *Journal of Power Sources*, 195:3655–3660, 2010.

[80] H. Shimoda, B. Gao, X. P. Tang, A. Kleimhammes, L. Fleming, Y. Wu, and O. Zhou. Lithium intercalation into opened single-wall carbon nanotubes: Storage capacity and eletronic properties. *Physical Review Letters*, 88(1):1–4, 2002.

[81] Christopher Mark Shumeyko and Edmund B. Webb III. A molecular dynamics study of lithium grain boundary intercalation in graphite. *Scr. Mater.*, 102:43–46, 2015.

[82] F J Sonia, B Ananthoju, M Jangid, R Kali, M Aslam, and A Mukhopadhyay. Insight into the mechanical integrity of few-layers graphene upon lithiation/delithiation via in situ monitoring of stress development. *Carbon*, 2015.

[83] D E Spearot and D L McDowell. Atomistic modeling of grain boundaries and dislocation processes in metallic polycrystalline materials. *Journal of Engineering Materials and Technology*, 131, 2009.

[84] N Spinner and M Mustain. Nanostructural effects on the cycle life and Li+ diffusion coefficient of nickel oxide anodes. *J. Electroanal. Chem.*, 711:8–16, 2013.

[85] Steven J Stuart, Alan B Tutein, and Judith A Harrison. A reactive potential for hydrocarbons with intermolecular interactions. *J. Chem. Phys.*, 112(14):6472–6486, April 2000.

[86] H. Sun. Compass: An ab initio force-field optimized for condensed-phase applications- overview with details on alkane and benzene compounds. *Journal of Physical Chemistry B*, 102:7338–7364, 1998.

[87] A. Suzuki and Y. Mishin. Atomistic Modeling of Point Defects and Diffusion in Copper Grain Boundaries. *Interface Sci.*, 11:131–148, 2003.

[88] Norio Takami, Asako Satoh, Michikazu Hara, and Takahisa Ohsaki. Structural and Kinetic Characterization of Lithium Intercalation into Carbon Anodes for Secondary Lithium Batteries. *J. Electrochem. Soc.*, 142(2):371–378, 1995.

[89] J-M Tarascon and M Armand. Issues and challenges facing rechargeable lithium batteries. *Nature*, 414, 2001.

[90] J. Tersoff. Empirical interatomic potential for carbon, with applications to amorphous carbon. *Phys. Rev. Lett.*, 61(25):2879–2882, 1988.

[91] J. Tersoff. New empirical approach for the structure and energy of covalent systems. *Physical Review B*, 37(12):6991–7000, 1988.

[92] J. Tersoff. Modeling solid-state chemistry: Interatomic potential for multicomponent systems. *Physical Review B*, 39(8):5566–5568, 1989.

[93] K Toyoura, Y Koyama, A Kuwabara, F Oba, and I Tanaka. First-principles approach to chemical diffusion of lithium atoms in a graphite intercalation compound. *Physical Review B*, 78(214303), 2008.

[94] M A Tschopp, G J Tucker, and D L McDowell. Atomistic simulations of tension-compression asymmetry in dislocation nucleation for copper grain boundaries. *Computational Materials Science*, 44:351–362, May 2008.

[95] G J Tucker and D L McDowell. Non-equilibrium grain boundary structure and inelastric deformation using atomistic simulations. *Internationl Journal of Plasticity*, 2011.

[96] G J Tucker, M A Tschopp, and D L McDowell. Evolution of structure and free volume in symmetric tilt grain boundaries during dislocation nucleation. *Acta Mater.*, 58:6464–6473, September 2010.

[97] Garritt J Tucker, Zachary H Aitken, Julia R Greer, and Christopher R Weinberger. The mechanical behavior and deformation of bicrystalline nanowires. *Modelling and Simulation in Materials Science and Engineering*, 21:118, December 2012.

[98] A. Udomvech and T. Kerdcharoen. Theoretical investigation of lithium-atom insertion into ultra-small diameter carbon nanotubes. *Journal of the Korean Physical Society*, 52(5):1350–1354, 2008.

[99] M W Verbrugge and B J Koch. Electrochemical analysis of lithiated graphite anodes. *Journal of the Electrochemical Society*, 150(3):A374–A384, 2003.

[100] M-S Wang, D. Golberg, and Y. Bando. Tensile tests of individual single-walled carbon nanotubes: Linking nanotube strength with its defects. *Advanced Materials*, 22:4071–4075, 2010.

[101] X-L Wang, K An, Lu Cai, Z Feng, S E Nagler, C Daniel, K J Rhodes, A D Stoica, H D Skorpenske, C Liang, W Zhang, J Kim, Y Qi, and S. J. Harris. Visualizing the chemistry and structure dynamics in lithium-ion batteries by in-situ neutron diffraction. *Scientific Reports*, 747(2), 2010.

[102] D. T. Welna, L. Qu, B. E. Taylor, L. Dai, and M. F. Durstock. Vevertical aligned carbon nanotube electrodes for lithium-ion batteries. *Journal of Power Sources*, 196:1455–1460, 2011.

[103] R. T. P. Whipple. Concentration contours in grain boundary diffusion. *Philosophical Magazine*, 138:1225–1236, 1954.

[104] Nicholas Williard, Wei He, Christopher Hendricks, and Michael Pecht. Lessons learned from the 787 dreamliner issue on lithium-ion battery reliability. *Energies*, 6:4682–4695, 2013.

[105] D Wolf. A broken-bond model for grain boundaries in face-centered cubic metals. *Journal of Applied Physics*, 68(7):3221–3236, 1990.

[106] D Wolf and S Phillpot. metals the densest lattice planes in the stability of crystalline interfaces: A computer simulation study. *Materials Science and Engineering*, A107:3–14, 1989.

[107] Z. Xiong, Yun Y. S., and H-J Jin. Applications of carbon nanotubes for lithium ion battery anodes. *Materials*, 6:1138–1158, 2013.

[108] Fei Yao, Fethullah Gunes, Huy Q Ta, Seung M Lee, Seung J Chae, Kyeu Y Sheem, Costel S Cojocaru, Si S Xie, and Young H Lee. Diffusion Mechanism of Lithium Ion through Basal Plane of Layered Graphene. *J. Am. Chem. Soc.*, 134:8646–8654, April 2012.

[109] R Younesi. Batteries: an important piece in the puzzle of renewable energies for a better world. *Frontiers in Energy Research*, 2, 2014.

[110] Ping Yu, B N Popov, J A Ritter, and R E White. Determination of the Lithium Ion Diffusion Coefficient in Graphite. *J. Electrochem. Soc.*, 146:8–14, 1999.

[111] J. Zhang, Z. Xie, W. Li, and S. Q. M. Dong. High-capacity graphene oxide/graphite/carbon nanotube composites for use in li-ion battery anodes. *Carbon*, 74:153–162, 2014.

Biography

Christopher Mark Shumeyko was born on July 11th, 1988 to Drs. Mark and Nancy Shumeyko in Johnson City, New York. Chris grew up in Vestal, New York and attended Vestal Senior High School where he graduated with honors in 2006. Upon graduation, Chris enrolled at Lafayette College in Easton, Pennsylvania where he quickly became involved in various activities across campus. Academically, Chris majored in Mechanical Engineering, while also becoming Captain of the Ski Team, President of the Sports Marketing Club, an Admissions Representative, and a Career Services Gateway Career Ambassador. He was elected to Dean's List multiple times, became the first student at Lafayette to earn LEED AP status through the US Green Building Council, and won the Aaron O. Hoff Leadership Award as a senior. Chris graduated *cum laude* in 2010 with a Bachelor of Science in Mechanical Engineering and enrolled in the Mechanical Engineering & Mechanics doctoral program at Lehigh University the following fall.

Throughout his tenure at Lehigh, Chris was a teaching assistant for numerous courses, include ME 121, Mechanical Engineering Lab II, where he found his true passion of engineering education. In 2014, Chris was nominated and inducted into the Rossin Doctoral Fellows program. Upon completion of his Ph.D. from Lehigh, Chris will join the faculty of Lafayette College as a Visiting Assistant Professor in the Mechanical Engineering Department.